Multiphase Modelling of Coffee Bean Roasting

Nabil T. Fadai

Mansfield College

University of Oxford

A thesis submitted for the degree of

Doctor of Philosophy

Trinity 2018

To Mum

Abstract

The coffee industry relies on fundamental research to improve the techniques and processes related to its products. However, the exploitation of mathematical models that provide insight into improving the roasting of coffee beans has been largely unexplored. In this thesis, we develop mathematical models to understand specific processes in a roasting coffee bean that are crucial in flavour development and consistency. We explore these processes using several models in a multiphase framework to highlight how phase changes, gas pressures, and various chemical reactions occur in different parts of the bean. These new models are then compared to new and existing experimental data, where the merits and pitfalls of each model are then discussed.

One main phenomenon that is crucial to the roasting process is the evaporation of water. Various models of evaporation rates are proposed and incorporated into the multiphase models, where the resulting qualitative features of the behaviour are discussed. The behaviour of these multiphase models is studied using asymptotic analysis and the leading-order water and vapour transport predicted from this analysis faithfully reproduce the salient features of the model.

We also examine how deformations and material stresses occur during the roasting process. We model the cellulose structure of a coffee bean as a poroviscoelastic material and couple the resulting constitutive equations with aforementioned multiphase models. The qualitative behaviour of this coupled model is discussed for various parameter regimes and used to explain various physical phenomena observed during the roasting process. A summary of key findings is then presented.

Acknowledgements

First and foremost, my sincerest thanks go to Robert Van Gorder and Colin Please for their supervision of this thesis. Robert, your dedication to your students in unrivalled and I am indebted to you for the counsel and initiatives that you have taken with me in this project. Here's to you. Colin, without your wisdom and direction, as well as endless humour, this project would be nothing more than ideas swirling around in my cup of coffee. Thanks for everything.

In addition to Robert and Colin, I would like to thank Robert Farr and Fabien Guilmineau for the additional supervision both in Oxford and at Jacobs Douwe Egberts, as well for JDE's financial support. Along with supplying generous insight (and coffee) to this project, I have thoroughly enjoyed collaborating with you both.

There are some pretty fantastic people in my life that also deserve a massive thank-you. To Ferran, for somehow enduring my presence these past four years and not getting sick of me as a flatmate, fellow mathematician, travel buddy, or friend. To Doireann and Andrew, for helping me transform my research from scribbles and random thoughts to well-crafted presentations. To my family, who have always supported me in my academic pursuits, even if they weren't quite sure what I was doing. To Mikey, Tom, Michael, Ozzy, Greg, and Jamie, for always being up for a pint or two after work and innumerable coffees during the day. Finally, to Pablo, for dealing with my insanity and never failing to put a smile on my face.

I have had my results for a long time:
but I do not yet know how I am to arrive at them.

\- Carl Friedrich Gauss

Contents

List of Figures

List of Tables

Chapter 1

Introduction and Background

1.1 Introduction

The coffee industry is worth more than $100 billion worldwide per year, making coffee one of the most valuable commodities in the world [54]. One vital step in coffee production is the roasting of coffee beans. Most of the publications concerning the roasting of coffee beans present experimental data (see e.g. [2, 51, 60]), using regression analysis and simple empirical models to interpret the results. In this thesis, we discuss key mechanisms that occur during the roasting process. We derive mathematical models in a multiphase framework, which account for these key mechanisms and allows solutions to be found that give understanding of the overall process. Before developing a mathematical model of a coffee bean during roasting, it is crucial to understand the physical structure of the coffee bean at the microscopic level and the important phenomena observed in the roasting process. This section provides a summary of these key points and gives background on the industrial process of roasting coffee beans, to set the work in context.

1.2 The Industrial Roasting Process

For industrial coffee roasting, two varieties of coffee beans are mainly used: *C. arabica* and *C. robusta* [28]. Due to cost and aroma balance, a combination of these varieties is used for the majority of coffee blends [28]. Prior to roasting, both kinds of beans are cleaned and any residual debris removed. Since *C. robusta* beans present different aromas than the *C. arabica* variety, they are sometimes steamed to bring out favourable aromas similar to the *C. arabica* bean before they are roasted [28].

After any pre-treatment, the beans are roasted, normally at around 200°C. The most commonly occurring methods used for roasting in industry are drum roasters and fluidised bed roasters [2, 13]. In a drum roaster, the coffee beans are placed in a rotating cylinder, which is attached to a hot air inlet [2]. In this roaster, heat is mainly transferred due to conduction from bean-bean contact or from inlet-bean interactions [2]. With the fluidised bed roaster, the beans are placed in a chamber where hot air is blown vertically through the bed of beans [2]. This causes the bean to become suspended in the air, and the main heat transfer mechanism in this roaster is convection from the air to the bean [2].

The roasting process can be divided into three phases: drying, flavour and colour development, and cooling. In the drying phase, the evaporation of water from the bean's biological cells brings the moisture content down from an initial value of 12% to approximately 2% by weight [2]. The bean's temperature rises rapidly, and swelling occurs. This is generally the longest phase of the roast and lasts about 3-6 minutes [2].

Following the drying phase, a phase occurs where flavour and colour start to develop in the bean [2, 51]. Once the bean's temperature reaches nearly 200°C, exothermic reactions in the bean, such as Maillard reactions, can begin [2, 12, 17, 34, 51]. These reactions generate the colour, flavour, and aromas that are typical of roast coffee beans [2, 51]. Additionally, carbon dioxide is generated within the bean, causing the bean to further swell [51]. At some critical point in this stage, one can observe "First Crack" [21]. While a detailed physical explanation for First Crack has not yet been found, a distinct popping sound can be heard, not unlike the sound of popping popcorn [21, 51]. After First Crack, the bean's colour continues to darken and its aromas continue to enhance [21, 51]. A "Second Crack" can then occur, similar to a snapping sound [21, 51], when the bean has become a very dark colour. For industrially-roasted coffee, the roasting process generally ends between First and Second Crack [21]. Before First Crack, the aromas and flavours of the bean have not fully developed [51], and after Second Crack, the bean is considered to be burnt with all desirable aromas and flavours lost and undesirable aromas generated [2].

When the required amount of flavour and colour development has occurred, further roasting is prevented by transferring beans to a second chamber for the cooling phase [2]. Usually, water is added to the chamber (called "quenching") to quickly stop the roasting process [2]. However, some roasters do not quench beans, but instead cool the beans using circulated cool air [2]. While quenching does add some extra moisture

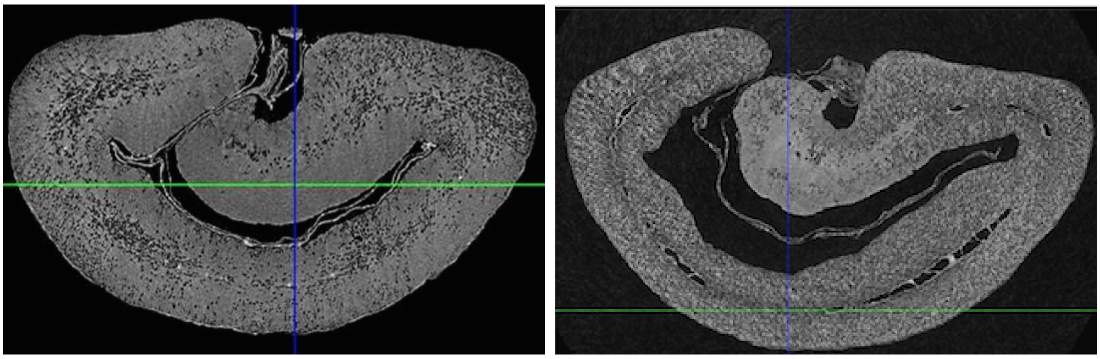

(a) (b)

Figure 1.1: SEM images of a cross-section of a typical coffee bean (a) before and (b) after roasting. Note that these two beans are not pictured at the same scale. Image courtesy of Jacobs Douwe Egberts.

in the bean, a target moisture of less than 5% is typically achieved [2]. This cooling phase occurs soon after First Crack to achieve a lighter roast, or near Second Crack for a darker roast [2].

Figure 1.1 shows how the bean's porous structure changes during roasting. The amount of bulk material decreases during roasting due to evaporation and reactions. We also see that in the bean prior to roasting (a "green" bean), the pores are small, while a roasted bean's pores are larger and mostly filled with gas.

1.3 The Structure of a Coffee Bean

A green coffee bean structure can be described as an intercellular matrix consisting of cellulose, glacto-mannans, arabinogalactans, lignin, bound water, and other structural carbohydrates [4, 51]. Within this structure, there are pockets of biological cells containing water, oils, proteins, sugars, cell carbohydrates, etc. [4, 51]. On roasting, the cell structures are destroyed and many of their contents react through a number of pathways [51]. In particular, those of the Maillard reactions [12, 17, 34] produce a wide variety of reactants, many of which are the flavour and aroma small molecules in addition to some larger polymerised molecules. Structural carbohydrates of the intercellular matrix are also degraded, in part by pyrolysis reactions [51]. Carbon dioxide is produced by these reactions and the bean's porosity is increased due to both the destruction of the cells and the degradation of the intercellular matrix [2]. At the same time, the water within the cells evaporates and becomes water vapour.

The carbon dioxide creation and water evaporation result in high gas pressures that cause the cells to expand. This expansion causes the nano-porous walls of the

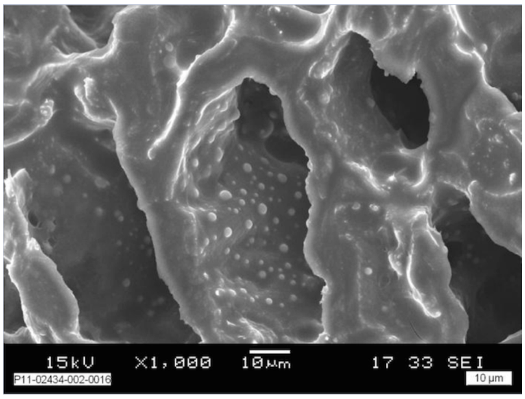

Figure 1.2: SEM image of the interior of a typical coffee bean after 40 seconds of roasting. Image courtesy of Jacobs Douwe Egberts.

cells to deform, allowing gas to flow through them more easily. Figure 1.2 shows a typical coffee bean's porous structure after roasting. We can clearly see the pores surrounded by the cellulose wall structure in this scanning electron microscope (SEM) image.

1.4 Summary of Relevant Literature

Before deriving any mathematical models, we examine the current mathematical understanding of the roasting of coffee beans in the literature. One of the most detailed models concerning the roasting of coffee beans has been developed by [13], in which they describe the transport of moisture and heat throughout a coffee bean. This model, however, has a number of simplifications, including the lack of any explicit phase change between liquid water and water vapour in the bean and the assumption that evaporation occurs only at the surface of the coffee bean. Furthermore, the model in [13] uses the concept of "mass diffusivity" to describe the transport of moisture in the coffee bean that was originally derived in [23]. While this may seem natural to do, as both papers deal with evaporation in coffee beans, the work in [23] only addresses what happens when coffee beans are dried at temperatures below the boiling temperature of water. In consequence, papers concerning lower-temperature evaporation (such as wood or food drying models, e.g. [49]) are not immediately applicable for higher-temperature evaporation, such as in the roasting of coffee beans.

Multiphase modelling has also been previously been applied in a variety of food heating problems [6, 11, 22, 26, 33, 38]. One particularly relevant model is the bread baking model seen in [61], where multiphase components are explicitly stated along with typically observed gas permeability functions. Furthermore, this multiphase setting is seen as a natural framework to model the coffee bean roasting process. While the majority of the processes discussed in [61] will be omitted from preliminary multiphase models (such as those presented in Chapters 2 and 3), they will be considered in our extended models (such as those presented in Chapters 5 and 6).

One process that is examined in detail in the literature is the evaporation rate and subsequent drying mechanisms. Mathematical models describing drying have been explored previously (see e.g. [43, 53, 56]) and have been used to model the drying of wood, bricks, and other materials. However, due to the impermeable cellulose structure within a coffee bean, the water vapour created in its biological cells cannot be easily released into the roasting environment. In consequence, our multiphase models are in the parameter regime where evaporation occurs significantly faster than the time it takes for water vapour to diffuse to the surface of the bean. Additionally, many evaporation mechanisms used in the drying of organic materials (such as wood and food products) incorporate "sorption isotherms" and water activity into the evaporation rate (see e.g. [9, 29, 40, 44]). The sorption isotherm is seen as an important concept to include in evaporation dynamics, and will be incorporated into our multiphase models in Chapter 4. However, the sorption isotherm will not be considered in the preliminary models seen in Chapters 2 and 3.

In addition to the evaporation of water, there are a myriad of other chemical reactions that occur in a roasting coffee bean. While attempting to examine each chemical reaction is beyond the scope of this thesis, we are still motivated to examine the dominant chemical reaction "groups" that are linked to flavour and aroma development. One noteworthy reaction group consists of the Maillard reactions [17, 34], which are linked to the browning process and the reduction of sugars, but many other reactions also occur. A general framework of chemical pathways occurring via the reduction of sugars is proposed by [12, 58], which examines caramelisation, Maillard reactions, and sucrose hydrolysis. In consequence, we will incorporate this framework for these reactions in our extended models (such as those presented in Chapter 5).

Using the multiphase framework seen in Chapters 2-5, we will provide a further extension to these models by incorporating deformations and stresses in the cellulose material. Similar concepts have been used in other multiphase models seen in the literature (c.f. [48, 61]) to describe baking and drying processes. By incorporating a model for poroviscoelastic materials (c.f. [24]), we extend our previous models to predict the stresses and deformations in a roasting coffee bean. We also make use of experimental data provided by [45, 62] to determine relevant parameter values in our models.

1.5 Overview of Thesis

In this thesis, we are motivated to derive multiphase mathematical models that describe specific dynamics and processes observed in a roasting coffee bean. In Chapter 2, we derive two preliminary models from first principles using conservation equations, where multiphase flow in porous media and mass transfer due to evaporation are seen as important. These models will incorporate the production of carbon dioxide gas, latent heat due to evaporation within the bean, and the changing porosity of the bean. Once a full model is derived, reasonable simplifications are made (in particular, we neglect carbon dioxide production) in order to gain a preliminary understanding of the general model behaviour. Numerical solutions to this model suggest that a "drying front" propagates through to the centre of the bean and that there exists a ridge of high pressure water vapour near the drying front. We are able to fit solutions of this model to experimental data shown in [13].

Following the derivation of this multiphase model, we are motivated to examine qualitative features of solutions to this system of PDEs in Chapter 3. In particular, we examine the drying process in this simplified multiphase model in order to compare and contrast its results with existing models in the literature. By obtaining asymptotic expansions for these quantities in physically relevant limits of the model parameters, we are able to determine the qualitative behaviour of the outer and inner regions, as well as the dynamics of the drying front. Although a number of simplifications and scalings are used, we take care not to discard aspects of the model which are fundamental to the roasting process. Indeed, we find that for all of the asymptotic limits considered, our approximate solutions faithfully reproduce the qualitative features evident from numerical simulations of the full model. From these asymptotic results, we have a better qualitative understanding of the drying front (which is hard to resolve precisely in numerical simulations), and hence, of the various mechanisms at play including heating, evaporation, and pressure changes.

One notable physical process in our multiphase models is the evaporation rate, which is critical to determine the average moisture content which we compare with experimental data. In Chapter 4, we modify our models by having evaporation rates include more physically suitable processes. In particular, we incorporate water activity into our evaporation model to more accurately address how water changes phase from liquid to vapour within a coffee bean structure. We then modify the existing multiphase model to include a sorption isotherm, linked to the coffee bean's water activity function, and discuss the quantitative differences between the two models.

In Chapter 5, we extend the aforementioned multiphase models in a number of ways. Firstly, we view evaporation as a multistep process that accounts for a distribution of chemical reactions. Secondly, to account for the many chemical reactions present within the roasting bean, we also include a simplified sugar chemical pathway model representative of key reaction groups that occur during the roasting process. Finally, a spherical "shell" geometry is used to provide a more realistic representation of the coffee bean's geometry. Since this multiphase model has many non-dimensional groupings with unknown values, we carry out a sensitivity analysis to show what qualitative features change in this model when various parameter values are modified.

One final extension of these multiphase models is to incorporate the deformations that occur in a roasting coffee bean. Specifically, we examine the build-up of gas pressure inside a bean and the connection thereof to macro-scale deformations in the cellular matrix, such as First Crack. By modelling the solid cellulose structure as a poroviscoelastic material with temperature-dependent parameters, we are able to examine the stresses and deformations in the cellulose structure, finding how various parameter regimes influence the qualitative behaviour of the solutions to the constitutive poroviscoelastic equations.

We conclude by summarising the key findings in this thesis. In particular, we return to the original premise of explaining the phenomena observed in industrially roasted coffee beans. This, in turn, motivates us to consider further phenomena seen when coffee beans are roasted and discuss possible future directions of mathematical modelling that address phenomena that have been neglected here.

1.6 Statement of Originality

At the time of submission, three papers [14, 15, 16] has been published from this thesis, containing the work in Chapters 2, 3, 4, and 5. These papers were co-authored by N. T. Fadai, C. P. Please, and R. A. Van Gorder (supervisors), along with Z. Akram, F. Guilmineau, and J. Melrose for [14] and J. Melrose and A. Schulman for [15], who were employees at Jacobs Douwe Egberts. SEM images in this chapter were provided by Jacobs Douwe Egberts; this is acknowledged in the figure captions. The experimental data in Chapter 5 was collected by Z. Akram; this is acknowledged in the tabular data. The models' analysis and numerical solutions were carried out by N. T. Fadai under the supervision of C. P. Please and R. A. Van Gorder.

1.7 Acknowledgement of Funding

This thesis is based on work supported by the EPSRC Centre for Doctoral Training in Industrially Focused Mathematical Modelling (EP/L015803/1) in collaboration with Jacobs Douwe Egberts. My thanks go to Jacobs Douwe Egberts for financial support and the opportunity to work on-site during parts of this project.

Chapter 2

Heat and Mass Transfer Models in Coffee Bean Roasting

2.1 Introduction

This chapter is mainly comprised of results shown in [15]. Understanding heat, moisture and mass transport during the roasting of a coffee bean is essential to identifying how the colour and flavours are produced. This chapter first considers a slightly simplified version of an existing heat and moisture transport model proposed by [13], denoted as the Bulk Moisture Model. We show that this model can be fitted well to data for the moisture content of a coffee bean but has some stability issues and lacks some important physical mechanisms. Building on these ideas, a new model is derived from conservation equations. This new model (the Local Moisture Model) focuses on dividing the bean into solid, liquid, and gas volume fractions, in order to capture the different thermal and mechanical properties of the various observed materials. This Local Moisture Model is then simplified; in particular, issues of CO_2 production are neglected, as there is currently insufficient experimental data to fit parameters. This simplified Local Moisture Model, called the Multiphase Model, is fitted to the same experimental data as presented by [13]. It predicts significantly different internal structure and behaviour of the moisture than the Bulk Moisture Model, while both show qualitatively similar average behaviour. A detailed comparison of the two models is provided, in order to cast light on the relative importance of various heat and mass transfer mechanisms inherent in coffee bean roasting.

2.2 The Bulk Moisture Model

We first review a model specifically describing coffee roasting, presented in [13]. It focuses on the heat transport within the bean, and the bulk "moisture" content present within the bean. The moisture is described as one phase with no distinction between vapour and liquid within the bean. The model consists of a coupled system of partial differential equations (PDEs) with flux boundary conditions that model the transfer of heat and moisture between the bean and the ambient environment. The model does not incorporate latent heat within the bean itself, but does account for it at its surface. A main consideration of the model is the external geometry of the bean and the PDEs are solved in a realistic shapes by using the commercial package COMSOL [7].

The model presented here is very similar to the model presented in [13], but with a few simplifications. Firstly, all the parameters in the model, except the mass diffusivity D, are held constant. Secondly, spherical geometry is used instead of a semi-elliptical geometry or a digitized geometry of a realistic coffee bean. Finally, we will solve the system in MATLAB [35] using a finite difference scheme in space and a stiff ODE solver in the time component, rather than in COMSOL.

2.2.1 Dimensional form of the Bulk Moisture Model

Consider the coupled system of PDEs

$$\rho_b C_{pb} \frac{\partial T^*}{\partial t^*} + \nabla \cdot (-K_b \nabla T^*) = 0 \quad \text{and} \quad \frac{\partial c^*}{\partial t^*} - \nabla \cdot (D^* \nabla c^*) = 0. \tag{2.1}$$

Here, T^* and c^* represent the dimensional temperature and moisture content in the bean respectively, and (2.1) is based on conservation of heat and water. Additionally, the thermal parameters ρ_b, C_{pb}, and K_b refer to the density, specific heat capacity, and thermal conductivity, respectively, of a "bulk" coffee bean. These thermal properties incorporate the fact that a coffee bean contains solid, liquid, and gas phases, and are therefore different than a dry bean. Here, we will assume that all thermal parameters of the bean are constants, except for the mass diffusivity term D^*, which is a strong function of temperature and moisture. In particular, we define

$$D^*(T^*, c^*) = \eta_1 \exp\left(-\frac{E_a}{RT^*} + \eta_2 \frac{c^*_{avg}}{c_0}\right), \tag{2.2}$$

where c_0 is the initial amount of moisture concentration and the term c^*_{avg} denotes the average moisture concentration over the volume V of the bean, i.e.

$$c^*_{avg} := \frac{1}{V}\int_V c^* \, \mathrm{d}V. \tag{2.3}$$

This mass diffusivity function is taken directly from [13], with the parameters η_1 and η_2 determined experimentally by [23]. On the surface of the bean, we impose the boundary conditions used by [13]:

$$K_b \nabla T^* \cdot \mathbf{n} = h_m(T_\infty - T^*) + \lambda_m D_m m_v \nabla c^* \cdot \mathbf{n}, \tag{2.4}$$

$$D^* \nabla c^* \cdot \mathbf{n} = \beta_m(c_\infty - c^*), \tag{2.5}$$

where $\mathbf{n}$ denotes the outward normal to the surface of the bean. Equation (2.4) means that the thermal flux at the bean's surface is proportional to the difference between the external roasting and actual surface temperature, plus the amount of energy needed to evaporate the moisture on surface out of the bean. Equation (2.5) indicates that the flux of moisture is proportional to the difference between the external and the moisture levels on the surface of the bean. The surface moisture diffusivity D_m is assumed to be constant and independent of D^*. Additionally, the convective heat transfer coefficient h_m, the ambient moisture content and temperature c_∞, T_∞, the mass transfer coefficient β_m, the molar mass of water m_v, and the latent heat of vapourisation λ_m are all assumed to be constant. Finally, we impose uniform initial conditions for the system, namely,

$$T^*(0,r) = T_0 \quad \text{and} \quad c^*(0,r) = c_0 \;\text{ for }\; 0 \le r^* \le L. \tag{2.6}$$

To allow generic behaviour of the model to be determined, we assume spherical geometry for the bean with spherical symmetry and the outer surface at $r^* = L$. Hence, the solution depends only on t^* and r^* and is solved in the region $0 \le r^* \le L$. Additionally, we impose boundedness on T^* and c^* at the centre of the bean where $r^* = 0$. This assumption about the geometry will permit us to gain an understanding of the salient features of the model. The Bulk Moisture Model is therefore defined by the PDE system (2.1), the constitutive equations (2.2)-(2.3), the boundary conditions (2.4) and (2.5), and the initial conditions (2.6).

2.2.2 Non-dimensionalisation of the Bulk Moisture Model

We non-dimensionalise the PDE (2.1) using the scalings

$$T^* = T_0 + (T_\infty - T_0)T, \qquad c^* = c_\infty + (c_0 - c_\infty)c, \tag{2.7}$$

$$r^* = Lr, t^* = \frac{L^2 \rho_b C_{pb}}{K_b} t, \text{ and } D^* = D_0 D. \tag{2.8}$$

Here, D_0 denotes a typical value of the diffusivity; in this case, it was picked as the average diffusivity at the initial and final temperatures with its initial moisture content:

$$D_0 = \frac{D^*(T_\infty, c_0) + D^*(T_0, c_0)}{2}. \tag{2.9}$$

The timescale is the heat diffusion timescale, also known as the Fourier number, which is typically about 130s. We obtain the non-dimensional system

$$\frac{\partial T}{\partial t} = \frac{1}{r^2} \frac{\partial}{\partial r} \left(r^2 \frac{\partial T}{\partial r} \right) \quad \text{and} \quad \frac{\partial c}{\partial t} = \frac{\mathscr{D}}{r^2} \frac{\partial}{\partial r} \left(r^2 D \frac{\partial c}{\partial r} \right). \tag{2.10}$$

Here the dimensionless parameter $\mathscr{D}$ denotes the ratio of mass diffusivity to thermal diffusivity, namely, $\mathscr{D} = \frac{D_0 \rho_b C_{pb}}{K_b}$, while the non-dimensional mass diffusivity is defined as

$$D(T, c) = \frac{\eta_1}{D_0} \exp \left\{ - \frac{E_a/(RT_0)}{1 + \left(\frac{T_\infty}{T_0} - 1 \right) T} + \eta_2 \frac{c_\infty}{c_0} + 3\eta_2 \left(1 - \frac{c_\infty}{c_0} \right) \int_0^1 c r^2 \, \mathrm{d}r \right\}. \tag{2.11}$$

On the surface of the bean, the boundary conditions in non-dimensional form become

$$\frac{\partial T}{\partial r} = \mathrm{Nu}\, (1 - T) + \xi \, \frac{\partial c}{\partial r} \quad \text{and} \quad \frac{\partial c}{\partial r} = -\mathrm{Sh} \, \frac{c}{D} \quad \text{at} \quad r = 1. \tag{2.12}$$

The Nusselt and Sherwood numbers, which are sometimes referred to as the heat and mass transfer Biot numbers, are defined as $\mathrm{Nu} = \frac{h_m L}{K_b}$ and $\mathrm{Sh} = \frac{\beta_m L}{D_0}$, respectively, and our final dimensionless group is defined as

$$\xi = D_m \frac{\lambda_m (c_0 - c_\infty) m_v}{K_b (T_\infty - T_0)}. \tag{2.13}$$

One could interpret ξ as a ratio of surface moisture diffusivity to thermal diffusivity from evaporation. Additionally, we impose Neumann boundary conditions at the centre of the bean, i.e.

$$\frac{\partial T}{\partial r} = \frac{\partial c}{\partial r} = 0 \quad \text{at} \quad r = 0. \tag{2.14}$$

Finally, the initial conditions become

$$T(0, r) = 0 \quad \text{and} \quad c(0, r) = 1 \quad \text{for} \quad 0 \leq r \leq 1. \tag{2.15}$$

2.2.3 Numerical Results

We solve the non-dimensionalised model presented in Section 2.2.2 in MATLAB [35] using the method of lines with a central finite difference scheme in the radial component, e.g.

$$\begin{aligned} \nabla^2 T\Big|_{r_i} \approx \frac{1}{(2\Delta r)^2} \Bigg[& \left(2 + \frac{\Delta r}{r_i}\right)^2 (T(r_{i+1}, t) - T(r_i, t)) \\ & - \left(2 - \frac{\Delta r}{r_i}\right)^2 (T(r_i, t) - T(r_{i-1}, t)) \Bigg], \end{aligned} \tag{2.16}$$

and a stiff ODE solver for the time component. This finite difference scheme is second-order accurate in theory; in practise, we see a convergence rate of approximately 1.95 at coarser meshes. We use a stiff adaptive ODE solver in time, namely the MATLAB function `ode15s`, to achieve convergence, as well as 100 spatial meshpoints for good numerical resolution. While other solvers such as COMSOL could have also been used, the transparency of the MATLAB structure and being able to avoid "black-box" solvers made the MATLAB approach desirable. We use parameter values shown in Table 2.1 to obtain the results shown in Figures 2.1 and 2.2. These parameter values are chosen so that solutions of the Bulk Moisture Model agree with the predictions presented in [13].

As we can see in Figure 2.2, the predictions shown in [13] can be reproduced well using the Bulk Moisture Model. Additionally, we observe from Figure 2.1 that the main spatial dependence in temperature and moisture content only occur during the first minute of roasting. After the first minute, the bean's temperature and moisture content become nearly spatially uniform.

It is important to note at this point that the boundary condition in T in (2.12) for this model can drive the system unstable. This is due to the fact that we have opposing signs in the boundary condition. For small t, $T \approx 0$ and $c \approx 1$, making $\frac{\partial T}{\partial r} \approx \mathrm{Nu} - 1.5\xi\mathrm{Sh}$. Therefore, if $\frac{\partial T}{\partial r} < 0$ for long enough time, the surface of the bean will cool the

Parameter	Typical Value	Reference(s)
T_0	20°C (293.15 K)	[13]
c_0	5500 mol/m^3 (approx 12% moisture)	[13]
c_∞	0.5 mol/m^3	[13]
T_∞	200°C (473.15 K)	[13]
D_0	1.63×10^{-10} m^2/s	Determined from other parameters (Section 2.2.2)
E_a	6.69×10^4 J/mol	[13]
R	8.314 J/(mol·K)	Universal gas constant
K_b	0.08 J/(s·m·K)	Chosen to agree with simulated data presented in [13]
ρ_b	850 kg/m^3	[5]
C_{pb}	780 J/(K·kg)	Chosen to agree with experimental data presented in [13]
L	4×10^{-3} m	[15]
η_1	15.01 m^2/s	[23]
η_2	1.74	[23]
λ_m	2.3×10^6 J/kg	[13]
m_v	0.018 kg/mol	Molar mass of water
D_m	5×10^{-10} m^2/s	[13]
h_m	20 J/(s·m^2·K)	Chosen to agree with experimental data presented in [13]
β_m	3.4×10^{-6} m/s	Chosen to agree with experimental data presented in [13]
ξ	7.9×10^{-3}	Determined from other parameters (Section 2.2.2)
Nu	1	Determined from other parameters (Section 2.2.2)
Sh	83	Determined from other parameters (Section 2.2.2)
$\mathscr{D}$	1.4×10^{-3}	Determined from other parameters (Section 2.2.2)

Table 2.1: List of dimensional and non-dimensional parameter values used in the Bulk Moisture Model.

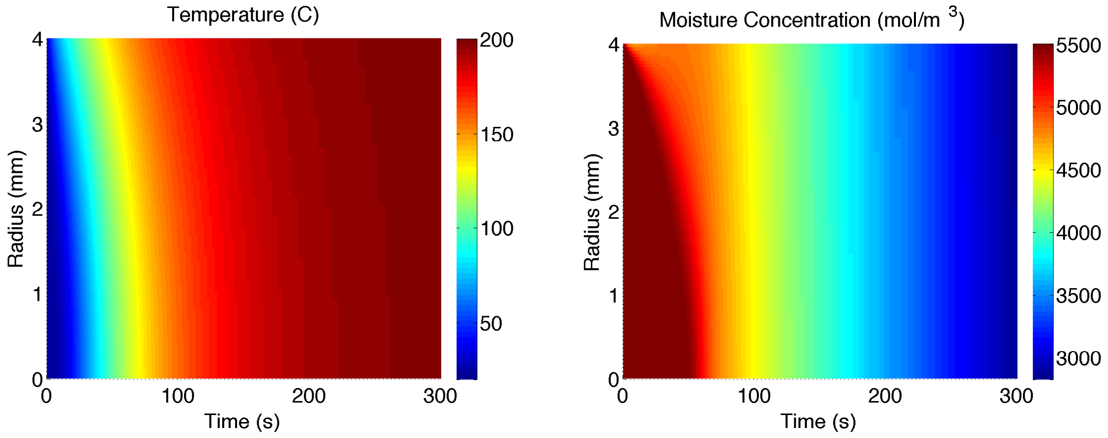

(a) (b)

Figure 2.1: Plots of a 4mm spherical bean's (a) temperature and (b) moisture concentration for 300s of roasting at 200°C from the Bulk Moisture Model, described in equations (2.10)-(2.15). Parameter values are listed in Table 2.1.

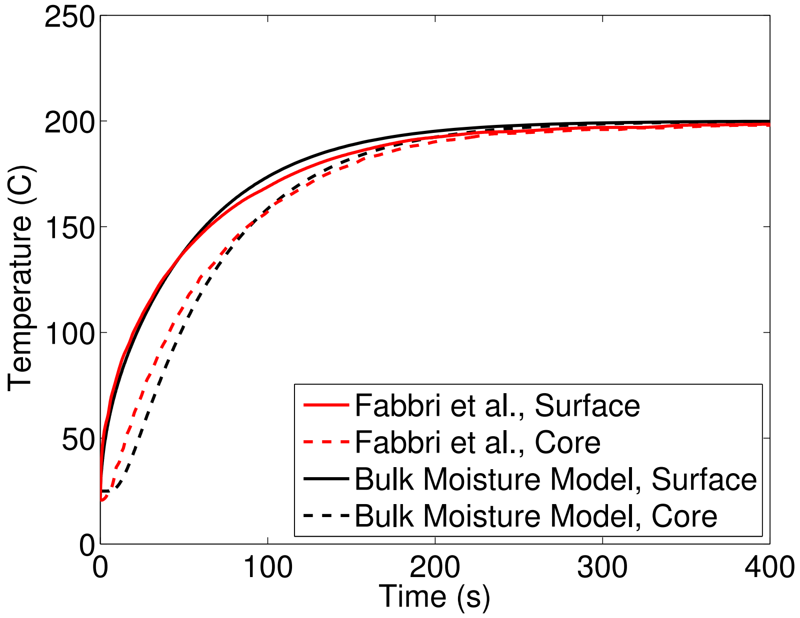

Figure 2.2: Comparison of temperature curves for a 4mm bean at the surface and the centre of the bean during 400s of roasting at 200°C. Predictions reproduced from Fabbri et al. [13] and the Bulk Moisture Model. Parameter values for the Bulk Moisture Model are listed in Table 2.1.

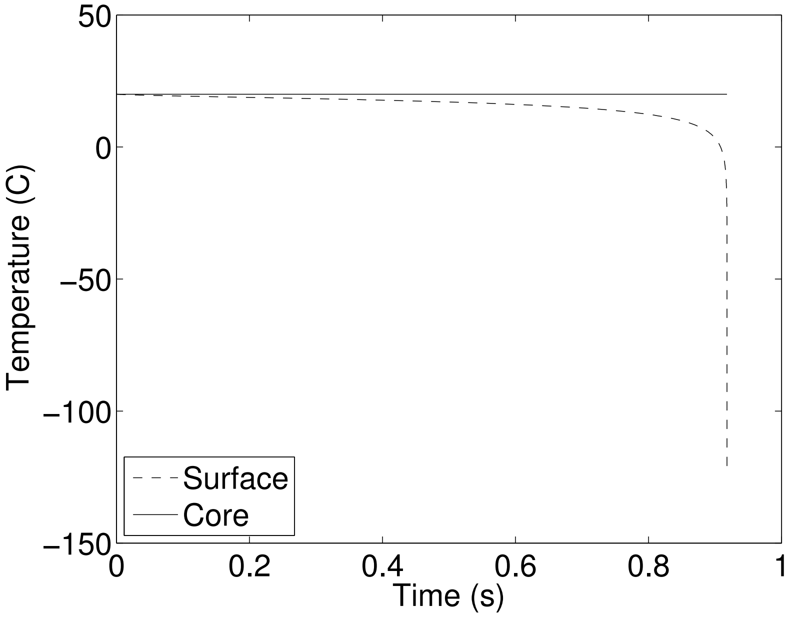

Figure 2.3: Numerical difficulties are seen when solving the Bulk Moisture Model with $\beta_m = 3.5 \times 10^{-6}$ m/s, giving $\mathrm{Sh} = 86$. All other parameters are defined in Table 2.1.

interior rather than heat it. Indeed, if we increase β_m from 3.4×10^{-6} to 3.5×10^{-6}, we see from Figure 2.3 that T becomes singular at $t \approx 1$s when MATLAB tries to solve the system. This may indicate that the boundary value problem consisting of (2.10) and (2.12) becomes ill-posed for certain parameter values. While parameter values that cause this unstable behaviour of the Bulk Moisture Model could be unreasonable in the context of coffee bean roasting, the authors in [13] provide no indication that this may be the case. Regardless, the Bulk Moisture Model does appear to give us undue numerical difficulties in some parameter regimes. Further, since certain features of the model are prescribed rather than derived from first principles, troubleshooting these features is difficult. This motivates us to consider a new model derived directly from conservation equations, which we do in the next section.

2.3 The Local Moisture Model

The Bulk Moisture Model is a good model of the observed behaviour during coffee roasting, as parameters and model elements were specifically chosen for the roasting process. However, the fact that the moisture content was treated as a bulk quantity without specifying the phase state at any point in the bean makes the model limited. This also means that the bulk thermal properties of the bean may be oversimplified for the roasting process. Additionally, latent heat and evaporation effects can happen in the interior of the bean, since the centre of the bean goes above the boiling temperature of water, and therefore such effects need to be incorporated in the model.

Using the bulk roasting model of [13] as motivation, in this section, we derive a roasting model using conservation equations in multiphase physics. Such a model has not previously been considered for coffee bean roasting, although we should remark that similar mathematical modelling that incorporates multiphase flow has been considered for other similar applications, including baking of bread [61], plasma/soil flow and heat transfer in an electric arc furnace [41], burning of timber [42], fire propagation in heterogeneous combustible media [32], and modelling forest fires [52]. In its applications to coffee bean roasting, such a model should incorporate multi-phase flow and CO_2 production. We assume that no deformation of the bean occurs during the roasting process. While deformation of the bean plays a significant role in the roasting of coffee beans, it is useful to consider this simpler problem first, in order to understand the general behaviour. We will consider these effects later in Chapter 6. We also assume that the density of the solid coffee bean and the water are constant.

To aid the derivation process, a simplified diagram (Figure 2.4(a)) shows the different phases existing within a coffee bean. The white squares represent the pockets containing the biological cells, which are partially filled with water (shown in blue). The solid nano-porous structure is shown in brown, and the surface of the bean is represented by the striped region near the top of the figure. Finally, the exterior of the bean, i.e. the roasting chamber, is represented by the red region at the top of the figure.

2.3.1 Derivation of the Dimensional Local Moisture Model

2.3.1.1 Introduction of Multiphase Components

Consider a representative small volume of interest with three phases present: solid (I), liquid (II), and gas (III). In the solid phase, only the coffee bean structure consisting of cellulose and other organic molecules exists. In the liquid phase, only water is present, and in the gas phase, water vapour and CO_2 coexist. Additionally, we will assume that the temperature in all phases is identical for a given volume of interest (i.e. $T_i^* = T^*$, for each phase i). These phases can be summarized using Figure 2.4(b), where the volume of interest is shown within a black circle, with each phase marked.

We define the porosity, ϕ, as the ratio of the total volume the gas and liquid phases occupy to the total representative volume. Similarly, we define the saturation, S, as the volume fraction of liquid water divided by the total volume of water and gas. Therefore, we have

$$\phi = \frac{V_{\text{II+III}}}{V_{\text{I+II+III}}} \quad \text{and} \quad S = \frac{V_{\text{II}}}{V_{\text{II+III}}} = \frac{V_{\text{II}}}{\phi V_{\text{I+II+III}}}. \tag{2.17}$$

Using these two non-dimensional quantities, we can define the volume fractions of phases I, II, and III as $1-\phi$, ϕS, and $\phi(1-S)$, respectively.

2.3.1.2 Conservation of Mass (Solid Phase)

We begin by using conservation of mass for the four species present: solid coffee bean, water, water vapour, and CO_2 gas. For the solid phase, there is no movement in the particles (and hence, no flux), but the particles in the coffee bean structure will react to produce CO_2 gas. This can be described as

$$\frac{\partial}{\partial t^*}\left((1-\phi)\rho_s\right) = -I_c^*, \tag{2.18}$$

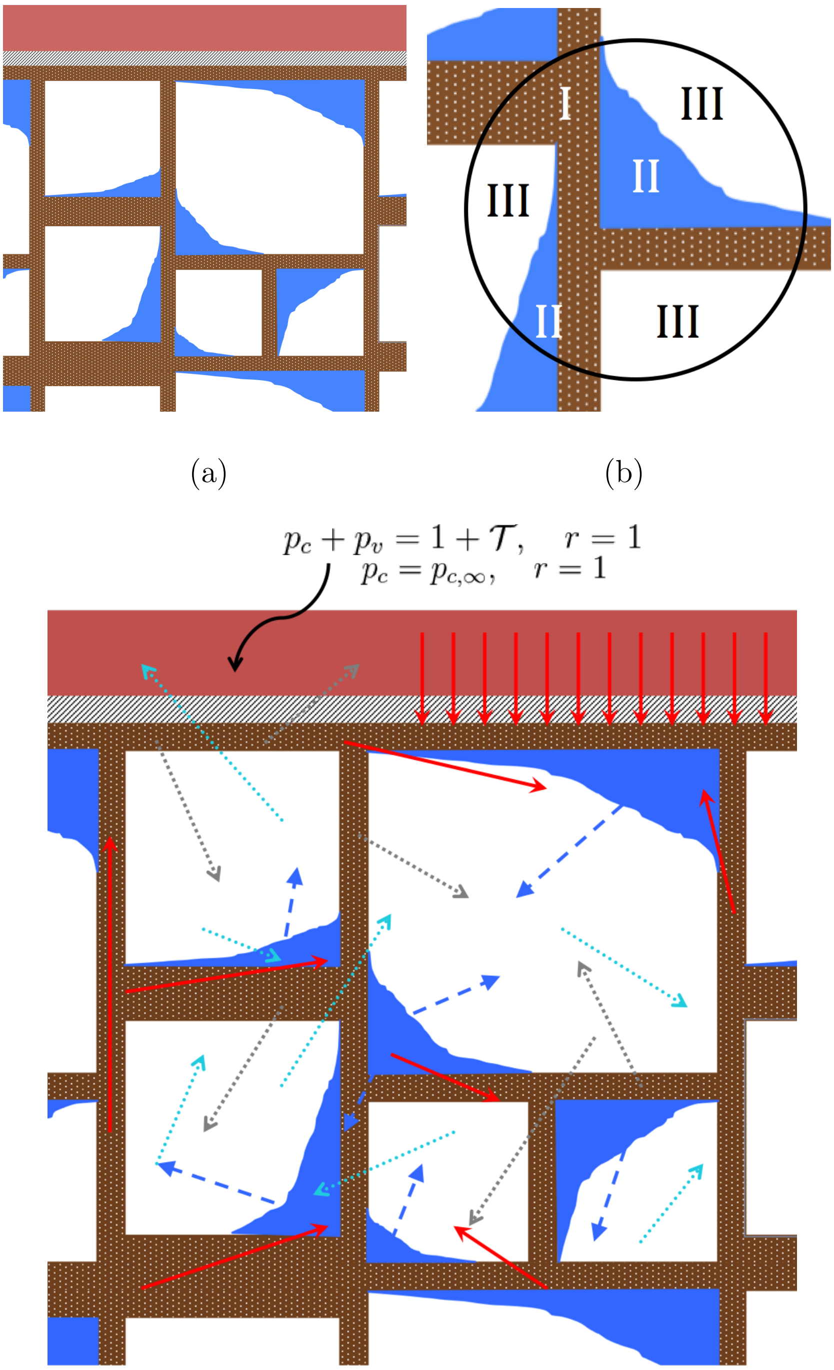

(a) (b)

(c)

Figure 2.4: Schematic representation of a coffee bean structure. (a) The exterior of the bean is shown in red, the surface of the bean is represented by the striped region, and the biological cells are shown as white squares partially filled with blue water. (b) The representative volume of interest is marked by a black circle, with each phase (I, II, and III) labeled. (c) The complete diagram for the Local Moisture Model with boundary conditions. The dark blue arrows represent water transport, the light blue arrows represent water vapour transport, the grey arrows represent CO_2 transport, and the red arrows represent thermal activity.

where ρ_s is the density of the solid phase and I_c^* is the production rate of CO_2 gas. In other words, the porosity of the bean will increase as more CO_2 gas is produced. As a visual aid, a schematic representation of this equation is given in Figure 2.4(c), where the grey arrows represent the production and transport of CO_2 gas.

2.3.1.3 Conservation of Mass (Liquid Phase)

For the liquid phase, we must consider the loss of water due to evaporation as well as the mass flux of water, $\mathbf{j}_w$, to incorporate diffusion. This can be summarized as

$$\frac{\partial}{\partial t^*}\left(\phi S \rho_w\right) + \nabla \cdot \mathbf{j}_w = -I_v^*, \tag{2.19}$$

where ρ_w is the density of water and I_v^* refers to the evaporation rate of water. This means that the local saturation can increase or decrease based on local condensation or evaporation, as well as any movement of liquid from mass flux. Referring to Figure 2.4(c), the transport of water is represented by the dark blue dashed arrows.

2.3.1.4 Conservation of Mass (Gas Phase)

In the gas phase, we incorporate mass fluxes $\mathbf{j}_v$ and $\mathbf{j}_c$ to allow for the transport of water vapour and CO_2 gas, as well as account for the production rates of CO_2 gas and water vapour. Additionally, we use the ideal gas law to define $\rho_v = p_v m_v / RT^*$ and $\rho_c = p_c m_c / RT^*$, where m_v and m_c are the molar masses of water and CO_2, respectively, and p_v and p_c are the partial pressures of water vapour and CO_2 gas, respectively. This gives us

$$\frac{\partial}{\partial t^*}\left(\phi(1-S)\frac{p_v^* m_v}{RT^*}\right) + \nabla \cdot \mathbf{j}_v = I_v^*, \tag{2.20}$$

$$\frac{\partial}{\partial t^*}\left(\phi(1-S)\frac{p_c^* m_c}{RT^*}\right) + \nabla \cdot \mathbf{j}_c = I_c^*. \tag{2.21}$$

Similar to the water equation, these mass conservation equations for the gas species tell us that the partial pressure of a gas will change based on any gas production in the solid or liquid phases, as well as any transport through the nano-porous structure. Again, we can refer to Figure 2.4(c) which represents the transport of water vapour (shown in light blue) and CO_2 gas (shown in grey).

2.3.1.5 Derivation of Mass Flux Terms

The mass fluxes of gases are due to the total gas pressure gradient and binary diffusion ([3, 39]). Additionally, the water transport is due to the water pressure gradient, which is assumed to be equal to the total gas pressure gradient, and moisture diffusion ([3, 39]). We take these directly from [61], using

$$\mathbf{j}_v^* = -\frac{\rho_v^* k_g^*}{\mu_g^*}\nabla(p_v^* + p_c^*) - m_v M^* D_{\text{eff,g}}^* \nabla \chi_v, \tag{2.22}$$

$$\mathbf{j}_c^* = -\frac{\rho_c^* k_g^*}{\mu_g^*}\nabla(p_v^* + p_c^*) - m_c M^* D_{\text{eff,g}}^* \nabla \chi_c, \tag{2.23}$$

$$\mathbf{j}_w^* = -\frac{\rho_w k_w^*}{\mu_w^*}\nabla(p_v^* + p_c^*) - \rho_w D_w^* \nabla \left(\frac{\phi S \rho_w}{(1-\phi)\rho_s}\right). \tag{2.24}$$

Here, k_g and k_w denote the permeabilities of gas and water within the nano-porous coffee bean structure, while μ_g and μ_w represent the dynamic viscosities of gas and water in the bean. Additionally, $D_{\text{eff,g}}^*$ and D_w^* are, respectively, the effective diffusivities of gas and water due to "standard" diffusion, i.e. Fick's Law [18].

It is important to note that M^* denotes the molar density of the gas mixture, i.e.

$$M^* = \rho_v^*/m_v + \rho_c^*/m_c = \frac{p_v^* + p_c^*}{RT^*}. \tag{2.25}$$

Since the molar fractions χ_v and χ_c sum to one, we can substitute $\nabla\chi_c = -\nabla\chi_v$ and, from the definition of the molar fraction, we have

$$\chi_v = \frac{\rho_v^*/m_v}{\rho_v^*/m_v + \rho_c^*/m_c} = \frac{p_v^*}{p_v^* + p_c^*}. \tag{2.26}$$

More care would need to be taken with molar fractions should a third gas species be included. The second term in $\mathbf{j}_w$ represents an "unforced" diffusion term of water, which is driven by any change in moisture content. Here, moisture content is defined as the mass ratio of water to dry solids. Using our definitions of volume fractions in (2.17), we can define moisture content as $\phi S \rho_w/(1-\phi)\rho_s$.

2.3.1.6 Conservation of Energy

We note, from [25, 59, 61], that each phase i contains enthalpy $\rho_i^* C_{pi} V_{f,i} T^*$ and contributes a diffusive heat flux $-K_i V_{f,i} \nabla T^*$. Additionally, from [25, 59, 61], advection of the enthalpy in phase i is given by $\mathbf{v}_i \rho_i C_{pi} V_{f,i} T^*$. Here, $V_{f,i}$ represents the volume fraction for each phase and the velocity field $\mathbf{v}_i$ is given by $\mathbf{v}_i = \frac{\mathbf{j}_i}{\rho_i}$. Finally, we note that the rate at which energy contributes to the production of CO_2 gas and evaporation of water is given by $\lambda_c I_c^*$ and $\lambda_v I_v^*$ respectively, where λ_v is the latent heat of vapourisation of water and λ_c denotes the energy required for the solid phase to react and produce CO_2 gas. Since we do not track the fine scale structure of the bean, it makes sense to consider a locally volume averaged formulation in the standard way [25, 59]. This can be summarised by

$$\begin{aligned}\frac{\partial}{\partial t^*}\left(\sum_i \rho_i^* C_{pi} V_{f,i} T^*\right) + \nabla \cdot \left(\sum_i \mathbf{v}_i \rho_i C_{pi} V_{f,i} T^*\right) \\ - \nabla \cdot \left(\sum_i K_i V_{f,i} \nabla T^*\right) = -\lambda_v I_v^* - \lambda_c I_c^*.\end{aligned} \tag{2.27}$$

All of these thermal processes can be summarised with a schematic representation given in Figure 2.4(c), where the red arrows denote thermal activity.

2.3.1.7 Derivation of Evaporation and Production Rates

For the evaporation rate I_v^*, we use Langmuir's equation [31] based on the difference between the actual partial pressure and the equilibrium partial pressure, given by

$$I_v^* = (p_{ST}^*(T^*) - p_v^*)\sqrt{\frac{m_v}{2\pi R T^*}}\frac{\text{Surface Area}}{\text{Volume}}. \tag{2.28}$$

This equilibrium pressure $p_{ST}^*(T^*)$ can be calculated using a steam table. However, we need to also incorporate the fact that evaporation occurs at the interface between the liquid and gas phases. The size of this interface is dictated by the surface-to-volume ratio. For example, if either of their related volume fractions should be zero, evaporation cannot occur. If we assume that the geometry of the liquid phase is roughly spherical, then we can approximate this ratio as

$$\frac{\text{Surface Area}}{\text{Volume}} = \frac{3}{\ell} V_{f,\text{II}} V_{f,\text{III}} = \frac{3}{\ell}\phi^2 S(1-S), \tag{2.29}$$

where ℓ is a typical radius of a biological cell. Combining all of these terms together gives us

$$I_v^* = 3\phi^2 S(1-S)\frac{p_{ST}^*(T^*) - p_v^*}{\ell}\sqrt{\frac{m_v}{2\pi R T^*}}. \tag{2.30}$$

The steam table pressure for pure water can be approximated by, from [10],

$$p^*_{ST}(T^*) = A_1 \exp\left(A_2 - \frac{A_3}{T^*}\right). \tag{2.31}$$

More complicated equilibrium vapour pressures, such as the *sorption isotherm* [29], could also be considered. We will discuss these ideas further in Chapters 4 and 5. For I^*_c, the kinetics of the CO_2-producing reaction are not as obvious as the evaporation rate. If one assumes that this reaction can only take place on the interface between the solid and gas phases, then we could approximate this production rate using Langmuir's equation [31] as

$$I^*_c = 3\phi(1-\phi)(1-S)\frac{p^*_{eq}(T^*) - p^*_c}{\ell}\sqrt{\frac{m_c}{2\pi R T^*}}. \tag{2.32}$$

The equilibrium pressure of this reaction, $p^*_{eq}(T^*)$, should only allow the reaction to proceed in a single direction (i.e. no solid can be created from CO_2 gas). Additionally, it is quite possible that the reaction assumes a completely different form, such as ones proposed in Chapter 5. In such a case, the expression for I^*_c would need to be modified.

2.3.2 Boundary Conditions for the Local Moisture Model

For the heat boundary condition, we assume that the principal means of heat transport away from the boundary is due to convection. This gives rise to our dimensional boundary condition in T^* on the surface of the bean, [1]

$$\left(\sum_i K_i V_{f,i} \nabla T^*\right) \cdot \mathbf{n} = \left(\sum_i h_i V_{f,i}\right)(T_\infty - T^*). \tag{2.33}$$

Additionally, it is quite possible that there are additional heat fluxes to consider, notably a term involving the flux of water. For this model, we will assume that evaporation of water occurs only inside the bean and not directly on the surface. Therefore, a heat flux term due to moisture, like the one used in the Bulk Moisture Model, is not included. Additionally, we will assume that water cannot be transported outside of the coffee in its liquid phase. This corresponds to having a Neumann boundary condition in ϕS:

---

[1] It is important to note that greater care may be needed for this flux condition. For instance, the roasting chamber is assumed to only contain gas, and therefore might not be reasonable to contain terms with volume fractions like $h_i V_{f,i}$. Consequently, it may be more realistic to have a "bulk" convective coefficient. This is omitted from this model, but discussed in Chapter 5.

$$\nabla(\phi S) \cdot \mathbf{n} = 0 \quad \text{at} \quad r^* = L. \tag{2.34}$$

For our boundary condition for the gases, we assume that the number of moles of gas in the roasting chamber (n), as well as the volume of the roasting chamber itself (V), stay constant during the roasting process, i.e. $\frac{\sum_i p_i^*}{T^*} = \frac{nR}{V}$. From the ideal gas law, this means that the ratio of roasting temperature to initial temperature $\left(\frac{T_\infty}{T_0}\right)$ is identical to the ratio of the total gas pressure in the roasting chamber to the initial total gas pressure, $\frac{\sum_i p_i^*}{p_0}$. Additionally, this means that we must also declare one of the partial pressures of gas at the surface of the bean; for this model, we choose to declare the partial pressure of CO_2 gas at the boundary. This is equivalent to saying that

$$p_c^* + p_v^* = \frac{T_\infty}{T_0} p_0 \quad \text{and} \quad p_c^* = p_{c,\infty}^* \quad \text{at} \quad r^* = L. \tag{2.35}$$

Since the beans have been stored at ambient temperature and a constant environment before going in to the roaster, we impose spatially uniform initial conditions for the system, namely, $T^* = T_0$, atmospheric vapour pressure ($p_v^* = p_{v0}^*$), and CO_2 pressure ($p_c^* = p_{c0}^*$).

The complete model is represented in Figure 2.4(c). Dimensional parameters (and typical values) are given in Table 2.2.

2.3.3 Non-dimensionalisation of the Local Moisture Model

We non-dimensionalise the variables in the PDE system, using

$$\begin{aligned} &T^* = T_0 + (T_\infty - T_0)T := T_0(1 + \mathscr{T}T), \\ &p_v^* = p_0 p_v, \; p_c^* = p_0 p_c, \; r^* = Lr, \quad \text{and} \quad t^* = \theta t; \end{aligned} \tag{2.36}$$

similarly, all dimensional functions are non-dimensionalised by dividing by a typical function value, i.e. $f^* = f_0 f$. The timescale, θ, is chosen to be the time for evaporation so that $\theta = \frac{\rho_w}{I_{v0}}$, where

$$I_{v0} = \frac{3p_0}{\ell} \sqrt{\frac{m_v}{2\pi R T_0}}. \tag{2.37}$$

The full model in spherical coordinates can then be written in the following form. First, the mass conservation equations become

$$\frac{\partial \phi}{\partial t} = \frac{\kappa_1}{\alpha_1} I_c, \tag{2.38}$$

Parameter	Typical Value	Reference(s)
A_1	133.3 Pa	[10]
A_2	20.39	[10]
A_3	5132 K	[10]
C_{pc}	900 J/(kg·K)	[15]
C_{ps}	450 J/(kg·K)	Chosen to agree with experimental data presented in [13]
C_{pv}	1900 J/(kg·K)	[15]
C_{pw}	4200 J/(kg·K)	[15]
$D_{\text{eff},g0}$	-	Not used
D_{w0}	-	Not used
h_c	-	Not used
h_v	16 J/(s·m^2·K)	Chosen to agree with experimental data presented in [13]
I_{c0}	3.4×10^7 kg/(m^{3}s)	Determined from other parameters (Section 2.3.3)
I_{v0}	2.2×10^7 kg/(m^{3}s)	Determined from other parameters (Section 2.3.3)
K_c	0.015 J/(s·m·K)	[15]
K_s	0.037 J/(s·m·K)	Extrapolation of [5]
K_v	0.016 J/(s·m·K)	[15]
K_w	0.58 J/(s·m·K)	[15]
k_{g0}	1.6×10^{-19} m^2	Chosen to agree with experimental data presented in [13]
k_{w0}	-	Not used
L	0.004 m	[15]
m_c	0.044 kg/mol	Molar mass of CO_2
m_v	0.018 kg/mol	Molar mass of water
p_0	101325 Pa	Atmospheric pressure
R	8.314 J/(mol·K)	Universal gas constant
T_0	293.15 K	[15]
T_∞	473.15 K	[15]
ℓ	15×10^{-6} m	[15]
λ_c	-	Not used
λ_v	2.3×10^6 J/kg	[13]
μ_{g0}	1.2×10^{-5} kg/(s·m)	[15]
μ_{w0}	-	Not used
ρ_s	850 kg/m^3	[5]
ρ_w	1000 kg/m^3	Density of water
θ	4.6×10^{-5} s	Determined from other parameters (Section 2.3.3)
σ	$0 \leq \sigma \leq 1$	Initial saturation
ϕ_0	0.5	Constant porosity
$p_{c,0}$	$0 \leq p_{c,0} \leq 1$	Initial partial pressure of CO_2

Table 2.2: Typical values for dimensional parameters used in the Local Moisture Model.

$$\frac{\partial}{\partial t}\left(\phi S\right) = -I_v + \kappa_3 \mathscr{D}_3 \nabla \cdot \left(\frac{k_w}{\mu_w} \nabla (p_v + p_c) + \frac{1}{\alpha_1} \mathscr{D}_2 \nabla \left(\frac{\phi S}{1-\phi} \right) \right), \tag{2.39}$$

$$\begin{aligned} \frac{\partial}{\partial t}\left(\frac{\phi(1-S)p_v}{1+\mathscr{T}T} \right) = \frac{1}{\alpha_2} I_v + \mathscr{D}_3 \nabla \cdot \left(\frac{k_g}{\mu_g} \frac{p_v}{1+\mathscr{T}T} \nabla (p_v + p_c) \right. \\ \left. + \mathscr{D}_1 \frac{(p_v+p_c) D_{\mathrm{eff,g}}}{1+\mathscr{T}T} \nabla \left(\frac{p_v}{p_v+p_c} \right) \right), \end{aligned} \tag{2.40}$$

$$\begin{aligned} \frac{\partial}{\partial t}\left(\frac{\phi(1-S)p_c}{1+\mathscr{T}T} \right) = \frac{\kappa_1\kappa_2}{\alpha_2} I_c + \mathscr{D}_3 \nabla \cdot \left(\frac{k_g}{\mu_g} \frac{p_c}{1+\mathscr{T}T} \nabla (p_v + p_c) \right. \\ \left. - \mathscr{D}_1 \frac{(p_v+p_c) D_{\mathrm{eff,g}}}{1+\mathscr{T}T} \nabla \left(\frac{p_v}{p_v+p_c} \right) \right). \end{aligned} \tag{2.41}$$

The energy conservation equation becomes

$$\frac{\partial}{\partial t}(\text{Enthalpy}) - \nabla \cdot (\text{Advection}) = -\gamma I_v - \gamma \kappa_1 \kappa_4 I_c + \mathscr{T} \nabla \cdot (\text{Conduction}), \tag{2.42}$$

where

$$\begin{aligned} \text{Enthalpy} = \alpha_1 \mathscr{C}_1 (1-\phi)(1+\mathscr{T}T) + \phi S (1+\mathscr{T}T) \\ + \alpha_2 \mathscr{C}_2 \phi (1-S) p_v + \frac{\alpha_2 \mathscr{C}_3}{\kappa_2} \phi (1-S) p_c, \end{aligned} \tag{2.43}$$

$$\begin{aligned} &\text{Advection} \\ &= \kappa_3 \mathscr{D}_3 \phi S (1+\mathscr{T}T) \left(\frac{k_w}{\mu_w} \nabla (p_v+p_c) + \frac{1}{\alpha_1} \mathscr{D}_2 \nabla \left(\frac{\phi S}{1-\phi} \right) \right) \\ &\quad + \alpha_2 \mathscr{C}_2 \mathscr{D}_3 \phi (1-S) \left(\frac{k_g}{\mu_g} p_v \nabla (p_v+p_c) + \mathscr{D}_1 (p_v+p_c) D_{\mathrm{eff,g}} \nabla \left(\frac{p_v}{p_v+p_c} \right) \right) \\ &\quad + \frac{\alpha_2 \mathscr{C}_3 \mathscr{D}_3}{\kappa_2} \phi (1-S) \left(\frac{k_g}{\mu_g} p_c \nabla (p_v+p_c) - \mathscr{D}_1 (p_v+p_c) D_{\mathrm{eff,g}} \nabla \left(\frac{p_v}{p_v+p_c} \right) \right), \end{aligned} \tag{2.44}$$

$$\text{Conduction} = \left(\zeta_1 (1-\phi) + \zeta_2 \phi S + \zeta_3 \phi (1-S) + \zeta_4 \phi (1-S) \right) \nabla T. \tag{2.45}$$

The heat flux condition, (2.33), becomes

$$\frac{\partial T}{\partial r} = \mathrm{Nu}_v \zeta_3 (1-T) \frac{\phi (1-S)(1+H)}{\zeta_1 (1-\phi) + \zeta_2 \phi S + (\zeta_3 + \zeta_4) \phi (1-S)}, \tag{2.46}$$

while the concentration boundary conditions are

$$\frac{\partial}{\partial r}(\phi S) = 0, \quad p_c + p_v = 1 + \mathscr{T}, \quad \text{and} \quad p_c = p_{c,\infty} \quad \text{at} \quad r = 1. \tag{2.47}$$

Additionally, because of the radial symmetry, it is appropriate to impose Neumann boundary conditions at the centre of the bean, namely,

$$\frac{\partial p_v}{\partial r} = \frac{\partial p_c}{\partial r} = \frac{\partial}{\partial r}(\phi S) = \frac{\partial T}{\partial r} = 0 \quad \text{at} \quad r = 0. \tag{2.48}$$

Finally, the initial conditions at $t = 0$ are

$$T = 0,\ p_v = p_{v,0},\ p_c = p_{c,0},\ S = \sigma,\ \phi = \phi_0\,. \tag{2.49}$$

We define the Local Moisture Model as the PDEs (2.38), (2.39), (2.40), (2.41), (2.42), the constitutive equations (2.43), (2.44), (2.45), the boundary conditions (2.46), (2.47), (2.48), and the initial conditions (2.49). Table 2.3 provides a description and a typical value of each dimensionless parameter shown above.

2.3.4 Simplification of the Local Moisture Model (the Mulitphase Model)

While the Local Moisture Model presented in Sections 2.3.3 appears to account for most of the processes relevant to the roasting of coffee beans, there are several difficulties in practice, primarily due to the lack of sufficient relevant physical data for determining realistic values of some parameter values. Furthermore, the complexity of the model makes interpretation of the behaviour of solutions somewhat complicated. In consequence, we are motivated to simplify the Local Moisture Model in order to to gain a preliminary understanding of the behaviour of its solutions.

Firstly, we note that several parameter values relating to CO_2 gas production are not well documented and that such parameters might only be determined by further experiments. We note however that, at least initially, we anticipate CO_2 production to be small and might therefore neglect its influence on the behaviour. This is equivalent to assuming the non-dimensional parameters $(\kappa_1, \kappa_2, \kappa_4, \mathscr{C}_3, H, \zeta_4)$ are all small. By doing so, this in turn implies that ϕ remains constant. We will revisit CO_2 production and variable porosity when extending models in Chapter 5.

In addition to the neglecting any CO_2 gas transport, we also simplify the transport of water and water vapour. If we assume that the dominant transport of water vapour is pressure-driven rather than by Fick's Law, we can conclude that the parameters $\mathscr{D}_1$ and $\mathscr{D}_2$ are small and can be neglected. Additionally, since k_{g0} is very small, due to the low permeability of the nano-porous coffee bean walls, we assume that $\frac{k_{w0}}{\mu_{w0}} \ll \frac{k_{g0}}{\mu_{g0}}$ (i.e. κ_3 is negligible).

Some parameter values in the Local Moisture Model have been determined, but

Dimensionless Parameter	Relationship to Dimensional Parameters	Typical value of Parameter
α_1	$\frac{\rho_s}{\rho_w}$	0.85
α_2	$\frac{p_0 m_v}{\rho_w R T_0}$	7.5×10^{-4}
B_1	$\frac{A_1}{p_0} \exp\left(A_2 - \frac{A_3}{T_0}\right)$	0.0235
B_2	$\frac{A_3}{T_0}$	17.5
γ	$\frac{\lambda_v}{T_0 C_{pw}}$	1.9
ζ_1	$\frac{K_s}{\rho_w C_{pw}} \cdot \frac{\rho_w}{L^2 I_{v0}}$	2.4×10^{-8}
ζ_2	$\frac{K_w}{\rho_w C_{pw}} \cdot \frac{\rho_w}{L^2 I_{v0}}$	3.9×10^{-7}
ζ_3	$\frac{K_v}{\rho_w C_{pw}} \cdot \frac{\rho_w}{L^2 I_{v0}}$	1.1×10^{-8}
ζ_4	$\frac{K_c}{\rho_w C_{pw}} \cdot \frac{\rho_w}{L^2 I_{v0}}$	1.0×10^{-8}
$\mathscr{C}_1$	$\frac{C_{ps}}{C_{pw}}$	0.11
$\mathscr{C}_2$	$\frac{C_{pv}}{C_{pw}}$	0.45
$\mathscr{D}_1$	$D_{\text{eff,g0}} \cdot \frac{\mu_{g0}}{k_{g0} p_0}$	-
$\mathscr{D}_2$	$D_{w0} \cdot \frac{\mu_{w0}}{k_{w0} p_0}$	-
$\mathscr{D}_3$	$\frac{k_{g0} p_0}{\mu_{g0}} \cdot \frac{\rho_w}{L^2 I_{v0}}$	$4.7{\times}10^{-9}$
$\mathscr{T}$	$\frac{T_\infty}{T_0} - 1$	0.61
Nu_v	$\frac{h_v L}{K_v}$	4
κ_1	$\frac{I_{c0}}{I_{v0}}$	1.56
κ_2	$\frac{m_v}{m_c}$	0.41
κ_3	$\frac{k_{w0} p_0}{\mu_{w0}} \cdot \frac{\mu_{g0}}{k_{g0} p_0}$	-
κ_4	$\frac{\lambda_c}{\lambda_v}$	-
$\mathscr{C}_3$	$\frac{C_{pc}}{C_{pw}}$	2.1×10^{-4}
H	$\frac{h_c}{h_v}$	-

Table 2.3: Description and typical values of dimensionless parameters used in the simplified form of the Local Moisture Model. Dimensional parameter values are given in Table 2.2.

are much smaller than other parameter values in the equation. Since $\alpha_2\mathscr{C}_2 \ll \alpha_1\mathscr{C}_1$ and $\alpha_2\mathscr{C}_2\mathscr{D}_3 \approx 10^{-12}$, we neglect both of these terms. Finally, we assume that k_g^* and μ_g^* are identically constant, implying that $\frac{k_g}{\mu_g} \equiv 1$, since k_{g0} and μ_{g0} have already been incorporated in the non-dimensionlisation.

Finally, since we anticipate evaporation to be a very quick process, we will pick a timescale and pressure scale that reflects an $O(1)$ vapour diffusion in non-dimensional quantities. Therefore, we rescale our variables such that

$$S = \sigma\hat{S}, \quad T = \hat{T}, \quad p_v = p_{ST}(1)\hat{P}, \quad t = \frac{\phi}{\mathscr{D}_3 p_{ST}(1)}\hat{t}\,. \tag{2.50}$$

Combining all of these simplifications and rescalings, our system of PDEs becomes (after dropping hats)

$$\frac{\partial S}{\partial t} = -\frac{1}{\epsilon^2}I_v, \tag{2.51}$$

$$\frac{\partial}{\partial t}\left[\frac{(1+\mathscr{T})P(1-\sigma S)}{1+\mathscr{T}T}\right] = -\frac{1}{\delta}\frac{\partial S}{\partial t} + \nabla\cdot\left[\frac{(1+\mathscr{T})P\nabla P}{1+\mathscr{T}T}\right], \tag{2.52}$$

$$\frac{\partial T}{\partial t} + \mathcal{A}_1\frac{\partial}{\partial t}\left[S(1+\mathscr{T}T)\right] = \mathcal{A}_2\frac{\partial S}{\partial t} + \mathcal{A}_3\nabla\cdot\left[(1+\mathcal{A}_4 S)\nabla T\right]. \tag{2.53}$$

Here, $\mathscr{T} = \frac{T_\infty}{T_0} - 1$ and relates the roasting temperature to room temperature, $\epsilon = \frac{\sqrt{\mathscr{D}_3\sqrt{1+\mathscr{T}}}}{\phi}$ and relates the evaporation timescale to the vapour diffusion timescale, and $\delta = \frac{p_{ST}(1)\alpha_2}{\sigma(1+\mathscr{T})}$ and relates the density of vapour to the density of water. Additionally, the rescaled evaporation rate I_v and the rescaled steam table pressure $P_{ST}(T)$ are given by

$$I_v = S(1-\sigma S)(P_{ST} - P)\sqrt{\frac{1+\mathscr{T}}{1+\mathscr{T}T}} \quad \text{and} \quad P_{ST}(T) = \exp\left(\frac{\beta(T-1)}{1+\mathscr{T}T}\right). \tag{2.54}$$

The boundary conditions we impose on the PDE system (2.51)-(2.53) are the symmetry conditions at the centre of the bean

$$\frac{\partial T}{\partial r} = 0, \quad \frac{\partial P}{\partial r} = 0 \ \text{ at } \ r = 0, \tag{2.55}$$

as well as the heat transfer condition

$$\frac{\partial T}{\partial r} = \nu\left(\frac{1-\sigma S}{1-\sigma}\right)\left(\frac{1+\mathcal{A}_4}{1+\mathcal{A}_4 S}\right)(1-T) \ \text{ at } \ r = 1. \tag{2.56}$$

If were to employ the boundary condition (2.47) without accounting for the non-

Multiphase Dimensionless Group	Relationship to Local Moisture Groupings	Typical value of Parameter
ϵ	$\frac{\sqrt{\mathscr{D}_3\sqrt{1+\mathscr{T}}}}{\phi}$	1.40×10^{-4}
δ	$\frac{p_{ST}(1)\alpha_2}{\sigma(1+\mathscr{T})}$	0.101
β	$\frac{B_2\mathscr{T}}{1+\mathscr{T}}$	6.66
$\mathcal{A}_1$	$\frac{\sigma\phi}{\alpha_1\mathscr{C}_1(1-\phi)\mathscr{T}}$	1.50
$\mathcal{A}_2$	$\gamma\mathcal{A}_1$	2.81
$\mathcal{A}_3$	$\frac{\phi(\zeta_1(1-\phi)+\zeta_3\phi)}{\mathscr{D}_3 p_{ST}(1)\alpha_1\mathscr{C}_1(1-\phi)}$	2.28
$\mathcal{A}_4$	$\frac{\phi\sigma(\zeta_2-\zeta_3)}{\zeta_1(1-\phi)+\zeta_3\phi}$	0.899
ν	$\frac{\mathrm{Nu}_v\zeta_3\phi(1-\sigma)}{(\zeta_1(1-\phi)+\zeta_3\phi)(1+\mathcal{A}_4)}$	0.585
P_a	$\frac{1+\mathscr{T}}{p_{ST}(1)}$	0.0879
T_a	$P_{ST}^{-1}(P_a)$	0.519

Table 2.4: Description and typical values of dimensionless parameters used in the Multiphase Model. Dimensionless groupings in the Local Moisture Model are given in Table 2.3.

reactive gases in the bean, we would observe condensation when the steam table pressure is smaller than this boundary condition, which occurs in the beginning of roasting. In order to prevent condensation from occurring at the surface of the bean, we impose that P equals the steam table pressure for temperatures below the evaporating temperature, i.e.

$$P\Big|_{r=1} = \begin{cases} P_{ST}(T), & T < T_a, \\ P_a, & T \geq T_a. \end{cases} \tag{2.57}$$

Finally, we impose the initial conditions corresponding to uniform initial moisture content, room temperature, and equilibrium steam table pressure, i.e.

$$S(r,0) = 1, \quad T(r,0) = 0, \quad P(r,0) = P_{ST}(0). \tag{2.58}$$

We define the Multiphase Model as the PDEs (2.51), (2.52), (2.53), the constitutive equation (2.54), the boundary conditions (2.55), (2.56), (2.57), and the initial conditions (2.58).

2.3.5 Numerical Results from the Multiphase Model

We focus on the Multiphase Model for preliminary results. We solve the nondimensionalised model presented in Section 2.3.4 using the method of lines with a finite difference scheme in the radial component, as outlined in (2.16), and a stiff ODE solver for the time stepping (i.e. the MATLAB function `ode15s`). This was implemented using MATLAB [35] with 301 spatial meshpoints, as a more refined spatial meshing would result in a prohibitive expense of computation time. Nevertheless, a convergence study similar to the one performed in the Bulk Moisture Model indicates that second-order convergence is achieved. Lastly, we assume parameters values given in Table 2.4.

In order to compare the experimental data and average moisture concentration presented in [13] with the predictions of the Multiphase Model, we need to briefly describe how the data relates to the moisture content variable in the Multiphase Model. We can define the moisture concentration c^* as the moisture content ($\frac{\phi S \rho_w}{(1-\phi)\rho_s}$, Section 2.3.1.5) multiplied by the molar density of water ($\frac{\rho_w}{m_w}$). This gives us

$$c^* = \frac{\phi S \rho_w^2}{(1-\phi)\rho_s m_w}. \tag{2.59}$$

This in turn tells us that a coffee bean with 12% moisture initially (5500 mol/m^3, as per [13]) would have $\sigma \approx 0.084$.

From the numerical results presented in Figure 2.5, we can see that S forms two distinct regions, each corresponding to when the evaporation rate

$$I_v = (P_{ST}(T) - P)S(1 - \sigma S)\sqrt{\frac{1 + \mathscr{T} T}{1 + T}} \tag{2.60}$$

must also be zero to leading order; a more detailed explanation of why this occurs will be discussed in Chapter 3. Nevertheless, we note that the evaporation rate I_v can equal zero in three ways: i) by having $P = P_{ST}(T)$, ii) by having $S = 0$, or iii) by having $S = \sigma^{-1}$. This naturally divides the solution into various subregions with one region for each of the cases. Physically, we can readily interpret the regions since i) is a region where the water vapour pressure is in equilibrium with the water, ii) is a region that is completely dry, and iii) corresponds to a completely water filled part of the bean. Between these regions, there will be narrow "transition layers", allowing the behaviour to smoothly vary. In practice, region iii) can only occur if some part the bean is initially full of water (i.e. $\sigma \equiv 1$) and we do not expect this to occur. Hence, in subsequent numerical results, we will see the development of the two regions: i) and ii).

Additionally, in Figure 2.6, we see that the Bulk Moisture Model and the Multiphase Model agree well with the temperature profiles shown at the core and the surface of the bean, when using parameters described in Table 2.3. Finally, we see in Figure 2.7 that the average moisture content predicted by the Multiphase Model has a very good agreement with the experimental data provided in [13], and affords a better fit than obtained from the Bulk Moisture Model.

2.4 Comparison of Solutions to the Two Models

At this point, it is natural to compare how the Bulk Moisture Model and the Multiphase Model compare and discuss their relative merits. Indeed, the results shown in Sections 2.2.3 and 2.3.5 indicate that both models can be fit to the experimental data shown in [13]. We note that, as indicated in Section 2.2.3, the Bulk Moisture Model can show numerical ill-posedness if the parameter values are not well-chosen. This behaviour does not seem to occur with the Multiphase Model. Regarding the internal transport of water, the Bulk Moisture Model uses a simple mass diffusivity term, while the Multiphase Model considers vapour and water as separate entities. In the former case, there is a need to ensure that the diffusivity is correctly fitted to data in the relevant temperature range, since it originates from models below the boiling point [23]. The latter suffers from a lack of physical data to properly quantify the many more parameters that are required. In particular, the Multiphase Model currently uses an ideal “steam table” pressure for the vapour pressure and this needs significant modification in the case of water bound to the solid phase. Such modifications to the steam table pressure are discussed in further detail in Chapter 4 and 5. One shortcoming of the specific mass diffusivity used in the Bulk Moisture Model is its dependence on the average moisture content. Such a dependency gives good fitting of the data, but the underlying physical mechanisms that it represents are not clear.

Although there is agreement on the predicted average moisture in a bean, there are substantial differences between the two models concerning the predicted distribution of the moisture the coffee bean. Specifically, the moisture content remaining after after a long period of time varies significantly between the two models. In the Bulk Moisture Model, the moisture in the bean slowly decreases after an initial transient period with spatial variance, causing the moisture throughout the bean to be nearly

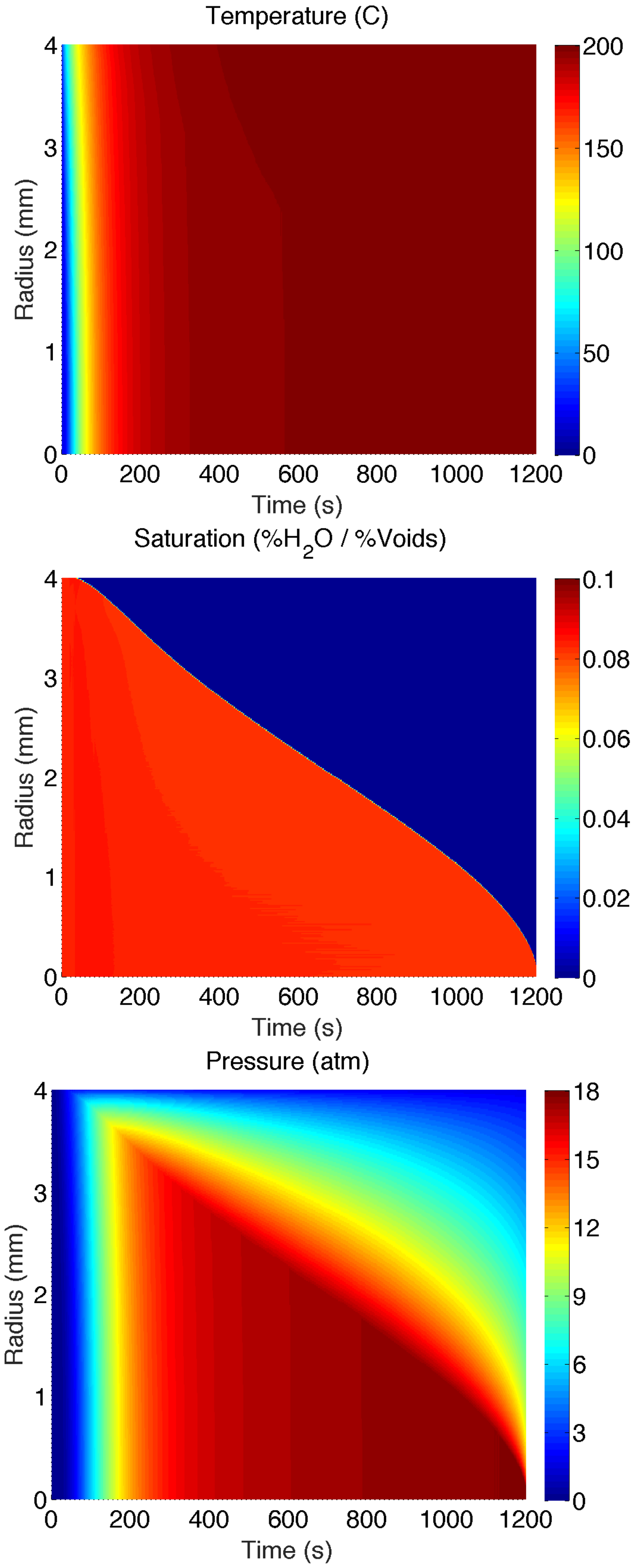

Figure 2.5: The solutions of the Multiphase Model, described in equations (2.51)-(2.58), for 1200s of roasting at 200°C. Dimensionless parameters are specified in Table 2.4 and boundary conditions described in Section 2.3.4 are imposed.

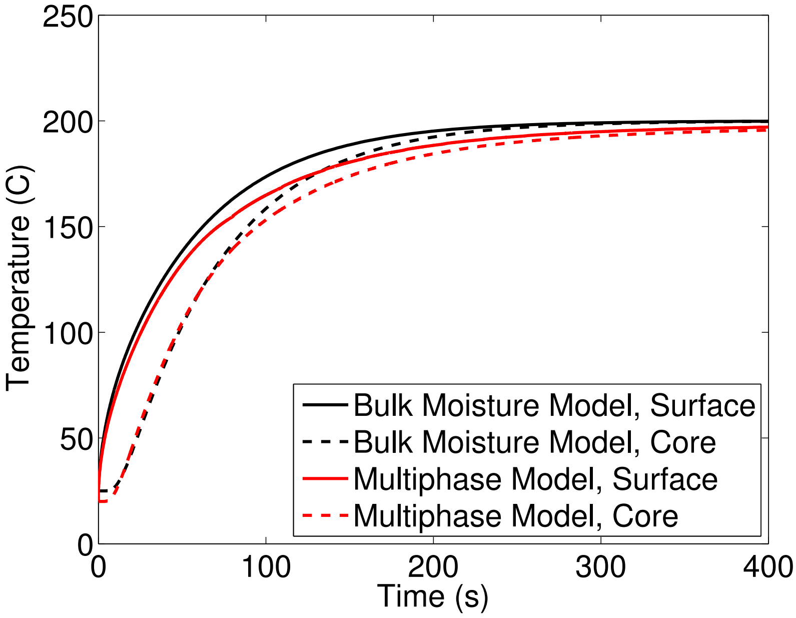

Figure 2.6: Comparison of temperature curves for a 4mm bean at the surface and the centre of the bean during 400s of roasting at 200°C under both the Bulk Moisture Model and the Multiphase Model. Parameter values for the Multiphase Model are listed in Table 2.4.

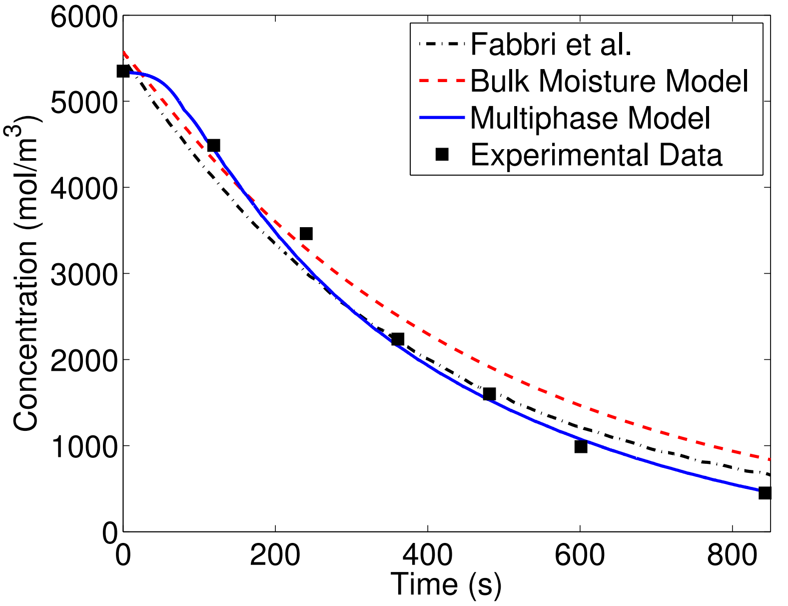

Figure 2.7: Comparison of average moisture content for a 4mm bean during 850s of roasting at 200°C for simulated and experimental data reproduced from Fabbri et al. [13], the Bulk Moisture Model, and the Multiphase Model. Parameter values used when obtaining solutions for the Bulk Moisture Model and the Multiphase Model are listed in Tables 2.1 and 2.4, respectively.

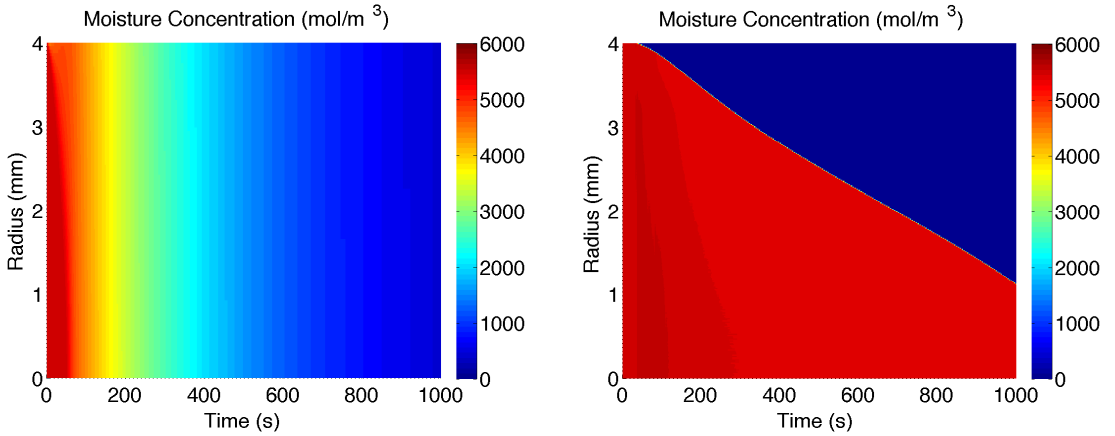

(a) (b)

Figure 2.8: Comparison of moisture concentrations in a 4mm bean during 1000s of roasting at 200°C for (a) the Bulk Moisture Model (2.10)-(2.15) and (b) the Multiphase Model (2.51)-(2.58). Parameter values for the Bulk Moisture Model and the Multiphase Model are listed in Tables 2.1 and 2.4 respectively.

uniform. On the other hand, in the Multiphase Model, the coffee bean is distinctly divided into a "moist" region (where $S \sim \sigma$) and a dry region ($S \sim 0$) via a "drying front". This drying front in the Multiphase Model is significantly sharper than in the Bulk Moisture Model, since the Bulk Moisture Model measures moisture in the bulk, and will show a bean drying in average moisture content, while the Multiphase Model will show the progress of the drying of a bean locally. Due to evaporation being a local phenomenon, we conclude that the Multiphase Model has a more realistic drying front. Such a comparison of these two models is shown in Figure 2.8. We note that these differences may play a significant role if used to predict where chemical reactions in the coffee bean can occur. In consequence, having a different localized model for the moisture concentration inside a coffee bean can significantly vary the predictions of other chemical reactions that can occur in a bean. These ideas will be further explored in Chapter 5.

One criticism of the Multiphase Model is that the gas permeability k_g, needed to match the experimental data, is approximately 2×10^{-19} m^{-2}. This is far smaller than the values $10^{-15} - 10^{-12}$ m^{-2} used for typical organic materials, such as wood (e.g. [8]). We will discuss how the Multiphase Model might be modified to make such fitted parameter values physically realistic in Chapter 5.

Until now, our main conclusion of the two models is that, while predicting different local moisture content within the bean, one can present similar average moisture content values to what is seen experimentally. We will now investigate how sensitive these parameters are to the lengthscale chosen using the following thought experiment. Suppose that we choose to finely grind up our green coffee beans and then roast them, rather than the standard method of grinding beans after roasting. Without changing any of the other parameters in the two models, how do the results differ? To answer this, we solve the Bulk Moisture Model and the Multiphase Model as before, but with changing $L = 0.2$mm to reflect a fine grinding of the bean. As we can see in Figure 2.9, the temperature profiles produced from the Bulk Moisture Model has at a significantly faster associated timescale than the Multiphase Model. Additionally, we also note that the moisture content predicted by these two models differ considerably. Indeed, the Bulk Moisture Model predicts a bean chunk that is nearly at roasting temperature, but still has a high moisture content. Conversely, the Multiphase Model predicts that after approximately 12s, the entire bean chunk has negligible moisture content. While experimental data on similar operating conditions are discussed more thoroughly in Chapter 5, we can still conclude from this thought experiment that the Bulk Moisture Model and the Multiphase Model will not always produce similar results in terms of average moisture content.

2.5 Discussion

We studied an existing model from the literature that describes the roasting of coffee beans and analysed it by looking at a very similar model, namely, the Bulk Moisture Model. With a suitable non-dimensionalisation, we were able to fit parameters occurring in this model to match the experimental data. While the parameters in the model could be adjusted to obtain a reasonable fit on the data, the model showed potential numerical problems when parameters were chosen slightly differently. Motivated by these numerical issues, along with certain ambiguity in the Bulk Moisture Model's physical processes, a new model (the Local Moisture Model) was derived from conservation equations. The Local Moisture Model accounts for different volume fractions for solid, liquid, and gas phases, the movement of water and gases, and the various materials observed in a coffee bean. By non-dimensionalising this system, as well as making certain simplifications to the model, we were also able to fit the experimental data obtained in [13] using the simplified form of the Local Moisture Model (the Multiphase Model). The main drawback of this model is the lack of physical data to properly fit the numerous parameters, since not all parameters have been previously determined experimentally. There were substantial differences between the models in the predicted distribution of moisture during the drying of the bean,

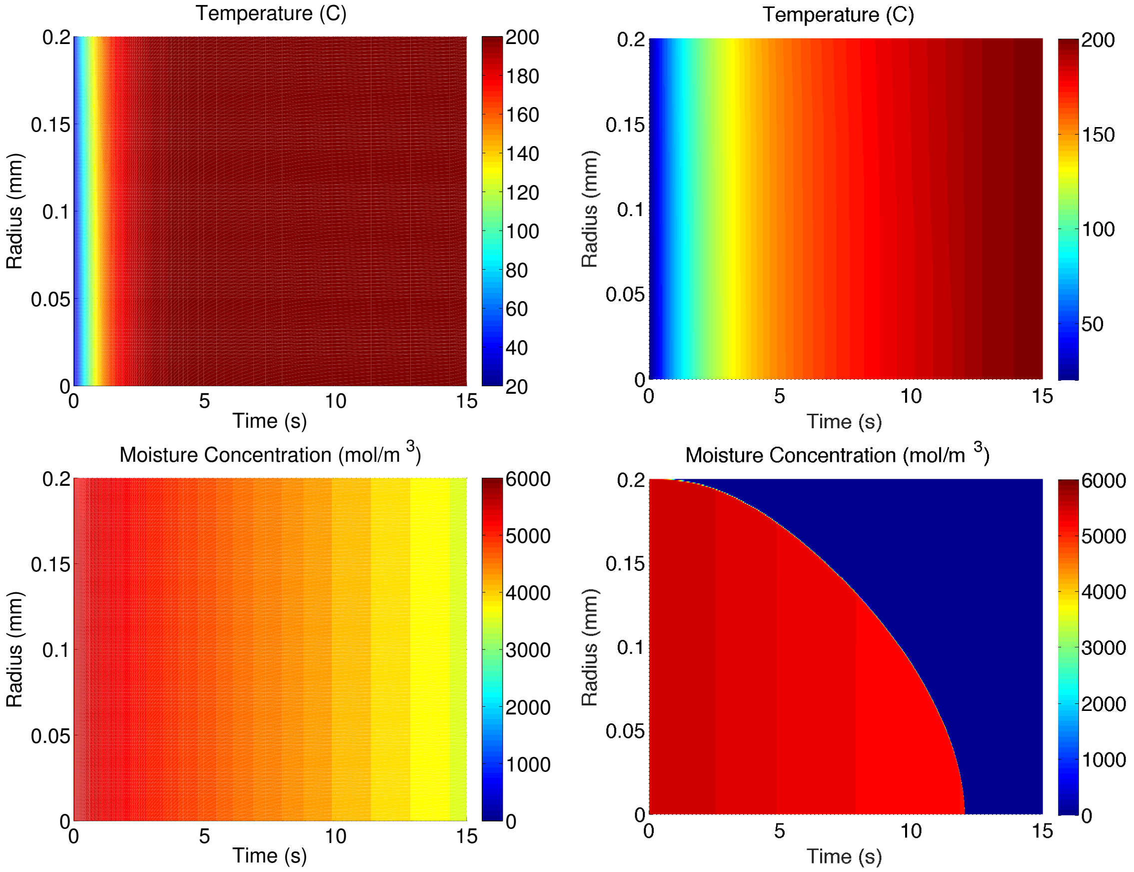

(a) (b)

Figure 2.9: Comparison of moisture concentrations in a 0.2mm bean chunk during 15s of roasting at 200°C for (a) the Bulk Moisture Model and (b) the Multiphase Model. Parameter values for the Bulk Moisture Model and the Multiphase Model (2.51)-(2.58) are listed in Tables 2.1 and 2.4, respectively.

which will be investigated further on. Compared to existing studies in the literature, the Multiphase Model allows for the influence of local moisture and heat transfer on the coffee bean roasting process to be better understood. Importantly, by including these local influences in our model, we were able to see the emergence of an explicit “drying front”, which was not previously seen in the literature when bulk quantities were employed. However, this Multiphase Model can prove useful to various roasting applications within the coffee industry, as well as for related roasting problems for which the roasting mechanism depends strongly on the existence of a drying front which penetrates from the surface to the core of a material. We will see, in Chapter 3, that we can determine an approximate form of this drying front via asymptotic analysis.

Chapter 3

Asymptotic Analysis of the Multiphase Model

3.1 Introduction

This chapter is mainly comprised of results shown in [16], where we are motivated to extend the results of the Multiphase Model, derived in Chapter 2, via asymptotic methods. As we observed in Chapter 2, in the early stages of coffee bean roasting, there are two emergent regions: a dried outer region and a saturated interior region. The two regions are separated by a transition layer (or, drying front). By obtaining asymptotic expansions for these quantities in relevant limits of the physical parameters, we are able to determine the qualitative behaviour of the outer and interior regions, as well as the dynamics of the drying front. Although a number of simplifications and scalings are used, we take care not to discard aspects of the model which are fundamental to the roasting process. Indeed, we find that for all of the asymptotic limits considered, our approximate solutions faithfully reproduce the qualitative features evident from numerical simulations of the full model. From these asymptotic results, we have a better qualitative understanding of the drying front (which is hard to resolve precisely in numerical simulations), and hence, of the various mechanisms at play including heating, evaporation, and pressure changes. This qualitative understanding of solutions to the multiphase model is essential when creating more involved models that incorporate chemical reactions and solid mechanics effects.

3.2 Asymptotics of the Multiphase Model with Variable Temperature

The (nondimensional) Multiphase Model (2.51)-(2.58) in Chapter 2 is

$$\frac{\partial S}{\partial t} = -\frac{1}{\epsilon^2} I_v, \tag{3.1}$$

$$\frac{\partial}{\partial t}\left[\frac{(1+\mathscr{T})P(1-\sigma S)}{1+\mathscr{T}T}\right] = -\frac{1}{\delta}\frac{\partial S}{\partial t} + \nabla\cdot\left[\frac{(1+\mathscr{T})P\nabla P}{1+\mathscr{T}T}\right], \tag{3.2}$$

$$\frac{\partial T}{\partial t} + \mathcal{A}_1\frac{\partial}{\partial t}\left[S(1+\mathscr{T}T)\right] = \mathcal{A}_2\frac{\partial S}{\partial t} + \mathcal{A}_3\nabla\cdot\left[(1+\mathcal{A}_4 S)\nabla T\right]. \tag{3.3}$$

Here, $\mathscr{T} = \frac{T_\infty}{T_0} - 1$ and relates the roasting temperature to room temperature, $\epsilon = \frac{\sqrt{\mathscr{D}_3\sqrt{1+\mathscr{T}}}}{\phi}$ and relates the evaporation timescale to the vapour diffusion timescale, and $\delta = \frac{p_{ST}(1)\alpha_2}{\sigma(1+\mathscr{T})}$ and relates the density of vapour to the density of water. Additionally, the rescaled evaporation rate I_v and the rescaled steam table pressure $P_{ST}(T)$ are given by

$$I_v = S(1-\sigma S)(P_{ST}-P)\sqrt{\frac{1+\mathscr{T}}{1+\mathscr{T}T}} \quad \text{and} \quad P_{ST}(T) = \exp\left(\frac{\beta(T-1)}{1+\mathscr{T}T}\right). \tag{3.4}$$

The boundary conditions we impose on the PDE system (3.1)-(3.3) are the heat transfer condition

$$\nabla T\cdot\mathbf{n} = \nu\left(\frac{1-\sigma S}{1-\sigma}\right)\left(\frac{1+\mathcal{A}_4}{1+\mathcal{A}_4 S}\right)(1-T) \quad \text{at} \quad r=1 \tag{3.5}$$

and a Dirichlet condition in P at the surface of the bean:

$$P\Big|_{r=1} = \begin{cases} P_{ST}(T), & T < T_a, \\ P_a, & T \geq T_a. \end{cases} \tag{3.6}$$

We will also make the assumption that the switching between the boundary condition for P only occurs at one critical time, namely, t^*. We define t^* as the time when the surface temperature equals the evaporation temperature T_a, i.e. as the solution to the equation

$$T(1,t^*) = T_a := P_{ST}^{-1}\left(P_a\right). \tag{3.7}$$

This critical time will be used not only to signal which part of the step in (3.6) is relevant, but also to signal where the asymptotic behaviour changes. Finally, we impose the initial conditions corresponding to uniform initial moisture content, room temperature, and equilibrium steam table pressure, i.e.

$$S(r,0)=1, \quad T(r,0)=0, \quad P(r,0)=P_{ST}(0). \tag{3.8}$$

A key feature of this model is the non-dimensional parameter ϵ, which can be interpreted as a ratio in timescales between Darcy-driven vapour transport and evaporation. One can interpret the non-dimensional parameters δ as a density ratio of water vapour to water, σ represents the initial water-to-void volume ratio, and P_a is the ambient vapour pressure in the roasting chamber.

For the physically relevent range of non-dimensional parameter values, we can divide the solution to the model into three regions in order to understand the approximate dynamics that occur in the coffee bean. Using parameter values shown in Chapter 2, a typical value of $\epsilon \approx 1.54 \times 10^{-4}$ suggests that we should consider the limit of $\epsilon \to 0^+$. We note that $\delta = O(1)$ is the distinguished limit of this system and concentrate on considering this case, despite the analysis being also valid for small δ. We will consider δ being small when the equations require further simplifications to extract closed form solutions. In Section 3.2.2, we will determine how small δ is allowed to be before a different analysis is required. In the $\epsilon \to 0^+$ limit, we can see from (3.1) that if time and space remain unscaled, $I_v = 0$ will be the leading-order equation, and from (3.4), this can occur in one of three ways. Firstly, $I_v = 0$ if the vapour pressure is in equilibrium with its steam table pressure, i.e. $P = P_{ST}$. As the initial data are consistent with this equilibrium, we will observe this first (which will be referred to as Region i). Secondly, $I_v = 0$ can be achieved by setting $S = 0$. This corresponds to where there is no more water to evaporate and will be denoted as Region ii. A final case where $I_v = 0$ is when $S = \sigma^{-1}$; however, this corresponds to when the coffee bean is completely saturated with water, which we will discard as an extraneous case.

We will also consider a narrow “drying front” that connects Regions i and ii. This drying front, which is centred about $r = R(t)$, propagates from the surface of the bean towards the center of the bean and is where the moisture content S quickly goes from 1 to 0. In this drying front around $R(t)$, we find that the temperature is approximately spatially uniform, but will vary as time progresses. This temperature profile within the drying front is denoted as $T^*(t)$. A schematic diagram of the three regions is shown in Figure 3.1, including the time t^* at which evaporation first occurs at the surface of the bean.

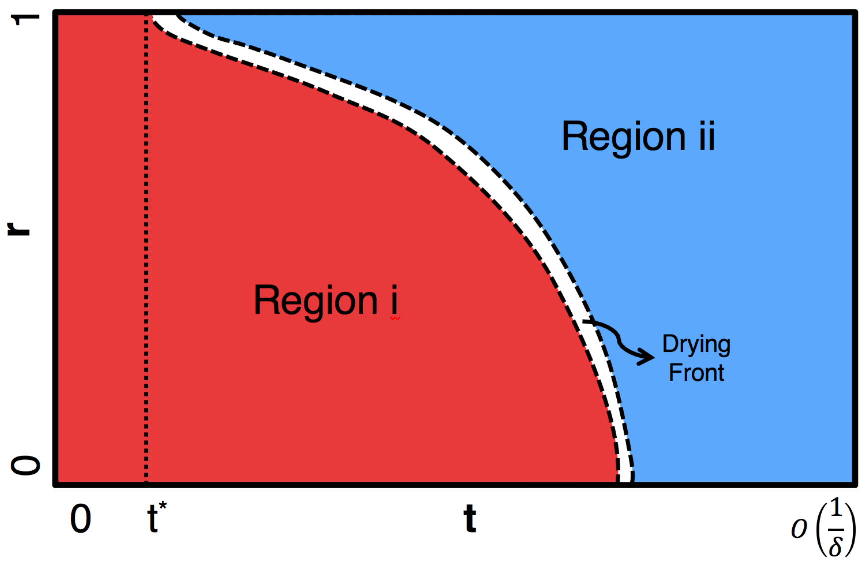

Figure 3.1: A summary of where the different regions are as the bean dries. Region i is when the vapour pressure is in equilibrium, Region ii is the dry region, and the dashed lines indicate the narrow transition layer between the regions, which begins at time t^*, defined in (3.7).

3.2.1 Asymptotics of Region i

In Region i, we have, from (3.1), $I_v = 0$ to leading order in the limit of $\epsilon \to 0^+$, implying that that $P = P_{ST}(T)$. Consider the asymptotic series valid as $\epsilon \to 0^+$,

$$\begin{aligned} S &= S_0(r,t) + \epsilon S_1(r,t) + O(\epsilon^2), \\ T &= T_0(r,t) + \epsilon T_1(r,t) + O(\epsilon^2), \\ P &= P_{ST}(r,t) + \epsilon P_1(r,t) + O(\epsilon^2). \end{aligned} \tag{3.9}$$

Substituting (3.9) into (3.2) and (3.3) gives, to lowest order,

$$\frac{1}{\delta}\frac{\partial S_0}{\partial t} + \frac{\partial}{\partial t}\left[(1-\sigma S_0)P_{ST}(T_0)\Lambda(T_0)\right] = \nabla \cdot \left[P_{ST}(T_0)\Lambda(T_0)\nabla P_{ST}(T_0)\right], \tag{3.10}$$

$$\frac{\partial S_0}{\partial t}[\mathcal{A}_1(1+\mathscr{T}T_0) - \mathcal{A}_2] + \frac{\partial T_0}{\partial t}\left[1 + \mathcal{A}_1\mathscr{T}S_0\right] = \mathcal{A}_3\nabla \cdot \left[(1+\mathcal{A}_4 S_0)\nabla T_0\right], \tag{3.11}$$

where

$$\Lambda(T_0) = \frac{1}{1+\mathscr{T}T_0}. \tag{3.12}$$

As we cannot solve this system analytically, we now suppose that $\delta \ll 1$ and write an asymptotic series in powers of δ for S_0 and T_0 valid in the limit $\delta \to 0^+$ as

$$S_0 = \tilde{S}_0(r,t) + \delta \tilde{S}_1(r,t) + O(\delta^2), \quad T_0 = \tilde{T}_0(r,t) + \delta \tilde{T}_1(r,t) + O(\delta^2). \tag{3.13}$$

Substituting (3.13) into (3.10) gives us, to leading order, that $\frac{\partial \tilde{S}_0}{\partial t} = 0$. Therefore, the moisture content of the bean stays at its initial value, i.e. $\tilde{S}_0 = 1$. To lowest order, (3.11) then gives us

$$\frac{\partial \tilde{T}_0}{\partial t} = \mathcal{K} \nabla^2 \tilde{T}_0, \quad \text{where} \quad \mathcal{K} = \frac{\mathcal{A}_3(1+\mathcal{A}_4)}{1+\mathcal{A}_1 \mathscr{T}}. \tag{3.14}$$

Equation (3.14) must be solved subject to the boundary condition (3.6), which can be stated as

$$\nabla \tilde{T}_0 \cdot \mathbf{n}\Big|_{r=1} = \nu \left(1 - \tilde{T}_0\big|_{r=1}\right), \quad t < t^*, \tag{3.15}$$

$$\tilde{T}_0\big|_{r=R(t)} = T^*(t), \quad t \geq t^*. \tag{3.16}$$

Additionally, we will impose the symmetry condition $\nabla \tilde{T}_0 \cdot \mathbf{n} = 0$ at $r = 0$, as well as the initial data $\tilde{T}_0(r,0) = 0$. We are able to solve the PDE for $t < t^*$, and hence, a leading-order approximation for t^*. By solving (3.14) in spherical coordinates, we obtain that

$$\tilde{T}_0(r,t) = 1 - \sum_{n=1}^{\infty} \frac{c_n}{r} \sin(\mu_n r) \exp(-\mu_n^2 \mathcal{K} t). \tag{3.17}$$

where the eigenvalues μ_n satisfy the transcendental equation $\mu_n \cot(\mu_n) = 1 - \nu$ and the constants c_n have the form

$$c_n = \begin{cases} \dfrac{2\nu \cos \mu_n}{\mu_n(\sin^2 \mu_n - \nu)}, & \nu \neq 1, \\ \\ \dfrac{8(-1)^n}{\pi^2(1+2n)^2}, & \nu = 1. \end{cases} \tag{3.18}$$

While the case $\nu = 1$ is reasonably pathological, it is included in this analysis for completeness. Typical parameter values seen in Chapter 2 give $\nu \approx 0.585$, so we will only consider the case where $\nu \neq 1$ from here on.

To determine t^* in spherical coordinates, denoted as t^*_{Sph}, we impose, from (3.7), that $\tilde{T}_0(1, t^*_{\text{Sph}}) = T_a$. When $\nu \neq 1$, this is equivalent to writing

$$\sum_{n=1}^{\infty} \left(\frac{\cos^2 \mu_n}{\sin^2 \mu_n - \nu} \right) \exp(-\mu_n^2 \mathcal{K} t^*_{\text{Sph}}) = \frac{(1 - T_a)\,(1 - \nu)}{2\nu}. \tag{3.19}$$

Using the parameter values in Chapter 2 ($\mathcal{K} \approx 2.25, \nu \approx 0.585, T_a \approx 0.519$), (3.19) has the solution $t^*_{\text{Sph}} \approx 0.173$, or about 45.9 seconds in dimensional units.

Similarly, we can determine t^* in Cartesian coordinates, denoted as t^*_{Cart}, by noting that the solution of (3.14) in Cartesian coordinates, with a Neumann boundary condition at $r = 0$, is

$$\tilde{T}_0(r, t) = 1 - \sum_{n=1}^{\infty} d_n \cos(\lambda_n r) \exp(-\lambda_n^2 \mathcal{K} t), \tag{3.20}$$

where

$$\lambda_n \tan \lambda_n = \nu \quad \text{and} \quad d_n = \frac{2\nu \sin \lambda_n}{\lambda_n(\nu + \sin^2 \lambda_n)}. \tag{3.21}$$

This allows us to determine t^*_{Cart} via the transcendental equation

$$\sum_{n=1}^{\infty} \frac{\sin^2 \lambda_n}{\nu + \sin^2 \lambda_n} \exp(-\lambda_n^2 \mathcal{K} t^*_{\text{Cart}}) = \frac{1 - T_a}{2}, \tag{3.22}$$

which, using parameter values stated above, gives $t^*_{\text{Cart}} \approx 0.494$, or about 131 seconds in dimensional units. Hence, we have determined when the step occurs in the boundary condition (3.6). When the boundary condition changes, we find that the transition layer forms at the surface. We shall not consider the very small time while the transition layer is close to the surface, as it does not give any useful insight, but proceed to when it is in the interior of the bean.

3.2.2 Asymptotics of the Transition Layer

In order to understand how S varies from 1 to 0, we must examine the transition layer in the limit $\epsilon \to 0^+$. We first discuss the distinguished limit $\delta = O(1)$. We will find that both P and T are spatially uniform at lowest order with small variations of equal size (say $O(\epsilon^a)$, $a > 0$) and hence, variations of the evaporation rate are also $O(\epsilon^a)$. The transition layer is narrow (say $O(\epsilon^b)$, $b > 0$) around a moving front at $r = R(t)$ and we find, noting that $S = O(1)$, that a balance between the resulting advective term in (3.1) and the evaporation rate requires $-b = -2 + a$. Similarly, having a balance of vapour production due to evaporation with transport by Darcy flow in (3.2) requires that $-b = -2b + a$. Hence, in the distinguished limit $\delta = O(1)$, we take $a = b = 1$. We can also consider small δ; when $\delta = O(\epsilon^{\alpha})$ and $\alpha > 0$, a dominant balance requires that $-b = a - 2$ and $-\alpha - b = -2b + a$. Therefore, the transition layer has width $O(\epsilon^{1+\alpha/2})$ and the variations in P and T are $O(\epsilon^{1-\alpha/2})$. Since we require these variations to be small, we must have $\alpha < 2$. We conclude that the analysis in the distinguished limit $\delta = O(1)$ is valid until $\delta = O(\epsilon^2)$.

For the case $\delta = O(1)$, the transition layer is around "drying front" $R(t)$ and we introduce the scaling $r = R(t) + \epsilon\hat{r}$. We also take P, T, and S as asymptotic series as $\epsilon \to 0^+$, with

$$\begin{aligned} S &= S_0(\hat{r}, t) + \epsilon S_1(\hat{r}, t) + O(\epsilon^2), \\ P &= P_0(\hat{r}, t) + \epsilon P_1(\hat{r}, t) + O(\epsilon^2), \\ T &= T_0(\hat{r}, t) + \epsilon T_1(\hat{r}, t) + O(\epsilon^2). \end{aligned} \tag{3.23}$$

We will first show that $T_0(\hat{r}, t) \equiv T^*(t)$ and $P_0(\hat{r}, t) \equiv P^*(t) := P_{ST}(T^*(t))$. To do this, we note that, in order to match our transition layer into Region i, we must have that

$$P_0\big|_{\hat{r}\to-\infty} \to P^*(t) \quad \text{and} \quad T_0\big|_{\hat{r}\to-\infty} \to T^*(t). \tag{3.24}$$

By substituting (3.23) into (3.2) and (3.3), we obtain, at $O\left(\epsilon^{-2}\right)$,

$$\frac{\partial}{\partial\hat{r}}\left[\frac{P_0\frac{\partial P_0}{\partial\hat{r}}}{1 + \mathscr{T} T_0}\right] = 0, \qquad \frac{\partial}{\partial\hat{r}}\left[\frac{\partial T_0}{\partial\hat{r}}(1 + \mathcal{A}_4 S_0)\right] = 0. \tag{3.25}$$

We note that these equations hold in any geometry at leading order, provided that we are sufficiently far away from any geometry-induced singularities that could produce additional derivative terms at $O\left(\epsilon^{-2}\right)$, e.g. if $R(t) = O(\epsilon)$ in spherical coordinates. Integrating (3.25) and imposing (3.24) implies that

$$T_0(\hat{r}, t) \equiv T^*(t) \quad \text{and} \quad P_0(\hat{r}, t) \equiv P^*(t). \tag{3.26}$$

To determine the leading-order behaviour for S, we note that using (3.23) in (3.4) and expanding yields

$$\begin{aligned} P_{ST} &= P^*\left(1 + \epsilon\frac{\beta(1 + \mathscr{T})}{(1 + \mathscr{T} T^*)^2}T_1\right) + O\left(\epsilon^2\right), \\ I_v &= -\epsilon\left(P_1 - \frac{\beta(1 + \mathscr{T})}{(1 + \mathscr{T} T^*)^2}T_1 P^*\right) S_0(1 - \sigma S_0)\sqrt{\frac{1 + \mathscr{T}}{1 + \mathscr{T} T^*}} + O\left(\epsilon^2\right). \end{aligned} \tag{3.27}$$

Using (3.27) along with (3.24), we find, at $O(\epsilon^{-1})$, that (3.1)-(3.3) give

$$-R'(t)\frac{\partial S_0}{\partial \hat{r}} = \Psi(P_1, T_1)S_0(1-\sigma S_0), \tag{3.28}$$

$$\sigma P^* R'(t)\frac{\partial S_0}{\partial \hat{r}} = -\frac{1}{\delta}\Psi(P_1,T_1)S_0(1-\sigma S_0)\left(\frac{1+\mathscr{T}T^*}{1+\mathscr{T}}\right) + P^*\frac{\partial^2 P_1}{\partial \hat{r}^2}, \tag{3.29}$$

$$-\mathcal{A}_1(1+\mathscr{T}T^*)R'(t)\frac{\partial S_0}{\partial \hat{r}} = \mathcal{A}_2\Psi(P_1,T_1)S_0(1-\sigma S_0) + \mathcal{A}_3\frac{\partial}{\partial \hat{r}}\left[(1+\mathcal{A}_4 S_0)\frac{\partial T_1}{\partial \hat{r}}\right], \tag{3.30}$$

where

$$\Psi(P_1,T_1) := \sqrt{\frac{1+\mathscr{T}}{1+\mathscr{T}T^*}}\left(P_1 - \frac{\beta(1+\mathscr{T})}{(1+\mathscr{T}T^*)^2}T_1 P^*\right). \tag{3.31}$$

Finally, the matching conditions with Regions i and ii are

$$S_0 \to 1, \quad P_1 \to 0, \quad \text{and} \quad T_1 \to 0 \quad \text{as} \quad \hat{r} \to -\infty, \tag{3.32}$$

$$S_0 \to 0 \quad \text{as} \quad \hat{r} \to +\infty, \tag{3.33}$$

$$\left.\frac{\partial P_1}{\partial \hat{r}}\right|_{\hat{r}\to+\infty} = \left.\frac{\partial P}{\partial r}\right|_{r\to R(t)}, \tag{3.34}$$

$$\left.\frac{\partial T_1}{\partial \hat{r}}\right|_{\hat{r}\to+\infty} = \left.\frac{\partial T}{\partial r}\right|_{r\to R(t)}. \tag{3.35}$$

In interpreting (3.32)-(3.35), we note that the limits where $r \to R(t)$ are matching conditions for solutions in Regions i and ii, whereas the limits where $\hat{r} \to \pm\infty$ refer to matching conditions for solutions in the transition layer.

By eliminating the terms with $\Psi(P_1, T_1)$ in (3.28) and (3.29), we obtain

$$P^*\frac{\partial^2 P_1}{\partial \hat{r}^2} = \left[\sigma P^* - \frac{1}{\delta}\left(\frac{1+\mathscr{T}T^*}{1+\mathscr{T}}\right)\right]R'(t)\frac{\partial S_0}{\partial \hat{r}}. \tag{3.36}$$

Integrating this and imposing the matching conditions (3.32) yields

$$\frac{\partial P_1}{\partial \hat{r}} = \left[\frac{1}{\delta}\left(\frac{1+\mathscr{T}T^*}{(1+\mathscr{T})P^*}\right) - \sigma\right]R'(t)(1-S_0). \tag{3.37}$$

Similarly, eliminating terms with $\Psi(P_1, T_1)$ in (3.28) and (3.30) gives us

$$R'(t)\left[\mathcal{A}_2 - \mathcal{A}_1(1+\mathscr{T}T^*)\right]\frac{\partial S_0}{\partial \hat{r}} = \mathcal{A}_3\frac{\partial}{\partial \hat{r}}\left[(1+\mathcal{A}_4 S_0)\frac{\partial T_1}{\partial \hat{r}}\right]. \tag{3.38}$$

Integrating and imposing the matching conditions (3.32) yields, after some rearranging,

$$\frac{\partial T_1}{\partial \hat{r}} = -\frac{1}{\mathcal{A}_3} R'(t) \left[\mathcal{A}_2 - \mathcal{A}_1(1 + \mathscr{T} T^*)\right] \left(\frac{1 - S_0}{1 + \mathcal{A}_4 S_0}\right). \tag{3.39}$$

Finally, by rearranging (3.28) to isolate S_0, we obtain

$$\frac{\frac{\partial S_0}{\partial \hat{r}}}{S_0(1 - \sigma S_0)} = -\frac{\Psi(P_1, T_1)}{R'(t)}. \tag{3.40}$$

In order to write a single differential equation for S_0, we differentiate (3.40) with respect to $\hat{r}$, as well as substitute in (3.37) and (3.39), to give us

$$\frac{\partial^2 S_0}{\partial \hat{r}^2} - \left(\frac{\partial S_0}{\partial \hat{r}}\right)^2 \frac{1 - 2\sigma S_0}{S_0(1 - \sigma S_0)} + S_0(1 - \sigma S_0)(1 - S_0)\Upsilon(S_0) = 0, \tag{3.41}$$

where we define

$$\Upsilon(S_0) := \sqrt{\frac{1 + \mathscr{T}}{1 + \mathscr{T} T^*}} \left[\frac{1}{\delta}\left(\frac{1 + \mathscr{T} T^*}{(1 + \mathscr{T})P^*}\right) - \sigma - \left(\frac{\beta(1 + \mathscr{T})P^*}{\mathcal{A}_3(1 + \mathscr{T} T^*)^2}\right)\left(\frac{\mathcal{A}_2 - \mathcal{A}_1(1 + \mathscr{T} T^*)}{1 + \mathcal{A}_4 S_0}\right)\right]. \tag{3.42}$$

We note that, aside from the denominator $1 + \mathcal{A}_4 S_0$, the components of the function $\Upsilon(S_0)$ are independent of $\hat{r}$. By identifying equation (3.41) as a Bernoulli-like ODE, we can use integrating factors and the matching conditions (3.33) to obtain the first-order non-linear autonomous differential equation for $S_0(\hat{r})$:

$$\frac{\partial S_0}{\partial \hat{r}} = -S_0(1 - \sigma S_0)\sqrt{2\int_{S_0}^{1} \frac{(1 - \chi)\Upsilon(\chi)}{\chi(1 - \sigma\chi)} \mathrm{d}\chi}\,. \tag{3.43}$$

It immediately follows that S_0 is monotone decreasing when S_0 lies between 0 and 1. Hence, we conclude that P and T do not drastically change within the transition layer and the $O(\epsilon)$ perturbations P_1 and T_1 can be related to S_0, which is the solution of a first-order differential equation in $\hat{r}$.

3.2.3 Asymptotics of Region ii

While the leading-order dynamics of S, T, and P have been determined in the transition layer, we still do not have an explicit form for $R(t)$ and $T^*(t)$. To find these, we now examine Region ii, where negligible water is present. From (3.1), we have that $S = 0$ at $O(\epsilon^{-2})$. However, this in turn causes a cascading effect in the asymptotic expansion of (3.1), and we conclude that $S = o(\epsilon^n)$ for all natural numbers n. Motivated by this fact, we anticipate that S will be exponentially small in Region ii.

Indeed, we can solve (3.1) explicitly, coupled with the condition that $S = 1$ at $t = t^*$:

$$S = \left\{ (1-\sigma) \exp \left[\frac{1}{\epsilon^2} \int_{t^*}^{t} \left(P_{ST}(T(r,s)) - P(r,s)\right) \sqrt{\frac{1+\mathscr{T}}{1+\mathscr{T}T(r,s)}}\, \mathrm{d}s \right] + \sigma \right\}^{-1}. \tag{3.44}$$

As we anticipate P to deviate from $P_{ST}(T)$ significantly in Region ii for $t > t^*$, it follows that S is indeed exponentially small. If we then neglect exponentially small terms, (3.2) and (3.3) become

$$\frac{\partial}{\partial t}\left[\frac{P}{1+\mathscr{T}T}\right] = \nabla \cdot \left[\frac{P\nabla P}{1+\mathscr{T}T}\right], \tag{3.45}$$

$$\frac{\partial T}{\partial t} = \mathcal{A}_3 \nabla^2 T. \tag{3.46}$$

For our boundary conditions in Region ii, we have the matching conditions (3.33)-(3.35), implying

$$T\Big|_{r\to R(t)} \to T^*(t), \quad P\Big|_{r\to R(t)} \to P^*(t), \tag{3.47}$$

$$\frac{\partial P}{\partial r}\Big|_{r\to R(t)} = \frac{\partial P_1}{\partial \hat{r}}\Big|_{\hat{r}\to+\infty} \to \left[\frac{1}{\delta}\left(\frac{1+\mathscr{T}T^*}{(1+\mathscr{T})P^*}\right) - \sigma\right] R'(t), \tag{3.48}$$

$$\frac{\partial T}{\partial r}\Big|_{r\to R(t)} = \frac{\partial T_1}{\partial \hat{r}}\Big|_{\hat{r}\to+\infty} \to -\frac{1}{\mathcal{A}_3}\left[\mathcal{A}_2 - \mathcal{A}_1(1+\mathscr{T}T^*)\right] R'(t). \tag{3.49}$$

We must also give an initial condition for $R(t)$ and $T^*(t)$. As the drying front starts from the surface of the bean and the temperature is at the switching point of (3.6), the initial conditions are $R(t^*) = 1$, $T^*(t^*) = T_a$. Finally, our solutions must also continue to agree with the outer surface boundary conditions of the system, namely,

$$\frac{\partial T}{\partial r}\Big|_{r=1} = \nu\left(\frac{1+\mathcal{A}_4}{1-\sigma}\right)\left[1 - T\big|_{r=1}\right] \quad \text{and} \quad P\Big|_{r=1} = P_a. \tag{3.50}$$

Therefore, our leading-order problem for T and P in Region ii is a coupled system of two Stefan-like problems in a mass transfer setting, rather than the classical heat transfer setting [37]. As this coupled system of PDEs (3.45)-(3.50) is not explicitly solvable, we are motivated to use the large Stefan number approximation by considering the limiting case when $\delta \ll 1$. The large Stefan number approximation has been studied previously in the context of heat transfer on spheres (see e.g. [36]). For Region ii, the large Stefan limit $\delta \ll 1$ corresponds to the drying front moving very slowly relative to the speed of vapour diffusion.

By rescaling time with $\tau = \delta(t - t^*)$, we can examine the asymptotic series

$$T = T_0(r,\tau) + \delta T_1(r,\tau) + O(\delta^2), \quad P = P_0(r,\tau) + \delta P_1(r,\tau) + O(\delta^2) \tag{3.51}$$

as $\delta \to 0^+$. In consequence, our leading-order Region ii problem (3.45)-(3.50) becomes

$$\nabla^2 T_0 = 0, \qquad T_0\big|_{r\to R(\tau)} \to T^*(\tau), \tag{3.52}$$

$$\nabla \cdot \left(\frac{P_0 \nabla P_0}{1 + \mathscr{T} T_0} \right) = 0, \qquad P_0\big|_{r\to R(\tau)} \to P^*(\tau), \tag{3.53}$$

$$\frac{\partial T_0}{\partial r}\bigg|_{r\to R(\tau)} \to 0, \qquad \frac{\partial P_0}{\partial r}\bigg|_{r\to R(\tau)} \to \left(\frac{1 + \mathscr{T} T^*}{(1+\mathscr{T})P^*} \right) R'(\tau), \tag{3.54}$$

$$\frac{\partial T_0}{\partial r}\bigg|_{r=1} = \nu \left(\frac{1 + \mathcal{A}_4}{1 - \sigma} \right) \left[1 - T_0\big|_{r=1} \right], \qquad P_0\big|_{r=1} = P_a, \tag{3.55}$$

$$R(0) = 1, \qquad T^*(0) = T_a. \tag{3.56}$$

Solving (3.52) implies that $T_0 \equiv T^*(\tau)$ and applying (3.55) forces $T^*(\tau) \equiv 1$. In consequence, this reduces our coupled Stefan problem to a Stefan problem for pressure alone, i.e.

$$\nabla \cdot (P_0 \nabla P_0) = 0, \qquad P_0\big|_{r\to R(\tau)} \to 1, \qquad P_0\big|_{r=1} = P_a, \tag{3.57}$$

$$\frac{\partial P_0}{\partial r}\bigg|_{r\to R(\tau)} \to R'(\tau), \tag{3.58}$$

$$R(0) = 1. \tag{3.59}$$

We note that this solution cannot satisfy the initial condition (3.56) for $T^*(t)$. For this to be resolved, we would have to consider the full problem in t, (3.45)-(3.50), which is not readily solvable.

3.2.3.1 Determining $R(t)$ in Cartesian Coordinates with $T^* \equiv 1$

In the limiting case where $\delta \ll 1$, i.e. $T^* \equiv 1$, we can solve (3.57), provided that we neglect any short-time discrepancies between the initial condition $T^*(0) = T_a$ and $T^* \equiv 1$. Solving this PDE system (3.57) gives us

$$P_0(r,\tau) = \sqrt{1 - (1 - P_a^2)\left(\frac{r - R(\tau)}{1 - R(\tau)} \right)}, \tag{3.60}$$

while the Stefan condition (3.58) gives us the ODE

$$\frac{\mathrm{d}R}{\mathrm{d}\tau} = -\frac{1 - P_a^2}{2(1 - R)}. \tag{3.61}$$

Based on the initial condition from (3.59), our drying front in Cartesian coordinates based on leading-order asymptotics, $R_{\text{Cart}}(\tau)$, is

$$R_{\text{Cart}}(\tau) = 1 - \sqrt{(1 - P_a^2)\tau}. \tag{3.62}$$

By returning to the original timescale of Region ii, we determine that P_0 can be fully expressed in Cartesian coordinates as

$$P_0^{\text{Cart}}(r, t) = \sqrt{P_a^2 + (1 - r)\sqrt{\frac{1 - P_a^2}{\delta\left(t - t^*_{\text{Cart}}\right)}}}. \tag{3.63}$$

Finally, we determine from (3.62) that the time to completely dry a bean based on leading-order asymptotics is

$$t^{\text{dry}}_{\text{Cart}} = t^*_{\text{Cart}} + \frac{1}{\delta(1 - P_a^2)}. \tag{3.64}$$

Using parameter values shown in Chapter 2, as well as typical values $P_a = 0.0879$, $\delta = 0.1011$, $\sigma = 0.0842$, and $t^*_{\text{Cart}} \approx 0.494$, we compute that $t^{\text{dry}}_{\text{Cart}} \approx 10.46$, or about 2768 seconds in dimensional units.

3.2.3.2 Determining $R(t)$ in Spherical Coordinates with $T^* \equiv 1$

In the limiting case where $\delta \ll 1$, i.e. $T^* \equiv 1$, we have that in spherical coordinates, by solving (3.57),

$$P_0(r, \tau) = \sqrt{1 - \left(\frac{1 - P_a^2}{r}\right)\left(\frac{r - R(\tau)}{1 - R(\tau)}\right)}, \tag{3.65}$$

and the Stefan condition (3.58) gives us the ODE

$$\frac{\mathrm{d}R}{\mathrm{d}\tau} = -\frac{1 - P_a^2}{2R(1 - R)}. \tag{3.66}$$

We use our initial condition (3.59) to give us, in implicit form, that the inverse function of the drying front in spherical coordinates, $\tau_{\text{Sph}}(R)$, satisfies the equation

$$\tau_{\text{Sph}}(R) = \frac{1 - R^2(3 - 2R)}{3(1 - P_a^2)}. \tag{3.67}$$

We can invert (3.67) and solve $R_{\text{Sph}}(\tau)$ in the correct domain and range:

$$R_{\text{Sph}}(\tau) = \frac{1}{2}\left(1 - \frac{\exp\left(\frac{2\pi \mathrm{i}}{3}\right)}{\Xi\left(3(1 - P_a^2)\tau\right)} - \exp\left(\frac{-2\pi \mathrm{i}}{3}\right)\Xi\left(3(1 - P_a^2)\tau\right)\right), \tag{3.68}$$

where

$$\Xi(\chi) = \sqrt[3]{2\sqrt{\chi(\chi - 1)} - 2\chi + 1} \tag{3.69}$$

and $\Xi(\chi)$ uses the principal branch of the cube root. Now that we have determined $R(\tau)$ in spherical coordinates, we can return to our original timescale of the problem and obtain that our leading-order asymptotic approximation for P is

$$\tilde{P}_0^{\text{Sph}}(r, t) = \sqrt{1 - \left(\frac{1 - P_a^2}{r}\right)\left(1 - \frac{2(1 - r)}{1 + \frac{\exp\left(\frac{2\pi \mathrm{i}}{3}\right)}{\Xi\left(3\delta(1 - P_a^2)(t - t^*_{\text{Sph}})\right)} + \exp\left(\frac{-2\pi \mathrm{i}}{3}\right)\Xi\left(3\delta(1 - P_a^2)(t - t^*_{\text{Sph}})\right)}\right)}. \tag{3.70}$$

To determine the time where the bean becomes fully dry, we substitute $R = 0$ into (3.67) to obtain, in our original timescale, that

$$t^{\text{dry}}_{\text{Sph}} = t^*_{\text{Sph}} + \frac{1}{3\delta(1 - P_a^2)}. \tag{3.71}$$

Therefore, to leading order, the time for a spherical coffee bean to dry out completely is $t^{\text{dry}}_{\text{Sph}} \approx 3.495$, or about 925 seconds in dimensional units. Figure 3.2(a) shows a comparison between the Cartesian and spherical asymptotic approximations of $R(t)$.

3.2.4 Comparison of Asymptotic Approximations with Numerical Results

We now compare the asymptotic approximations we have developed with the numerical solution of the PDE system (3.1)-(3.3), considering the drying front $R(t)$ in particular. We solve the PDE system (3.1)-(3.3) in MATLAB using the method of lines and a second-order central finite difference scheme in space. We use a stiff adaptive ODE solver in time, namely the MATLAB function `ode15s`, to achieve con-

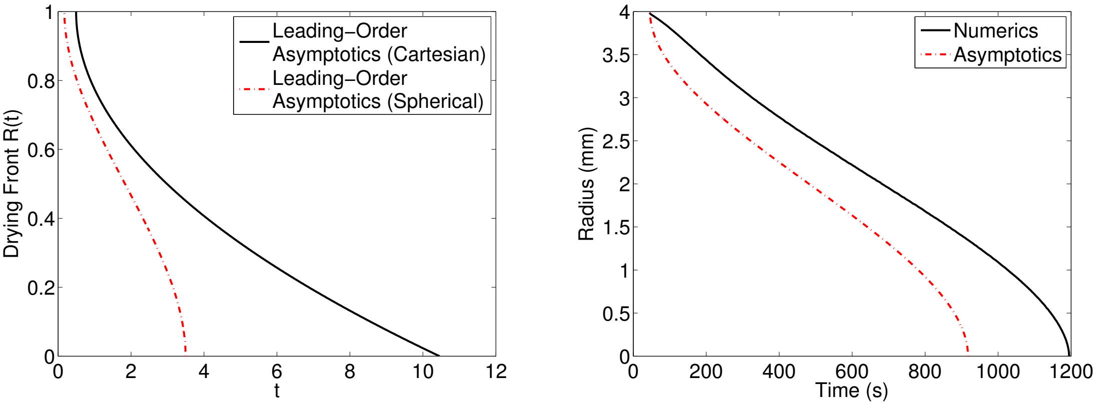

(a) (b)

Figure 3.2: Comparison of predictions of the drying front position $R(t)$ for the variable temperature regime. (a) Predictions $R_{\text{Cart}}(t)$ from (3.62) and $R_{\text{Sph}}(t)$ from (3.68). (b) Spherical predictions $R_{\text{Sph}}(t)$ from (3.68), shown in dash-dot red, and numerical solutions of (3.1)-(3.8), shown in black. All predictions in (b) are shown in dimensional units.

vergence. As we can see in Figure 3.2(b), the general shape of the dimensional drying front $R(t)$ agrees reasonably well with the dimensional drying front seen in the numerical solution, especially as $R(t) \to 0$. However, we also see that the drying time in the numerical solution is larger than the predicted $t^{\text{dry}}_{\text{Sph}}$ from asymptotic results. This is to be expected, as the asymptotic results used were for when the Stefan number $\frac{1}{\delta} \to +\infty$. Therefore, for a smaller (but still large) Stefan number, we expect the drying time to be longer. Additionally, these approximations for the drying front $R(t)$ assume $T^* \equiv 1$. Because $T^*(t)$ is less than unity in the numerical simulations, this will cause the drying front to be slower than the asymptotic approximation, which can explain why the numerical solution takes longer to dry out the entire bean.

3.3 Asymptotics of the Multiphase Model with Constant Temperature

In Section 3.2, we have given an analysis of the leading-order equations governing Region i, Region ii, and the transition layer. However, the numerical solutions indicate the thermal timescale of the multiphase model is much smaller than the vapour diffusive timescale. In consequence, it seems reasonable to examine a reduced model where the coffee bean is at the externally imposed roasting temperature throughout. Additionally, many of the leading-order equations can be solved explicitly if the temperature is spatially uniform and this helps in interpreting the behaviour of the moisture content and vapour pressure. Therefore, we are motivated from a physical and an asymptotics point of view to consider a reduced model with $T \equiv 1$. We note that this approximation means that the initial heating of the bean is not considered.

In this section, we assume that $T \equiv 1$ throughout the bean, which this means that the transition region is created immediately (i.e. $t^* = 0$) and the system of PDEs (3.1)-(3.2) become

$$\frac{\partial S}{\partial t} = -\frac{I_v}{\epsilon^2}, \tag{3.72}$$

$$\frac{\partial}{\partial t}\left[(1-\sigma S)P\right] = \frac{I_v}{\delta\epsilon^2} + \nabla \cdot \left(P\nabla P\right), \tag{3.73}$$

$$I_v = (1-P)S(1-\sigma S), \tag{3.74}$$

with boundary conditions

$$P\Big|_{r=1} = P_a, \qquad \frac{\partial P}{\partial r}\bigg|_{r=0} = 0, \tag{3.75}$$

and initial conditions

$$S(r,0) = 1, \quad P(r,0) = 1. \tag{3.76}$$

Formally, we will consider the asymptotics of this system in the limit as $\epsilon \to 0^+$. We will take $\delta = O(1)$ except where significant simplification is found by taking $\delta \ll 1$, and all other parameters are assumed to be $O(1)$.

3.3.1 Asymptotics in Region i

In Region i, we have that $P = 1$ to leading order. In fact, we note that $P, S \equiv 1$ is the exact solution in Region i, as these constant solutions satisfy both PDEs, the initial conditions, and the symmetry condition in P at $r = 0$. It is important to note that, since we assume that Region i is never in contact with the surface of the bean, the boundary condition at $r = 1$ does not apply.

3.3.2 Asymptotics of the Transition Layer

As in Section 3.2, we introduce the scaling $r = R(t) + \epsilon\hat{r}$ to examine the behaviour as S transitions from 1 to 0. Again, we can expand P and S as asymptotic series as $\epsilon \to 0$:

$$S = S_0(\hat{r},t) + \epsilon S_1(\hat{r},t) + O(\epsilon^2), \quad P = 1 + \epsilon P_1(\hat{r},t) + O(\epsilon^2). \tag{3.77}$$

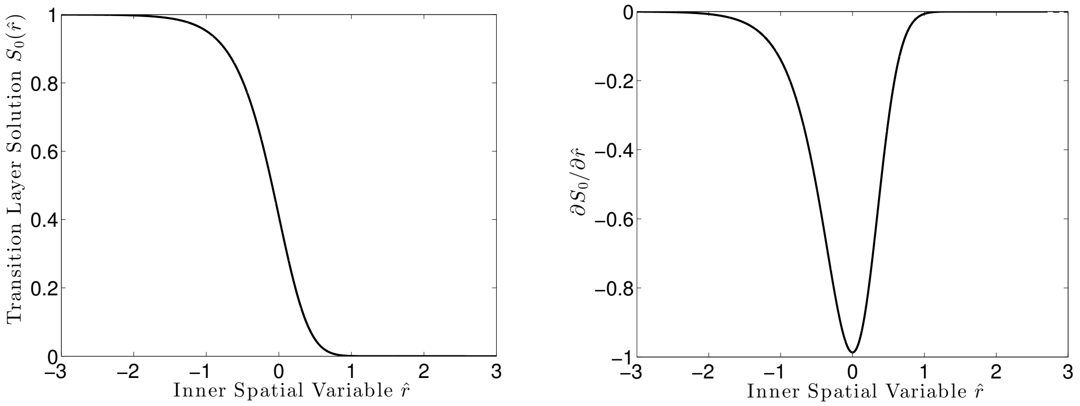

Figure 3.3: Numerical solution of the ODE (3.79). The left panel shows the solution $S_0(\hat{r})$ and the right panel shows its spatial derivative $\frac{\partial S_0}{\partial \hat{r}}$. For uniqueness, we pick a constant of integration so that $S_0(\hat{r})$ has an inflection point at $r = 0$.

Noting that temperature is constant (implying that $T_1 \equiv 0$ and $T^* \equiv 1$), the equation (3.42) for $\Upsilon(S_0)$ reduces to $\Upsilon(S_0) \equiv \frac{1}{\delta} - \sigma$. From (3.37), this gives us

$$\frac{\partial P_1}{\partial \hat{r}} = \left(\frac{1}{\delta} - \sigma\right) R'(t)(1 - S_0), \tag{3.78}$$

and from (3.43), gives us the first-order non-linear autonomous ODE:

$$\frac{\partial S_0}{\partial \hat{r}} = -S_0(1 - \sigma S_0)\sqrt{2\left(\frac{1}{\delta} - \sigma\right)\left[\frac{1-\sigma}{\sigma}\log\left(\frac{1-\sigma}{1-\sigma S_0}\right) + \log\left(\frac{1}{S_0}\right)\right]}, \tag{3.79}$$

with matching conditions $S_0 \to 0$ as $\hat{r} \to +\infty$ and $S_0 \to 1$ as $\hat{r} \to -\infty$. It is important to note a few key points about equation (3.79). Firstly, it is not explicitly solvable. Secondly, due to translational invariance, we require an additional constraint for uniqueness. This can be achieved, for example, by assuming the unique inflection point of S_0 occurs at $r = 0$. With this additional constraint, we numerically solve (3.79) and plot the results in Figure 3.3.

3.3.3 Asymptotics in Region ii

In Region ii, we have, from (3.72), that $S = 0$ at $O(\epsilon^{-2})$, which again causes a cascading effect in the asymptotic expansion of (3.72). Similar to what was done in

Section 3.2, we find that S is exponentially small in Region ii and is given by

$$S = \left\{ (1-\sigma) \exp\left[\frac{1}{\epsilon^2} \left(t - \int_0^t P(r,s)\, \mathrm{d}s \right) \right] + \sigma \right\}^{-1}. \tag{3.80}$$

Additionally, by neglecting exponentially small S, (3.73) becomes

$$\frac{\partial P}{\partial t} = \nabla \cdot (P \nabla P). \tag{3.81}$$

From (3.78), our boundary and initial conditions become

$$P\Big|_{r=1} = P_a, \qquad P\Big|_{r\to R(t)} \to 1, \qquad \frac{\partial P}{\partial r}\Big|_{r\to R(t)} \to \left(\frac{1}{\delta} - \sigma \right) R'(t), \qquad R(0) = 1. \tag{3.82}$$

This problem has a similarity solution in Cartesian coordinates, as will be shown in Section 3.3.3.1, although it cannot be explicitly solved. However, we can also examine the physically relevant large Stefan-number limit by letting $\delta \to 0^+$, as was done in Section 3.2.3. By rescaling time with $\tau = \delta t$ and considering the asymptotic series

$$P \sim P_0(r,\tau) + \delta P_1(r,\tau) + O(\delta^2), \tag{3.83}$$

(3.81)-(3.82) become

$$\nabla \cdot (P_0 \nabla P_0) = 0, \quad P_0\Big|_{r=1} = P_a, \quad P_0\Big|_{r\to R(\tau)} \to 1, \quad \frac{\partial P_0}{\partial r}\Big|_{r\to R(\tau)} \to R'(t), \quad R(0) = 1. \tag{3.84}$$

Solving (3.84) as in Section 3.2, we determine that in Cartesian coordinates,

$$P_0(r,t) = \sqrt{P_a^2 + (1-r)\sqrt{\frac{1-P_a^2}{\delta t}}}, \quad R(t) = 1 - \sqrt{(1-P_a^2)\delta t}, \tag{3.85}$$

and in spherical coordinates,

$$\begin{aligned} \tilde{P}_0(r,t) &= \sqrt{1 - \left(\frac{1-P_a^2}{r} \right) \left[1 - \frac{2(1-r)}{1 + \frac{\exp\left(\frac{2\pi \mathrm{i}}{3}\right)}{\Xi(3(1-P_a^2)\delta t)} + \frac{\Xi(3(1-P_a^2)\delta t)}{\exp\left(\frac{2\pi \mathrm{i}}{3}\right)}} \right]}, \\ R(t) &= \frac{1}{2} \left(1 - \frac{\exp\left(\frac{2\pi \mathrm{i}}{3}\right)}{\Xi\left(3(1-P_a^2)\delta t\right)} - \frac{\Xi\left(3(1-P_a^2)\delta t\right)}{\exp\left(\frac{2\pi \mathrm{i}}{3}\right)} \right), \end{aligned} \tag{3.86}$$

where

$$\Xi(\chi) = \sqrt[3]{2\sqrt{\chi(\chi-1)} - 2\chi + 1}. \tag{3.87}$$

3.3.3.1 Determining $R(t)$ in Cartesian Coordinates using Similarity Solutions

One might consider using a similarity solution to solve the system (3.81)-(3.82) in Cartesian coordinates without the assumption that $\delta \ll 1$. To do this, we let

$$P = h(\eta), \quad \text{where} \quad \eta = \frac{1-r}{\sqrt{t}}. \tag{3.88}$$

Substituting the transformation (3.88) into (3.81) gives

$$(h(\eta)h'(\eta))' + \frac{\eta}{2}h'(\eta) = 0, \tag{3.89}$$

and (3.82) becomes

$$h(0) = P_a, \qquad h(\lambda) = 1, \qquad h'(\lambda) = \frac{\lambda\,(1-\delta\sigma)}{2\delta}. \tag{3.90}$$

Here, $\eta = \lambda$ corresponds to the moving boundary $R(t)$. Thus, our drying front based on the Cartesian similarity solution, is given by

$$R_{\mathrm{SS}}(t) = 1 - \lambda\sqrt{t}. \tag{3.91}$$

We note that our choice of η allows us to automatically satisfy the initial condition $R(0) = 1$ and we can determine from this equation when the bean will be completely dry, i.e. when $R_{\mathrm{SS}}(t) = 0$. This gives us $t_{SS}^{\mathrm{dry}} = \frac{1}{\lambda^2}$. As (3.89) is not explicitly solvable, it is necessary to numerically solve this boundary value problem in order to determine λ. Using the shooting method, with the typical values $P_a = 0.0879$, $\delta = 0.1011$, and $\sigma = 0.0842$, we find that $\lambda \approx 0.3152$, implying that $t_{SS}^{\mathrm{dry}} \approx 10.06$, or about 2664 seconds in dimensional units. With less than a 1% relative error compared to t_{SS}^{dry}, we conclude that $t_{\mathrm{Cart}}^{\mathrm{dry}} \approx 9.964$, as described in (3.64), is a very good approximation to the drying time computed from the similarity solution. Figure 3.4(a) shows a comparison of the drying front $R_{\mathrm{SS}}(t)$ with the Cartesian drying front determined previously via asymptotic methods, namely, $R_{\mathrm{Cart}}(t)$ given in (3.62).

3.3.3.2 Numerical Solution of the Region ii PDE

Another method to determine $R(t)$ without using the large Stefan limit is by solving (3.81)-(3.82) numerically. To do this, we set the problem in a fixed domain by making the change of variables

$$\mu = \frac{1-r}{1-R(t)}, \mathcal{P} = P(\mu, t), \tag{3.92}$$

yielding the PDE

$$\frac{\partial \mathcal{P}}{\partial t} + \left(\frac{\mu R}{1-R}\right)\frac{\partial \mathcal{P}}{\partial \mu} = \frac{\tilde{\nabla}\cdot\left(\mathcal{P}\tilde{\nabla}\mathcal{P}\right)}{(1-R)^2}, \tag{3.93}$$

while the transformed boundary and initial conditions become

$$\mathcal{P}\Big|_{\mu=0} = P_a, \quad \mathcal{P}\Big|_{\mu\to 1} \to 1, \quad \frac{\partial \mathcal{P}}{\partial \mu}\Big|_{\mu\to 1} \to \frac{R'(R-1)}{K}, \quad \mathcal{P}(\mu,0)\equiv 1, \quad R(0)=1. \tag{3.94}$$

Here, we define $K = \left(\frac{1}{\delta}-\sigma\right)^{-1}$. In spherical coordinates, our PDE can be written as

$$\frac{\partial \mathcal{P}}{\partial t} = \left(\frac{1}{1-R}\right)^2\left[\frac{\partial}{\partial \mu}\left(\mathcal{P}\frac{\partial \mathcal{P}}{\partial \mu}\right) - (1-R)\left(\mu R' + \frac{2\mathcal{P}}{1-\mu(1-R)}\right)\frac{\partial \mathcal{P}}{\partial \mu}\right]. \tag{3.95}$$

We discretise using central differencing in μ, e.g.

$$\begin{aligned} \frac{\partial \mathcal{P}}{\partial \mu} &= \frac{P_{i+1}-P_{i-1}}{2\Delta\mu} + O\left((\Delta\mu)^2\right), \\ \frac{\partial}{\partial \mu}\left(\mathcal{P}\frac{\partial \mathcal{P}}{\partial \mu}\right) &= \frac{P_{i+1}^2 - 2P_i^2 + P_{i-1}^2}{2(\Delta\mu)^2} + O\left((\Delta\mu)^2\right), \quad i = 0,\ldots,N. \end{aligned} \tag{3.96}$$

Additionally, we use the Stefan condition to approximate $R'(t)$ when solving for $\mathcal{P}$, e.g.

$$R' = \left(\frac{K}{1-R}\right)\left(\frac{3P_N - 4P_{N-1} + P_{N-2}}{2\Delta\mu}\right) + O\left((\Delta\mu)^2\right). \tag{3.97}$$

Finally, by using an implicit time-stepping routine to achieve convergence, our numerical routine is implemented as follows:

$$\begin{aligned}
P_i^{j-1} =& P_i^j - \left(\frac{\Delta t}{2\Delta\mu}\right)\left(\frac{1}{1-R^j}\right)^2 \Bigg\{ \frac{P_{i+1}^{2,j} - 2P_i^{2,j} + P_{i-1}^{2,j}}{\Delta\mu} \\
&+ (R^j - 1)(P_{i+1}^j - P_{i-1}^j)\left[\left(\frac{K\mu_i}{2\Delta\mu}\right)\left(\frac{3P_N^j - 4P_{N-1}^j + P_{N-2}^j}{1-R^j}\right)\right. \qquad (3.98) \\
&+ \left.\frac{2P_i^j}{1-\mu_i(1-R^j)}\right]\Bigg\}, \\
R^j =& R^{j+1} - \left(\frac{K\Delta t}{2\Delta\mu}\right)\left(\frac{3P_N^j - 4P_{N-1}^j + P_{N-2}^j}{1-R^{j+1}}\right). \qquad (3.99)
\end{aligned}$$

This system of algebraic equations is solved in MATLAB using the function `fsolve` to determine P_i^j, followed by the function `fzero` to determine R^{j+1}. The algorithm terminates when $R^{j+1} < 0$.

3.3.4 Comparison of Asymptotic Approximations with Numerical Results

Comparing the various asymptotic approximations with the numerical solutions of (3.72)-(3.76), we can see in Figure 3.4(b) that the general shape of the dimensional drying front $R(t)$ agrees well with the dimensional drying front seen in the full numerical solution. Because we have assumed that $T^* \equiv 1$, we no longer have differences induced by varying the temperature that were seen Section 3.2. Therefore, it is expected that the drying front $R(t)$ determined via asymptotics fits closer to the numerics. We see, as in Section 3.2, that the drying time predicted by the numerical solution is larger than $t_{\mathrm{Sph}}^{\mathrm{dry}}$ determined from asymptotic results in (3.71). However, this is to be expected; a large (but finite) Stefan number would cause the drying time to be longer than the time produced by the limit $\delta \to 0^+$. This is confirmed by comparing the drying front in the full numerical solution with the drying front obtained by solving (3.81)-(3.82) numerically, as discussed in Section 3.3.3.2. Indeed, by allowing $\epsilon \to 0^+$, we only observe significant discrepancies between these two drying fronts near the surface and the centre of the bean. This is to be expected, as the transition layer will be on a semi-infinite region in both of these cases and will have different behaviour due to the boundary conditions.

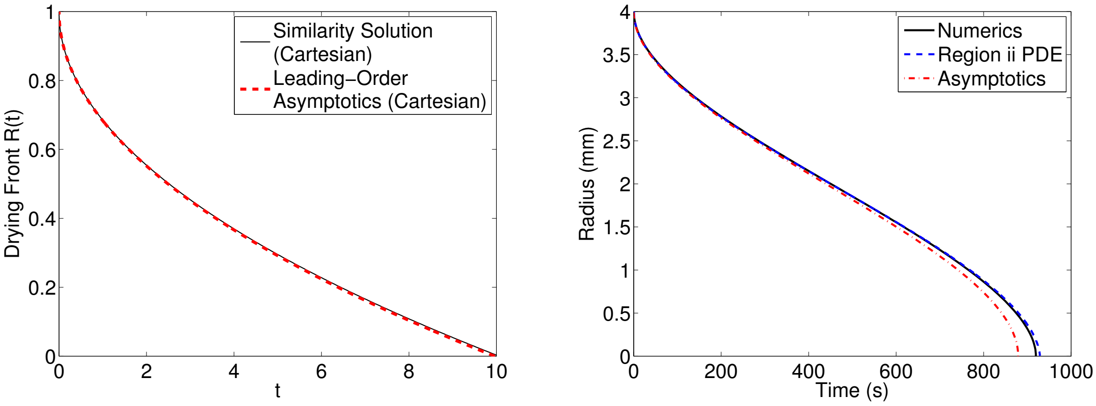

(a) (b)

Figure 3.4: Comparison of predictions of the drying front position $R(t)$ for the constant temperature regime. (a) Cartesian predictions $R_{\mathrm{SS}}(t)$ from (3.91) and $R_{\mathrm{Cart}}(t)$ from (3.85). (b) Spherical predictions $R_{\mathrm{Sph}}(t)$ from (3.86), shown in dash-dot red, and numerical solutions of (3.72)-(4.4), shown in black, and of (3.81)-(3.82), shown in dashed blue. All predictions in (b) are shown in dimensional units.

3.4 Discussion

In this chapter, we have extended results of the "simplified" form of the multiphase model presented in Chapter 2 via asymptotic methods, in order to better understand the qualitative features of the coffee bean roasting process. Motivated by previous numerical results, we considered the limit $\epsilon \to 0^+$, representing the situation where the rate of vapour transport by Darcy flow is much smaller than the evaporation rate. The asymptotic analysis showed that the solution could be divided into two main regions and a transition layer. The entire bean was in the first region until a time t^*, when a thin transition layer appears at the surface of the bean. This transition layer then propagated into the bean creating a second main region between it and the surface of the bean. This asymptotic limit is different from what has been studied previous in drying models, since the rigid cellulose structure of the solid coffee bean creates a large build-up of vapour pressure that drives the vapour to the external environment. The analysis shows that a narrow drying front, represented by the transition layer, is crucial to the drying process in this limit.

In the first region, the vapour pressure is in equilibrium with the steam table pressure and the moisture content of the bean remains at its initial value, with heat flow governed by the heat equation. In the thin transition region, the moisture content changes rapidly from its initial value to a small value. Here, evaporation dominates and the temperature and vapour pressure remain spatially uniform. Finally, in the second main region, there is almost no water and therefore no evaporation. The problem in this second region consists of diffusion equations for the heat and vapour flow with coupling through the matching conditions to the transition layer, similar to a Stefan problem.

Numerical simulations suggest that the externally applied roasting temperature is attained globally fairly quickly; hence, the case where temperature is fixed at the roasting temperature was considered. This also allowed the coupled Stefan problem to be reduced to a single Stefan problem, which could then be solved via similarity solutions or large Stefan number asymptotics. The leading order expressions are shown to agree well with the dynamics of the drying front found from numerical simulations, under both spherical and planar geometries.

Despite several simplifications made in obtaining asymptotic solutions in each of the regions of the coffee bean, a reasonable agreement between the asymptotic approximations and the numerical solution of the multiphase model as described in Chapter 2 has been obtained. This suggests that the asymptotics found here accurately capture the qualitative behaviour of the coffee bean roasting process, and provide an acceptable compromise between a simpler heat transfer model (such as those presented in [13]) and more complicated multiphase models. However, we will see in Chapter 4 that the leading-order behaviour of the Multiphase Model changes when more general evaporation rates are considered.

Chapter 4

Extensions of Evaporation Mechanisms in Multiphase Drying Models

4.1 Introduction

The asymptotic analysis of a multiphase drying model seen in Chapter 3 successfully reduces the complexity of the mathematical models in question while retaining the salient features of drying. In particular, we are able to find approximate solutions of the Multiphase Model (described in Chapter 2) because of the evaporation timescale being significantly smaller than the vapour diffusive timescale and the particular form of the evaporation rate motivated by Langmuir [31]. This evaporation rate has two equilibria: when the vapour is aligned with its steam table pressure and when the water saturation is zero. Crucially, we note that the steam table pressure, given by [10] and employed in Langmuir's equation, is independent of water saturation. Therefore, for the vapour pressure boundary condition in the Multiphase Model to be satisfied, there must be a transition region between the evaporation rate's equilibria.

In this chapter, we shall extend evaporation mechanisms used in Chapter 2's Multiphase Model in a number of ways. Specifically, we wish to understand how modifying the Langmuir equation to more general evaporation rates affects the dynamics of the Multiphase Model. As Langmuir's equation assumes a number of simplifications (an unconfined domain, zero impurities in the water, no restrictions to accessing the water, etc.), more general evaporation rates are essential in understanding drying mechanisms in roasting coffee beans.

The first generalized evaporation rate that we examine is a separable function of saturation S and vapour pressure P. We will show that the asymptotic analysis seen in Section 3.3 remains unchanged in the equilibria regions, i.e. Regions i and ii. However, evaporation dynamics dominate in the thin transition region that connects Regions i and ii, where the separable evaporation rates exhibit different behaviour from the Langmuir equation.

Motivated in part by literature on timber drying (e.g. [44]), we consider a second, more detailed, mechanism for the evaporation rate via a *sorption isotherm*. In particular, we incorporate water activity ([29, 40]) into our evaporation rate to account for how water changes phase from liquid to vapour within a coffee bean structure. As this evaporation rate now includes a saturation dependence on the equilibrium vapour pressure, we will show that the “drying front” seen in Chapters 2 and 3 no longer exists. Furthermore, while certain simplifications can be made via asymptotic analysis, we are unable to determine the water saturation other than by numerical methods.

4.2 General Separable Evaporation Rates under Isothermal Simplifications

In this section, we focus on more general evaporations that can be employed in the isothermal Multiphase Model discussed in Section 3.3. Specifically, we will assume that the evaporation rate, denoted as I_v, is a separable function of saturation S and vapour pressure P. As discussed in Chapter 3, we note that many of the salient features of drying, such as the aforementioned “drying front”, continue to hold in an isothermal setting. Because of this, and the simplified equations that result, we will focus on general separable evaporation rates in an isothermal setting; as discussed in Section 3.3, the system of PDEs become

$$\frac{\partial S}{\partial t} = -\frac{I_v}{\epsilon^2}, \tag{4.1}$$

$$\frac{\partial}{\partial t}\left[(1-\sigma S)P\right] = \frac{I_v}{\delta\epsilon^2} + \nabla\cdot\left(P\nabla P\right), \tag{4.2}$$

with boundary conditions

$$P\Big|_{r=1} = P_a, \qquad \left.\frac{\partial P}{\partial r}\right|_{r=0} = 0, \tag{4.3}$$

and initial conditions

$$S(r,0) = 1, \quad P(r,0) = 1. \tag{4.4}$$

In Chapter 3, we assumed that the evaporation rate I_v has taken the form (3.74) in the isothermal model. It is quite possible that this Langmuir's evaporation rate [31] may not be the best way to model water evaporation in a roasting coffee bean. We therefore briefly examine a larger class of evaporation rates in order to highlight the differences a revised model would present. We will now consider a general class of evaporation rates, in which I_v can be written as

$$I_v(S,P) = -\epsilon F(S) G\left(\frac{P-1}{\epsilon}\right), \tag{4.5}$$

such that F, G are continuous functions independent of ϵ and satisfy the conditions

$$F(0) = 0, \tag{4.6}$$

$$F(S) > 0 \text{ for all } S \in (0,1), \tag{4.7}$$

$$G(0) = 0, \tag{4.8}$$

$$G'(0) = \lambda > 0. \tag{4.9}$$

Physically speaking, (4.6) implies that evaporation does not occur with zero water content, and (4.7) indicates that evaporation will not stop if a bean is partially saturated. Additionally, (4.8) tells us that no evaporation occurs when the vapour pressure is at steam table pressure. However, (4.9) means that a small decrease in vapour pressure from the steam table pressure will cause evaporation (rather than condensation) to occur. To relate back to Langmuir's evaporation rate, this would be the case where $F(S) = S(1-\sigma S)$ and $G(\psi) = \psi$.

4.2.1 Asymptotics of the Multiphase Model for Separable Evaporation Rates

Under this general separable form of I_v, the leading-order solutions in Regions i and ii observed in Chapter 3 remain the same, as Region i still follows from (4.8) and Region ii follows from (4.6). In other words, we will still have a region where the vapour pressure is aligned with its equilibrium pressure (Region i), joined to a nearly-dry region (Region ii) by a thin transition region near a "drying front", denoted here as $R(t)$. However, in the transition layer, we can show the dynamics for more general classes of evaporation rates. Using the same asymptotic series expansion as shown in Chapter 3, our leading-order equation for (4.1) becomes

$$-R'(t)\frac{\partial S_0}{\partial \hat{r}} = F(S_0)G(P_1), \tag{4.10}$$

and our leading-order equation for (4.2) becomes

$$\delta\left[\frac{\partial^2 P_1}{\partial \hat{r}^2} - \sigma R'(t)\frac{\partial S_0}{\partial \hat{r}}\right] = F(S_0)G(P_1), \tag{4.11}$$

where $r = R(t) + \epsilon\hat{r}$. Additionally, the matching conditions

$$S_0 \to 1, \quad \text{and} \quad P_1 \to 0 \quad \text{as} \quad \hat{r} \to -\infty, \tag{4.12}$$

$$S_0 \to 0 \quad \text{as} \quad \hat{r} \to +\infty, \tag{4.13}$$

$$\left.\frac{\partial P_1}{\partial \hat{r}}\right|_{\hat{r}\to+\infty} = \left.\frac{\partial P}{\partial r}\right|_{r\to R(t)}, \tag{4.14}$$

remain the same. By equating (4.10) with (4.11) and using (4.12), we determine that our relationship between P_1 and S_0 remains the same as in Chapter 3:

$$\frac{\partial P_1}{\partial \hat{r}} = R'(t)\left(\frac{1}{\delta} - \sigma\right)(1 - S_0). \tag{4.15}$$

Thus, the Stefan condition (4.15) for Region ii (as discussed in Chapter 3 is the same, implying that the asymptotics for Regions i and ii are identical for all general evaporation rates of the form stated previously. Now, by dividing (4.15) by (4.10), we obtain the following differential equation for P_1 in terms of S_0:

$$\frac{\mathrm{d}P_1}{\mathrm{d}S_0} = -\frac{R'(t)^2\left(\frac{1}{\delta} - \sigma\right)(1 - S_0)}{F(S_0)G(P_1)}. \tag{4.16}$$

By separating variables, we can integrate (4.16) and impose the matching conditions (4.12) once again and obtain

$$\int_0^{P_1} G(\psi)\mathrm{d}\psi = (R'(t))^2\left(\frac{1}{\delta} - \sigma\right)\int_0^{1-S_0} \frac{\chi}{F(1-\chi)}\mathrm{d}\chi. \tag{4.17}$$

By defining

$$\mathscr{F}(Y) = \int_0^{Y} \frac{\chi}{F(1-\chi)}\mathrm{d}\chi, \tag{4.18}$$

we have that

$$S_0 = 1 - \mathscr{F}^{-1}\left(\frac{\int_0^{P_1} G(\psi)\mathrm{d}\psi}{(R'(t))^2\left(\frac{1}{\delta}-\sigma\right)}\right). \tag{4.19}$$

Substituting (4.19) into (4.15), and noting that the only variable in the function $\mathscr{F}^{-1}$ that depends on $\hat{r}$ is P_1, we can separate the subsequent differential equation and obtain that

$$\mathscr{G}(P_1) := \int^{P_1} \frac{\mathrm{d}\tilde{P}}{\mathscr{F}^{-1}\left(\frac{\int_0^{\tilde{P}} G(\psi)\mathrm{d}\psi}{(R'(t))^2\left(\frac{1}{\delta}-\sigma\right)}\right)} = R'(t)\left(\frac{1}{\delta}-\sigma\right)(\hat{r}-C), \tag{4.20}$$

where C is chosen so that the matching condition (4.12) is satisfied. Thus, by a final inversion of the function $\mathscr{G}$, as well as substituting back into (4.19), our solutions in the transition layer are

$$\begin{aligned} P_1(\hat{r},t) &= \mathscr{G}^{-1}\left(R'(t)\left(\frac{1}{\delta}-\sigma\right)(\hat{r}-C)\right), \\ S_0(\hat{r},t) &= 1 - \mathscr{F}^{-1}\left(\frac{\int_0^{P_1} G(\psi)\mathrm{d}\psi}{(R'(t))^2\left(\frac{1}{\delta}-\sigma\right)}\right). \end{aligned} \tag{4.21}$$

In general, the functions $\mathscr{F}$, $\mathscr{F}^{-1}$, $\mathscr{G}$, and $\mathscr{G}^{-1}$ are not easy to determine. However, the main purpose of examining the transition layer is to examine the leading-order behaviour of S. One way to do this is to determine the leading-order differential equation for S by approximating $G(\psi)$ near $\psi = 0$. Since $P \sim 1 + \epsilon P_1$ in the transition layer, we can make the approximation that $G(P_1) \sim \lambda P_1$. Rearranging (4.10) and differentiating the expression with respect to $\hat{r}$, as well as substitute in (4.15), this gives us the differential equation

$$\frac{\partial^2 S_0}{\partial \hat{r}^2} - \left(\frac{\partial S_0}{\partial \hat{r}}\right)^2 \frac{F'(S_0)}{F(S_0)} + \lambda\left(\frac{1}{\delta}-\sigma\right)(1-S_0)F(S_0) = 0. \tag{4.22}$$

If we allow $u = S_0$ and $w = \left(\frac{\partial S_0}{\partial \hat{r}}\right)^2$, we obtain, in similar nature by methods shown in Section 3.2.2, that

$$\frac{\mathrm{d}w}{\mathrm{d}u} - 2w\frac{F'(u)}{F(u)} = -2\lambda\left(\frac{1}{\delta}-\sigma\right)(1-u)F(u). \tag{4.23}$$

Multiplying (4.23) by the integrating factor $[F(u)]^{-2}$, as well as using the condition

$w = 0$ when $u = 1$, we find that

$$w = 2\lambda \left(\frac{1}{\delta} - \sigma\right) F(u)^2 \int_u^1 \frac{1-\chi}{F(\chi)} \mathrm{d}\chi. \tag{4.24}$$

Thus, if we return to our original variables of the differential equation, and choose the negative branch of the square root so $S_0(\hat{r})$ transitions from 1 to 0 as $\hat{r}$ increases, we have

$$\frac{\partial S_0}{\partial \hat{r}} = -F(S_0)\sqrt{2\lambda \left(\frac{1}{\delta} - \sigma\right) \int_{S_0}^1 \frac{1-\chi}{F(\chi)} \mathrm{d}\chi}. \tag{4.25}$$

Motivated by the form of this differential equation, we now consider a different evaporation rate that yields an explicit solution for both (4.21) and (4.25). Suppose that $F(S) = S^2(1-S)$ and $G(\psi) = \psi$, i.e.

$$\tilde{I}_v = S^2(1-S)(1-P). \tag{4.26}$$

This implies, after integrating inside the square root, that (4.25) becomes

$$\frac{\partial S_0}{\partial \hat{r}} = -\sqrt{2\left(\frac{1}{\delta} - \sigma\right)} \left[S_0(1-S_0)\right]^{\frac{3}{2}}. \tag{4.27}$$

This differential equation can be explicitly solved by separating variables and its solution is

$$S_0(\hat{r}) = \frac{1}{2}\left[1 - \frac{\hat{r} - C}{\sqrt{(\hat{r}-C)^2 + \frac{8\delta}{1-\delta\sigma}}}\right], \tag{4.28}$$

where C is an arbitrary constant. This also tells us, from (4.15), that

$$P_1(\hat{r}, t) = \frac{\left(\frac{1}{\delta} - \sigma\right) R'(t)}{2}\left[\hat{r} - C + \sqrt{(\hat{r}-C)^2 + \frac{8\delta}{1-\delta\sigma}}\right]. \tag{4.29}$$

These results can be verified by using (4.21) and noting that for this choice of $F(S)$ and $G(\psi)$,

$$\begin{aligned} \mathscr{F}(Y) &= \frac{Y}{1-Y}, \qquad \mathscr{F}^{-1}(Y) = \frac{Y}{1+Y}, \\ \mathscr{G}(Y) &= Y - \frac{2\left(R'(t)\right)^2\left(\frac{1}{\delta} - \sigma\right)}{Y}, \\ \mathscr{G}^{-1}(Y) &= \frac{1}{2}\left[Y + \sqrt{Y^2 + 8\left(R'(t)\right)^2\left(\frac{1}{\delta} - \sigma\right)}\right]. \end{aligned} \tag{4.30}$$

Therefore, for more general evaporation rates (4.5) that satisfying conditions (4.6)-(4.9), we have now shown that the asymptotic behaviour in Regions i and ii is the same as in the specific earlier case. Additionally, we have determined a general solution for the moisture content and vapour pressure in the transition layer, defined in terms of inverse functions of integrals. These results allow us to conclude that while Langmuir's evaporation rate may not be the best model to describe the evaporation of water in roasting coffee beans, the differences between Langmuir's equation and more general separable evaporation rates are only observed in the thin transition layer near the drying front.

4.3 The Sorption Isotherm

While separable evaporation rates, such as Langmuir's equation [31], provide great simplifications to multiphase drying models, they do not capture many crucial aspects of evaporation occurring in organic materials. Specifically, these separable equations do not account for the chemical binding to other materials (such as cellulose in the case of coffee beans), the surface tension of drying droplets, or the distribution and shape of water droplets present in organic materials. In consequence, we wish to extend the ideas of evaporation to capture more realistic drying mechanisms that occur in a roasting coffee bean. This section mainly comprises of results shown in [14].

We start by considering how water bound to the cellulose matrix (discussed in Chapter 1) might evaporate. This mechanism was omitted in Chapter 2, where it was assumed that there was no binding and so the evaporation was described by a simple Langmuir expression for pure water. In a real material, there is a distribution of different binding sites. One way of describing the sites is to consider the material in equilibrium, where every site is either empty or full. Hence, at a given equilibrium vapour pressure p_v^* and specified water activity a_w, it is possible to measure the mass fraction of water to dry solids, denoted here as X. This equilibrium vapour pressure has the form

$$p_v^* = a_w(X) p_{ST}(T), \tag{4.31}$$

where $p_{ST}(T)$ is the pure steam table pressure as given, for example, in [10]:

$$p_{ST}(T) = A_1 \exp(A_2 - A_3/T), \tag{4.32}$$

with A_1, A_2, and A_3 being constants. The binding site will fill if the vapour pressure is too high (i.e. $p_v > p_v^*$) and empty otherwise. This relationship is normally prescribed by the *sorption isotherm* (see e.g. [29, 40]).

In terms of variables presented here, we relate the bound water mass fractions to their volume fractions using

$$X = \frac{\frac{\rho_w}{\rho_s}\phi S}{1-\phi}, \tag{4.33}$$

where ρ_s is the density of the dry coffee solids, $1-\phi$ is the volume fraction occupied by the solid coffee bean, ϕS is the volume fraction occupied by liquid, and the sorption isotherm p_v^* is defined by

$$p_v^* = a_w(X) p_{ST}(T). \tag{4.34}$$

Many models relating a_w to X have been proposed (see for example [29]), but here we will consider the simple relationship proposed in [40]:

$$X = B_1 \left(\frac{a_w}{1-a_w} \right)^{B_2}, \tag{4.35}$$

implying that

$$a_w = \frac{(\phi S)^{C_1}}{(\phi S)^{C_1} + C_2 \sigma^{C_1} (1-\phi)^{C_1}}, \tag{4.36}$$

where σ is the initial volumetric liquid-to-void ratio in the coffee bean and $C_1 = \frac{1}{B_2}$ and $C_2 = \left[\frac{B_1 \rho_s}{\sigma \rho_w}\right]^{C_1}$ are constants. It is important to note that the density ratio $\frac{\rho_w}{\rho_s}$ in (4.33) is absorbed in the fitting parameter C_2. Therefore, our sorption isotherm p_v^*, relating vapour pressure to water content, can be written as

$$p_v^*(T, \phi, S) = \frac{P_0 D_1 (\phi S)^{C_1} \exp\left[-\frac{D_2 T_0}{T_\infty - T_0}\left(\frac{T_\infty}{T} - 1\right)\right]}{(\phi S)^{C_1} + C_2 \sigma^{C_1} (1-\phi)^{C_1}}, \tag{4.37}$$

where

$$D_1 = \frac{A_1}{P_0} \exp\left(A_2 - \frac{A_3}{T_\infty}\right) \quad \text{and} \quad D_2 = \frac{A_3 (T_\infty - T_0)}{T_0 T_\infty}. \tag{4.38}$$

Figure 4.1 shows how $a_w(S)$ varies with different values of C_1 and C_2 for fixed porosity. Comparing the model developed here with that used used in Chapter 2, we note that the previous sorption isotherm is independent of volumetric fractions (e.g. $C_2 = 0$). The literature on timber drying (see e.g. [44]) uses a similar approach, but assumes that the reaction is so rapid that the sorption isotherm is equal to the water vapour pressure. We also assume that this reaction is rapid, but will state the underlying governing conservation equations for completeness.

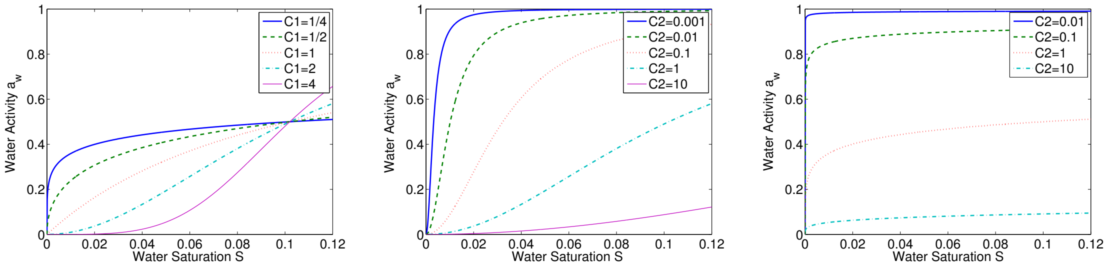

(a) (b) (c)

Figure 4.1: Comparison of the water activity function a_w, defined in (4.36), with $\phi = 0.5$ and $\sigma = 0.1$. (a) Parameter C_1 is varied with $C_2 = 1$. (b) Parameter C_2 is varied with $C_1 = 2$. (c) Parameter C_2 is varied with $C_1 = \frac{1}{4}$.

4.3.1 The Incorporation of p_v^* into the Multiphase Model

It is natural at this stage to compare the Multiphase Model shown in Chapter 2 with one incorporating the sorption isotherm. By changing $P_{ST}(T)$ in Chapter 2 with $P_v^*(T,S)$ shown in (4.37) with constant porosity, the modified Multiphase Model becomes

$$\frac{\partial S}{\partial t} = -\frac{1}{\epsilon^2} I_v, \tag{4.39}$$

$$\frac{\partial}{\partial t}\left[\frac{(1+\mathscr{T})P(1-\sigma S)}{1+\mathscr{T}T}\right] = -\frac{1}{\delta}\frac{\partial S}{\partial t} + \nabla\cdot\left[\frac{(1+\mathscr{T})P\nabla P}{1+\mathscr{T}T}\right], \tag{4.40}$$

$$\frac{\partial T}{\partial t} + \mathcal{A}_1\frac{\partial}{\partial t}\left[S(1+\mathscr{T}T)\right] = \mathcal{A}_2\frac{\partial S}{\partial t} + \mathcal{A}_3\nabla\cdot\left[(1+\mathcal{A}_4 S)\nabla T\right], \tag{4.41}$$

where

$$I_v = S(1-\sigma S)(P_v^*(T,S) - P)\sqrt{\frac{1+\mathscr{T}}{1+\mathscr{T}T}} \tag{4.42}$$

and

$$P_v^*(T,S) = \frac{S^{C_1}\exp\left(\frac{D_2(T-1)}{1+\mathscr{T}T}\right)}{S^{C_1}+C_3}, \tag{4.43}$$

and the boundary conditions are the same as employed in Chapter 3:

$$\nabla T\cdot\mathbf{n} = 0, \quad \nabla P\cdot\mathbf{n} = 0 \quad \text{at} \quad r = 0, \tag{4.44}$$

$$\nabla T\cdot\mathbf{n} = \nu\left(\frac{1-\sigma S}{1-\sigma}\right)\left(\frac{1+\mathcal{A}_4}{1+\mathcal{A}_4 S}\right)(1-T) \quad \text{at} \quad r = 1, \tag{4.45}$$

$$P\big|_{r=1} = \begin{cases} P_v^*(T,S), & T < T_a, \\ P_a, & T \geq T_a. \end{cases} \tag{4.46}$$

Here,

$$C_3 = C_2 \left(\frac{1-\phi}{\phi} \right)^{C_1}. \tag{4.47}$$

The initial conditions corresponding to uniform initial moisture content, room temperature, and equilibrium *sorption isotherm* pressure, i.e.

$$S(r,0) = 1, \quad T(r,0) = 0, \quad P(r,0) = P_v^*(0,1). \tag{4.48}$$

We can solve this modified Multiphase Model with the same parameters as used in Chapter 3, with $C_1 \approx 0.41$ and $C_3 \approx 6.1 \times 10^{-3}$ being given in [9] and $T_\infty = 230°\text{C}$. With reference to Figure 4.2, there are two main differences between these two models. Firstly, the moisture content decays significantly faster in the original Multiphase Model (without the sorption isotherm) than in the modified Multiphase Model with the sorption isotherm. Secondly, we note that the maximum vapour pressure inside the bean is much smaller in the modified Multiphase Model than in the original Multiphase Model. This is due to the water activity function reducing the maximal vapour pressure for a given moisture content, which in turn slows the rate at which water vapour can be transported to the outside of the bean.

4.3.2 Asymptotics of the Modified Multiphase Model

It is natural at this point to discuss the asymptotic behaviour of the modified Multiphase Model when the incorporated sorption isotherm. As seen in Chapter 3, we observe that $P \sim P_v^*(T,S)$ initially, corresponding to the "Region i" equilibrium. Crucially, we note that, due to P_v^* now being a function of S, we can now satisfy the boundary condition $P\big|_{r=1} = P_a$ without a transition layer or a dry Region ii. This is different to the Langmuir evaporation rate, where the pressure boundary condition required a change in evaporation equilibrium to the $S \ll 1$ dry equilibrium. Instead, we can satisfy the pressure boundary conditions by formulating equivalent boundary conditions in S based on the sorpotion isotherm function. Specifically, by employing the boundary conditions

$$\begin{aligned} \nabla S \cdot \mathbf{n}\big|_{r=0} &= 0, \\ S\big|_{r=1} = P_v^{*,-1}(T,P_a) &= \left[\frac{1}{C_3 P_a} \exp\left(\frac{\beta(T-1)}{1+\mathscr{T}T} \right) - \frac{1}{C_3} \right]^{-\frac{1}{C_1}}, \end{aligned} \tag{4.49}$$

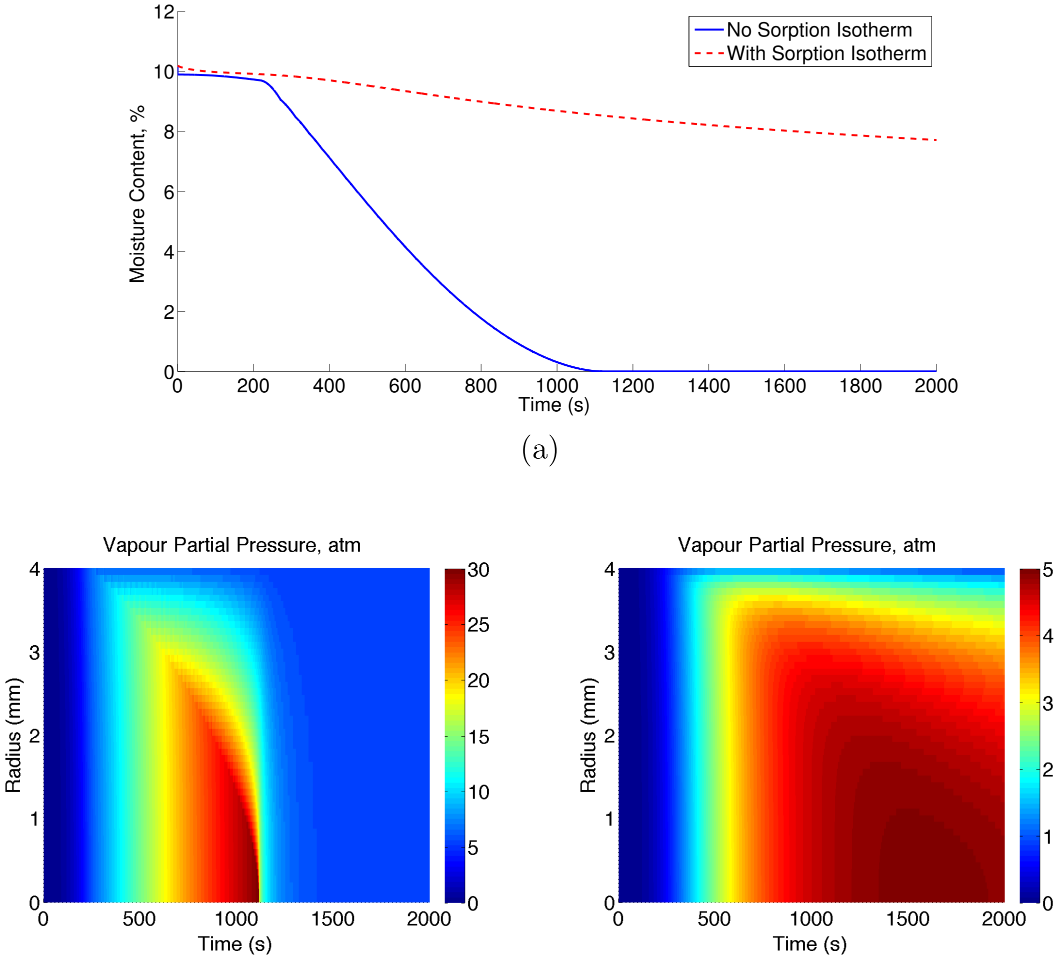

(a)

(b)

(c)

Figure 4.2: (a) Comparison of the moisture loss predicted by the Multiphase Model (3.1)-(3.8) shown in Chapter 3 with and without the incorporation of the sorption isotherm defined in (4.37). Bottom: Vapour pressure $p_v(r,t)$ as predicted by the Multiphase Model (b) without the sorption isotherm and (c) with the sorption isotherm. All parameters are the same as those used in Chapter 3, with C_1 and C_2 in (4.37) being given in [9] and $T_\infty = 230°\text{C}$.

we obtain the following Region i PDE system:

$$\frac{\partial}{\partial t}\left[\frac{(1+\mathscr{T})(1-\sigma S)P_v^*(T,S)}{1+\mathscr{T}T}\right] = -\frac{1}{\delta}\frac{\partial S}{\partial t} + \nabla\cdot\left[\frac{(1+\mathscr{T})P_v^*(T,S)\nabla P_v^*(T,S)}{1+\mathscr{T}T}\right], \tag{4.50}$$

$$\frac{\partial T}{\partial t} + \mathcal{A}_1\frac{\partial}{\partial t}\left[S(1+\mathscr{T}T)\right] = \mathcal{A}_2\frac{\partial S}{\partial t} + \mathcal{A}_3\nabla\cdot\left[(1+\mathcal{A}_4 S)\nabla T\right]. \tag{4.51}$$

Unlike in Chapter 3, further parameter simplifications, such as allowing $\delta \ll 1$, do not allow for further analytical results. Indeed, our leading order equation for (4.50) gives us $\frac{\partial S}{\partial t} = 0$, which in turn implies that $S \equiv 1$; however, substituting this into (4.49) and (4.45) forces T to assume two different constant values. Alternatively, we could rescale time by allowing $\tau = \delta t$; our leading-order equations for (4.51) become

$$\frac{\partial}{\partial \tau}\left[T + (\mathcal{A}_1 - \mathcal{A}_2)S + \mathcal{A}_1\mathscr{T}ST\right] = 0, \tag{4.52}$$

which, after integrating and imposing (4.48), gives

$$S = \frac{\mathcal{A}_1 - \mathcal{A}_2 - T}{\mathcal{A}_1(1+\mathscr{T}T) - \mathcal{A}_2}. \tag{4.53}$$

Again, this requires T to satisfy two conflicting boundary conditions; therefore, we conclude that we must solve (4.50) and (4.51) together, which is only possible via numerical methods.

Finally, we note that the isothermal simplification, discussed in Section 3.3, does not provide any additional simplifications. Indeed, by setting $P = P_v^*(1,S)$, we must solve the following nonlinear PDE in S for Region i:

$$\frac{\partial}{\partial t}\left[(1-\sigma S)P_v^*(1,S) + \frac{S}{\delta}\right] = \nabla\cdot\left[P_v^*(1,S)\nabla P_v^*(1,S)\right], \tag{4.54}$$

$$\nabla S\cdot\mathbf{n}\big|_{r=0} = 0, \tag{4.55}$$

$$S\big|_{r=1} = \left[\frac{1}{C_3 P_a} - \frac{1}{C_3}\right]^{-\frac{1}{C_1}}. \tag{4.56}$$

While one could rescale time to have $\tau = \delta t$ and examine the leading-order behaviour for $\delta \ll 1$, an explicit solution is still not readily available. Therefore, we conclude that while the vapour pressure is, to leading order in ϵ, aligned with the sorption isotherm, the resulting non-linear PDEs cannot be solved analytically.

Gas Permeability k_g, m^2	Maximal Vapour pressure $P_{v,\max}$, atm
10^{-20}	5.0839
10^{-19}	5.0604
10^{-18}	4.2938
10^{-17}	2.4268
10^{-16}	1.0352
10^{-15}	0.3826
10^{-14}	0.1308
10^{-13}	0.0427
10^{-12}	0.0138

Table 4.1: Maximum vapour pressure experienced in the modified Multiphase Model for various gas permeabilities.

4.3.3 Relating the Maximum Vapour Pressure to Evaporation Parameters

The modified Multiphase Model predicts that the coffee bean will dry at a significantly slower speed than the original model stated in Chapter 3. However, this could be compensated for by increasing the gas permeability (k_g) to a more realistic value for similar organic compounds, such as wood. Such a change in parameters would cause the maximal vapour pressure observed in the coffee bean, denoted as $P_{v,\max}$, to decrease (as seen in Table 4.1). These data are also presented in Figure 4.3, where we can see that $\log(P_{v,\max})$ is approximately linear in $\log(k_g)$ away from zero and has a slope of approximately $-\frac{1}{2}$, which indicates that $P_{v,\max} = O(k_g^{-1/2})$ for $k_g \gg 1$. However, we also note that $P_{v,\max}$ cannot exceed $p_v^*(T_\infty, \phi, \sigma)$ if we assume that condensation does not occur. Therefore, we infer the approximate relationship

$$P_{v,\max} = \frac{P_v^*(T_\infty, \sigma)}{\sqrt{\frac{k_g}{k_0} + 1}}, \tag{4.57}$$

where k_0 is chosen to fit the data.

If we take the view that the value of k_g should be appropriate for permeabilities in wood, we would choose k_0 so that the curve intersects the data when $k_g = 10^{-12}$ m^2, which implies that $k_0 \approx 6.84 \times 10^{-18}$ m^2. As we can see in Figure 4.3, this approximate relationship between $P_{v,\max}$ and k_g agrees well with the data in the physically relevant parameter range. We note, however, that when using this value of k_g, the effect of sorption isotherm implies that the maximal vapour pressure, as shown in Table 4.1, is only a fraction of an atmosphere above the external environment. As we will discuss in Chapters 5 and 6, knowing the maximum gas pressure in the coffee bean is crucial to understanding further aspects of roasting, such as First Crack.

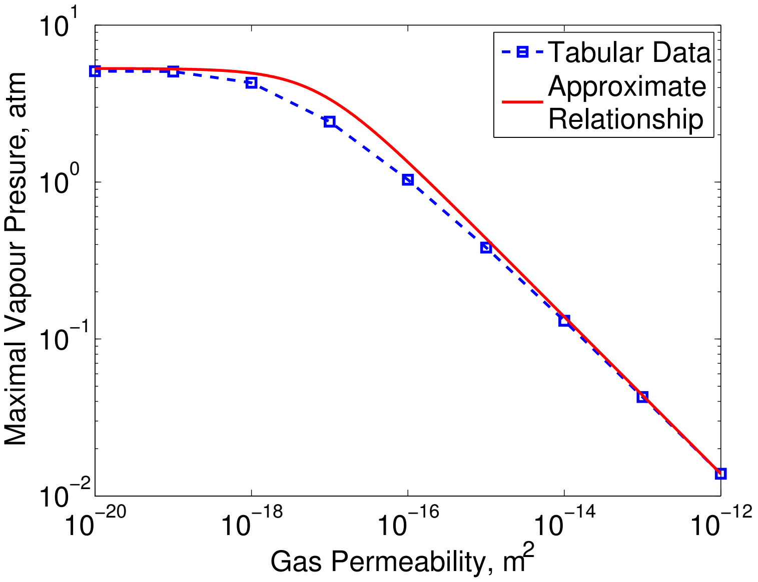

Figure 4.3: Log-log plot of $P_{v,\max}$ versus k_g. The tabular data are shown in Table 4.1 and the approximate relationship refers to Equation (4.57), with $k_0 \approx 6.84 \times 10^{-18}$ m^2.

4.4 Discussion

In this chapter, we have incorporated modified evaporation rates to improve existing mathematical models of roasting coffee beans. Motivated by the fact that Langmuir's equation, described in [31], may not be the best representation of water evaporation from a coffee bean, a more general class of separable evaporation rates was also examined. By continuing to assume a constant roasting temperature to simplify the Multiphase Model, it was shown that the explicit form of the evaporation rate only affects the dynamics within the transition layer: in particular, how the moisture content S transitions from its initial moisture to negligible quantities.

However, we also note that separable evaporation rates, such as those presented in Chapter 2, did not reflect moisture transport in a roasting bean with sufficient accuracy. Hence, a different approach was required to model the evaporation rate inside a roasting bean. We therefore presented a model of evaporation of the water in a roasting coffee bean via a sorption isotherm, which is often employed for evaporation mechanisms inside drying organic materials. This evaporation rate is affected by deviation of vapour pressure from an equilibrium vapour pressure of the bound water and accounts for the large number of possible binding sites in organic materials.

Numerical solutions of the Multiphase Model with the incorporated sorption isotherm indicate a number of differences between the Multiphase Model that uses the

Langmuir equation as an evaporation rate. Firstly, we note that, to leading order, the vapour pressure never deviates from its sorption isotherm. This is because the sorption isotherm is a function of saturation, which allows the external vapour pressure boundary condition to be resolved by modifying the water saturation accordingly. In consequence, there is no "drying front" or secondary dry region observed when the sorption isotherm is incorporated into the Multiphase Model.

We also determined that the incorporation of the sorption isotherm significantly increases the time for a coffee bean to dry out, while decreasing the maximal vapour pressure experienced in the bean. When compared to numerical results, we determined that the bean's maximal vapour pressure approximately obeys a reciprocal square-root power law for gas permeabilities in the range of similar organic materials to wood. However, for much smaller values of gas permeabilities, the maximal vapour pressure approaches the maximal sorption vapour pressure, i.e. the sorption isotherm pressure at roasting temperature and initial water saturation. While this approximate relationship is simplistic, it allows us to infer what magnitudes of vapour pressures can be expected for a range of gas permeabilities, which is crucial in determining chemical reaction rates and additional features of a roasting coffee bean that will be discussed in the following chapters. Specifically, this range of gas permeabilities will be further considered when we incorporate additional groups of chemical reactions into the multiphase models presented in Chapter 5.

Chapter 5

The Influence of Distributed Chemical Reaction Groups in a Multiphase Coffee Bean Roasting Model

5.1 Introduction

This chapter is mainly comprised of results shown in [14]. Here, we incorporate modified evaporation rates and chemical reaction groups to improve previously discussed mathematical models of roasting coffee beans. We model the phase change from liquid to vapour water within the bean during roasting using first-order Arrhenius-like global reactions, and for other components of the bean, we consider a three-component solid phase model which includes sucrose, reducing sugars, and other organic compounds, which allows for porosity of the solid matrix to vary during the roasting process. We non-dimensionalise and then solve the multiphase model numerically, comparing the simulations with data we have collected through full bean and chopped bean experiments.

We demonstrate that numerical solutions of the enhanced multiphase model with global water reactions and three-component solid phase reactions agree with experimental data for the average moisture content in whole beans and small chunks of bean, but that the data allows for a range to possible parameter values. We discuss other experimental data that might be collected to more firmly determine the parameters and hence the model behaviour more generally. The indeterminacy of the parameters ensures that the additional effects included in the model will enable better understanding the coffee bean roasting process.

In this chapter, we shall extend the Multiphase Model in Chapter 2 in a number of ways. Motivated in part by literature on timber drying (e.g. [44]) we consider more detailed mechanisms for the evaporation rate within a coffee bean. Specifically, we view evaporation as a multistep process including accounting for a distribution of chemical reactions. Furthermore, we incorporate water activity ([29, 40]) into our evaporation model to account for how water changes phase from liquid to vapour within a coffee bean structure. To account for the many chemical reactions present within the roasting bean, we also include a simplified sugar chemical pathway model representative of key reaction groups that occur during the roasting process. Finally, a spherical "shell" geometry is used to provide a more realistic representation of the geometry of a coffee bean. The resulting model is then non-dimensionalised and solved numerically.

5.2 The Chopped Green Coffee Bean Experiment

To further validate the model parameter values, we undertook the chopped green coffee bean experiment proposed in Chapter 2. Specifically, this experiment explores the question: if we coarsely break up green coffee beans prior to roasting, how much faster does the water vapour leave the bean? To examine this behaviour, washed Arabica Peru coffee beans were ground on a NETZSCH Condux mill set with the widest possible gap settings between rotor and stator. The ground beans obtained were sieved through 2 metal mesh sieves placed above each other, with mesh sizes of 2.5mm and 1.4mm respectively. Hence, we can infer that the radius of a coffee bean chunk that we consider is between 0.7mm and 1.3mm.

Roasting experiments were carried out on a Probat BRZ2 electric drum laboratory roaster in batches of 100g and roasted at approximately 230°C for 180-300 seconds. The product temperature, measured by the fixed probe built in the roaster drum, was recorded throughout the roast. The batch of chopped beans was removed at regular intervals during roasting, cooled in ambient air and immediately placed in a sealed container. Residual bean moisture was measured gravimetrically: a 10g sample of roasted whole beans was placed in an oven set at 103-105°C for 16 hours and allowed to cool down in a desiccator. To provide a control for comparison, whole green beans of approximately 4mm average radius were also roasted at 230°C and their moisture content recorded at regular intervals (see Table 5.1).

Time, s	Moisture Content (Whole Bean), %	Moisture Content (Chopped Bean), %
0	10.2	10.2
60	9.05	6.37
120	7.13	3.18
180	5.72	1.45
210	5.07	1.22
240	2.27	-
270	1.62	-

Table 5.1: Moisture Content of whole coffee beans and chopped coffee beans during a 230°C roast. Experimental data courtesy of Z. Akram.

As these bean chunks look roughly spherical, we consider predicting their drying behaviour using the Multiphase Model shown in Chapter 3 on a spherical geometry with radius $L = 0.7$mm while keeping all other parameter values unchanged. Results of this experiment are shown Figure 5.1, where we observe that the moisture loss predicted by the Multiphase Model significantly disagrees with the experimental data. We might expect that because the behaviour is primarily determined by a diffusive process, along with the effective length scale of the model being decreased by a factor of between $\frac{0.7}{4}$ and $\frac{1.3}{4}$, the drying time of the bean chunk will be between $\left(\frac{0.7}{4}\right)^2 \approx 3.1\%$ and $\left(\frac{1.3}{4}\right)^2 \approx 11\%$ of the time for a whole bean. However, the data in Figure 5.1 shows that, when drying chunks, they take roughly 65% of the whole bean drying time. Hence, this Multiphase Model with the parameters chosen to fit whole bean behaviour does not translate well with a different length scale.

5.3 Chemical Reaction Groups in Roasting Coffee Beans

To gain a better fit between the model predictions and experimental data over a wide range of conditions, the model in Chapter 2 needed to be extended. Motivated by the existing literature on timber drying (e.g. [44]), the model of evaporation was seen as the critical element to describe accurately. A simplistic view of the evaporation process is the following. Firstly, there is water in the cells which is not accessible until the cell structure degrades (called the "yellowing stage" in roasting). When the cell degrades, this cell water joins the water already bound in the cellular matrix of the bean. This bound water then slowly evaporates to become water vapour. How quickly it evaporates is determined by the strength of the chemical bond between the water and the matrix, as well as the surrounding water vapour pressure. One of the difficulties in deriving such a model is that there are a myriad of possible compo-

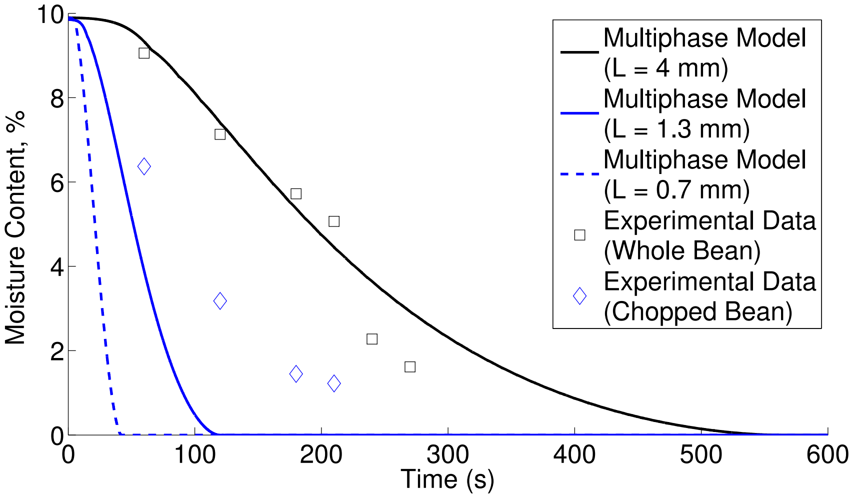

Figure 5.1: Comparison of the average moisture content in a bean chunk versus a whole bean during a 230°C roast. The solid lines correspond to the average moisture loss determined by the Multiphase Model (3.1)-(3.8) presented in Chapter 3, and the markers correspond to experimental data seen in Table 5.1. Aside from the effective radius L and roast temperature $T_\infty = 230°\text{C}$, all other parameters are the same as those used in Chapter 2.

nents to be degraded in cells and a similar large number of compounds that water might bind to. This model has a few parameters in it and we shall present ideas from pyrolysis of coal, the Distributed Activation Energy Method (DAEM) discussed in [46], to indicate how these parameters might be connected to independently measurable quantities. Hence, the resulting modelling of evaporation replaces the simple Langmuir evaporation equation given in Chapter 2.

5.3.1 Modelling the Degradation of Cells

We now consider how to model the degradation of the cells and how the water in the cells then moves into bound water. We will assume that the cell water volume fraction is given by $\phi S - w_b - w_n$, where ϕ is the porosity, S is the water saturation, and $w_b + w_n$ is the total bound water fraction. The bound water will be separated into w_b, denoting the water that can be evaporated, and w_n, denoting the fraction that cannot be removed. A simple model of degradation of the cells is given by

$$\frac{\partial}{\partial t}\left[\phi S - w_b - w_n\right] = -(\phi S - w_b - w_n)\mathcal{R}_1(T), \tag{5.1}$$

where $\mathcal{R}_1(T)$ is the effective rate that cell water becomes bound water due to degradation of the cell. We now discuss how this effective rate might be determined from degradation rates for the many chemical components of a cell.

5.3.2 Modelling Degradation using a Distribution of Chemical Reactions

To motivate the framework of a distributed chemical reaction group, we first consider a single first-order reaction $A \to B$ with reaction rate $\mathscr{K}$, where A is a particular cell component and B is the product of its degradation. If we assume a first-order Arrhenius reaction model [30], we obtain the system of differential equations

$$\frac{\partial \phi_A}{\partial t} = -\mathscr{K}\phi_A \exp\left(-\frac{E}{RT}\right), \tag{5.2}$$

$$\frac{\partial \phi_B}{\partial t} = \frac{\rho_A}{\rho_B}\mathscr{K}\phi_A \exp\left(-\frac{E}{RT}\right), \tag{5.3}$$

where ϕ_A and ϕ_B are the volumetric fractions of chemicals A and B respectively, while ρ_A and ρ_B are the densities of chemicals A and B respectively. This is an appropriate form to model reaction kinetics for a single chemical reaction and can readily be extended to many components by writing a differential equation for each. However, when modelling a very large group of chemical reactions, it may be appropriate to make a simple model by assuming some distribution of chemical reactions. For simplicity, we will assume that all chemical reactions in the group are independent and that they are first-order governed by Arrhenius-like kinetics. We then model a group of chemical reactions by assuming each component has a different activation energy E and reaction pre-factor $\mathscr{K}$ so that they can be described by a density distribution $f(E)$ over activation energies. This approach is motivated from the Distributed Activation Energy Method (DAEM), whose original application was in modelling various chemical reactions in the pyrolysis of coal. Mathematically, this distributed chemical reaction model takes the form of a single reaction for the group with a *global* reaction rate, $\mathcal{R}(T)$, given by

$$\mathcal{R}(T) = \int_0^\infty \mathscr{K}(E) \exp\left(-\frac{E}{RT}\right) f(E) \mathrm{d}E. \tag{5.4}$$

As a specific example, we can assume that the pre-factors are constant and independent of the activation energy (i.e. $\mathscr{K}(E) \equiv \mathscr{K}$) and that the distribution of activation energies of the chemical reactions is Gaussian with a large mean μ_E and standard deviation σ_E:

$$f(E) = \frac{1}{\sigma_E\sqrt{2\pi}} \exp\left(-\frac{(E-\mu_E)^2}{2\sigma_E^2}\right). \tag{5.5}$$

Thus, if we now view the process $a \to b$ as a group of chemical reactions, we would model this group of reactions as

$$\frac{\partial \phi_a}{\partial t} = -\phi_a \mathcal{R}(T), \tag{5.6}$$

$$\frac{\partial \phi_b}{\partial t} = \frac{\rho_a}{\rho_b}\phi_a \mathcal{R}(T), \tag{5.7}$$

where

$$\begin{aligned} \mathcal{R}(T) &= \frac{\mathscr{K}}{\sigma_E\sqrt{2\pi}} \int_0^\infty \exp\left(-\frac{E}{RT} - \frac{(E-\mu_E)^2}{2\sigma_E^2}\right) dE \\ &= \frac{\mathscr{K}}{2} \exp\left(\frac{\sigma_E^2}{2R^2T^2} - \frac{\mu_E}{RT}\right) \operatorname{erfc}\left(\frac{\sigma_E}{\sqrt{2}RT} - \frac{\mu_E}{\sqrt{2}\sigma_E}\right); \end{aligned} \tag{5.8}$$

here, ϕ_a and ϕ_b are the volumetric fractions of chemical groups a and b, respectively.

5.3.3 Approximation of the Global Reaction Rate

While the global reaction rate in (5.8) better represents more complex groups of chemical reactions, the explicit formula for $\mathcal{R}(T)$ shown in (5.8) is complicated to work with. We therefore consider a simplified version of $\mathcal{R}(T)$ given by

$$\mathcal{R}(T) \approx \tilde{\mathcal{R}}(T) := \mathcal{R}(T_\infty) \exp\left[\log\left(\frac{\mathcal{R}(T^*)}{\mathcal{R}(T_\infty)}\right)\left(\frac{T_\infty - T}{T_\infty - T^*}\right)\right], \tag{5.9}$$

where T^* is chosen so that $\max_{T\in[T_0,T_\infty]}\left|\tilde{\mathcal{R}}(T) - \mathcal{R}(T)\right|$ is minimized, i.e. the maximal absolute error between the global reaction rate and its approximating function is minimal. This exponential approximation is appropriate as we are in the parameter range where $\mu_E \gg \sigma_E$, implying that $\mathcal{R}(T)$ is always concave up in the specified temperature range. Equivalently, this exponential behaviour is valid when the Arrhenius dependence can readily be approximated by an exponential, as is valid for most roasting conditions.

As an example, we consider the hydrolysis of surcrose to glucose and fructose, which has parameters $\mu_E = 109200$ and $\mathscr{K} = 2.0 \times 10^{14}$ [55]. We anticipate that the standard deviation of this global reaction rate is small, so we choose $\sigma_E = 1000$. As we can see in Figure 5.2, the fit exponential approximation agrees well with $\mathcal{R}(T)$ on

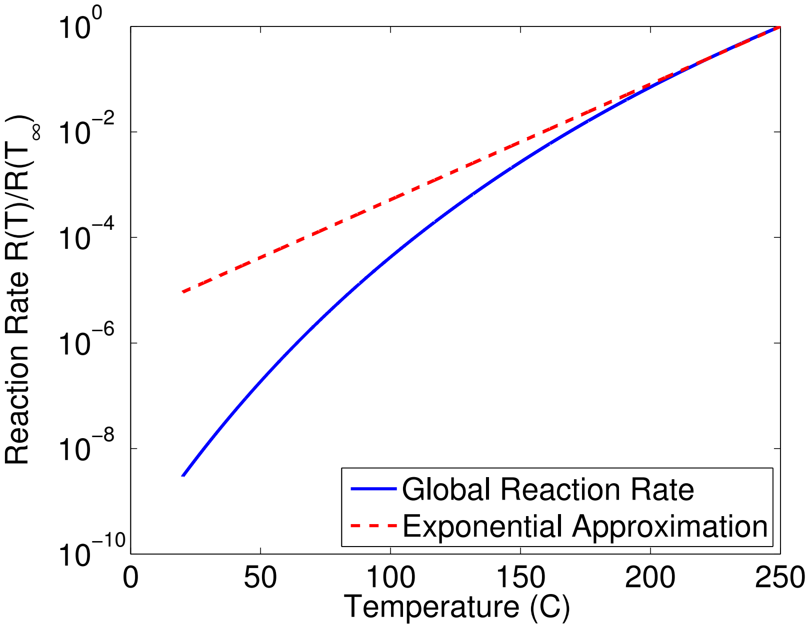

Figure 5.2: Comparison of the hydrolysis of sucrose modelled using the global reaction rate $\frac{\mathcal{R}(T)}{\mathcal{R}(T_\infty)}$, defined in (5.8), and its exponential approximation $\frac{\tilde{\mathcal{R}}(T)}{\mathcal{R}(T_\infty)}$, defined in (5.9).

the temperature range of 20°C - 250°C.

Using these ideas, we assume that the global reaction rate can be approximated by

$$\mathcal{R}(T) \approx \alpha \exp\left(-\frac{\beta(T_\infty - T)}{T_\infty - T_0}\right), \tag{5.10}$$

where $\alpha > 0$ and $\beta > 0$ are parameters to be determined experimentally. To help identify a possible realistic range for these parameters, we note that for the sucrose hydrolysis example, when $T_0 = 20$°C and $T_\infty = 250$°C, this yields $\alpha \approx 2560$ s^{-1}, $\beta \approx 11.6$.

5.3.4 Modelling the Evaporation of Bound Water

The second process for the liquid phase is evaporation of the bound water into water vapour. Having described the behaviour of a single type of binding site for the water in Chapter 4, we now need to write down the effective equations when there is a distribution of sites with different activation energies. We find there are two elements that appear in the model when applying DAEM concepts: an effective reaction rate $\mathcal{R}_2(T)$ for the evaporation, and the previously mentioned sorption isotherm p_v^*. Using the ideas from Chapter 4, and recalling that bound water is also created from cell water by cell degeneration as discussed previously, the model for bound water becomes

$$\frac{\partial w_b}{\partial t} = (\phi S - w_b - w_n)\mathcal{R}_1(T) - w_b\left[p_v - p_v^*(T,\phi,S)\right]\mathcal{R}_2(T). \tag{5.11}$$

Note that by combining (5.11) with (5.1), we can derive the conservation equation for the fraction of the entire liquid phase ϕS:

$$\frac{\partial}{\partial t}[\phi S] = -w_b\left[p_v - p_v^*(T,\phi,S)\right]\mathcal{R}_2(T). \tag{5.12}$$

A summary of the parameter values used for the effective reaction rates of degradation and evaporation is shown in Table 5.2.

5.4 A Three-Component Solid Phase Model (the Sugar Pathway Model)

It is crucial for understanding coffee roasting to know how sucrose and other sugars in the bean react to produce flavour compounds. In particular, we will model the main sugar reactions via a simplified chemical reaction pathway that is motivated by the reactions proposed by [58]. To account for important effects of these reactions, we will also need to incorporate variable porosity, additional gas species, and some effective thermal properties in the model. With appropriate boundary and initial conditions, these conservation equations will be referred to as the Sugar Pathway Model.

5.4.1 A Simplified Sugar Pathway and the Inclusion of Variable Porosity

For simplicity, and motivated by the reactions described in [58], we consider the solid phase of the bean to consist of just three main chemical reaction groups. We take these groups to be sucrose (with volume fraction ϕ_1), reducing sugars (with volume fraction ϕ_2), and other organic compounds (with volume fraction ϕ_3). If we now recall that the solid volume fraction is denoted by $1-\phi$, we have that

$$1 - \phi = \sum_{i=1}^{3} \phi_i, \tag{5.13}$$

and hence the solid phase of the bean will have a volume fraction that varies in time and space as roasting occurs.

We will consider reactions between the three groups using a simplified sugar pathway model. Firstly, sucrose hydrolyses into reducing sugars within the biological cells (at an effective reaction rate $\mathcal{R}_3(T)$). These reducing sugars then have two main reactions that they can undertake. They either react to form CO_2 gas and other organic solids via the Maillard reactions (with effective reaction rate $\mathcal{R}_4(T)$ and stoichiometric ratios of the products χ_1, χ_2 respectively), or they react to form CO_2 and other organic solids via caramelization (with an effective reaction rate $\mathcal{R}_5(T)$ and stoichiometric ratios of the products χ_3, $(1-\chi_1-\chi_2-\chi_3)$ respectively).

The Maillard reaction [58] is a group of chemical reactions that describe the browning of various foodstuffs, from bread to malted barley to roasted coffee beans. These reactions involve amino acids combining with sugars to produce pyrazines, carbonyls, furrans, and other organic compounds [34]. Contrastingly, the caramelization reactions are simply the pyrolysis of sugars and are thus viewed as entirely different reaction group. Nevertheless, the Maillard reaction relies on the presence of sugars to produce the aforementioned products of amino acids and therefore is included in this simplified sugar pathway.

Another important difference between the Maillard reactions and the caramelization reactions is that the Maillard reactions effectively act as an endothermic reaction group [34], whereas the caramelization reactions behave as an exothermic reaction group [12]. Additionally, we assume that hydrolysis of sucrose can only occur if cell water is present. Using these simplified sugar pathway reactions, the conservation equations for the three solid phases are

$$\frac{\partial \phi_1}{\partial t} = -\phi_1(\phi S - w_b - w_n)\mathcal{R}_3(T), \tag{5.14}$$

$$\frac{\partial \phi_2}{\partial t} = \frac{\rho_1}{\rho_2}\phi_1(\phi S - w_b - w_n)\mathcal{R}_3(T) - \phi_2[\mathcal{R}_4(T) + \mathcal{R}_5(T)], \tag{5.15}$$

$$\frac{\partial \phi_3}{\partial t} = \frac{\rho_2}{\rho_3}\phi_2[\chi_2\mathcal{R}_4(T) + (1-\chi_1-\chi_2-\chi_3)\mathcal{R}_5(T)]. \tag{5.16}$$

Note that using (5.13), we can combine these three equations to give a conservation equation of the entire solid phase given by

$$\begin{aligned}\frac{\partial \phi}{\partial t} = &\left(1-\frac{\rho_1}{\rho_2}\right)\phi_1(\phi S - w_b - w_n)\mathcal{R}_3(T) \\ &+ \phi_2\left[\left(1-\frac{\rho_2}{\rho_3}\chi_2\right)\mathcal{R}_4(T) + \left(1-\frac{\rho_2}{\rho_3}(1-\chi_1-\chi_2-\chi_3)\right)\mathcal{R}_5(T)\right].\end{aligned} \tag{5.17}$$

A summary of the parameter values used for three chemical reaction groups in the

Reaction Name and Number ($\mathcal{R}_i(T)$)	Global Reaction Rate (α_i)	Exponential Factor (β_i)	Enthalpy, J (λ_i)
$\mathcal{R}_1(T)$: Cell Degradation	0.2	7.5	-1×10^5
$\mathcal{R}_2(T)$: Evaporation	1	7	-2.3×10^6
$\mathcal{R}_3(T)$: Sucrose Hydrolysis	10	11.4	-4.3×10^4
$\mathcal{R}_4(T)$: Maillard Reactions	0.01	10	-6.1×10^5
$\mathcal{R}_5(T)$: Caramelization	1×10^{-3}	10	1×10^5

Table 5.2: Parameters used in the global reaction rates $\mathcal{R}_i(T)$.

sugar pathway is shown in Table 5.2.

5.4.2 Incorporating Additional Gas Species

Some of the chemical reactions in the Sugar Pathway Model also produce large quantities of CO_2 gas. Hence, we need to not only to consider water vapour transport but also include the effects of CO_2 in the model. We will also need to consider other gases; for example, when a bean is put into the roaster, it is typically full of normal atmospheric gases with a small amount of vapour and no CO_2. Thus, we will lump all gases, other than water vapour and CO_2, as a species that we call “air”. We assume that the total gas pressure within a coffee bean can be represented as the sum of three partial gas pressures: air (p_a), CO_2 (p_c), and water vapour (p_v).

Transport of the gases in the bean has previously been assumed to be dominated by a bulk motion determined by a Darcy flow, driven by the total pressure gradient. The bulk motion is described through a permeability, which accounts for flow in nanopores that interconnect the pores in the structure. We note that, when fitted to data, the permeabilities required may be very small and perhaps non-physical. A second possible transport mechanism is to assume that the pores are completely sealed (a closed pore structure), so that transport is by adsorption into the structure and diffusion through the structure. A simple model of such a mechanism is an effective diffusion with flow driven by the partial pressure of the relevant gas. Since the mathematical form of these two mechanisms is very similar, we will adopt the notation of the Darcy flow but note that if permeabilities need to be very small, we might infer that the bean has a closed pore structure and diffusion dominates transport. We have not yet explored this diffusion mechanism in great detail.

We now consider the transport equations for the three gases. Firstly, the air does not participate in any reactions and hence the conservation equation of air implies that

$$\frac{\partial}{\partial t}\left[\frac{p_a\phi(1-S)}{T}\right] = \nabla\cdot\left[\frac{p_a k_g}{\mu T}\nabla\left(p_a+p_c+p_v\right)\right]. \tag{5.18}$$

The CO_2 gas is produced in both the caramelization and Maillard reactions and hence, conservation of this species requires that

$$\frac{\partial}{\partial t}\left[\frac{p_c\phi(1-S)}{T}\right] = \nabla\cdot\left[\frac{p_c k_g}{\mu T}\nabla\left(p_a+p_c+p_v\right)\right] + \frac{R\rho_2}{m_c}\phi_2[\chi_1\mathcal{R}_4(T)+\chi_3\mathcal{R}_5(T)]. \tag{5.19}$$

Finally, for the water vapour phase, we assume that all water lost from the liquid phase becomes water vapour, so that

$$\frac{\partial}{\partial t}\left[\frac{p_v\phi(1-S)}{T}\right] = \nabla\cdot\left[\frac{p_v k_g}{\mu T}\nabla\left(p_a+p_c+p_v\right)\right] - \frac{R\rho_w}{m_v}\frac{\partial}{\partial t}[\phi S]. \tag{5.20}$$

5.4.3 Accounting for Varying Gas Permeability

We have assumed that the gases are driven through narrow pores and described using the permeability k_g. The pores in the structure are changing as the porosity varies and are constricted due to any water that is in them. Hence, the permeability needs to be modelled to account for these variations. The fundamental idea is that below a critical amount of gas, the gas phase sits in disconnected pockets and hence cannot move ($k_g = 0$) and that above this critical amount, the permeability increases as the amount of gas increases. Motivated by [61], we assume that the permeability therefore depends only on the liquid volume fraction and a very simple model of this is

$$k_g = k_{g0}\max\left\{1-\frac{\phi S}{\eta},\ 0\right\}, \tag{5.21}$$

where k_{g0} is the intrinsic gas permeability when there is no water present, and η is a physical parameter between 0 and 1 that represents the threshold liquid fraction in the pore for gas to permeate. As this simple model originates from the study of moisture transport in bread baking, it seems reasonable that moisture transport in other organic materials (such as coffee beans) can also be described by this model.

5.4.4 Effective Thermal Properties

When considering the thermal energy in the bean, we must account for the heat released by the various chemical reaction groups that we have considered. In general, the heat released by each of the individual parts of any reaction group also follows a distribution across activation energies E. However, we will assume that the heat release is independent of E and is constant (denoted by the positive constants λ_i). We note that all reaction groups are assumed to be net-endothermic [34] except the caramelization reaction group [12], which we assume to be net-exothermic (and account for this with a minus sign in the equations). Finally, as was done in Chapter 2, we will assume that at any point in space, all the different volumetric fractions are at the same temperature and that heat transport due to gas motion is negligible. Conservation of thermal energy can then be summarised by

$$\begin{aligned}\frac{\partial}{\partial t}\left[\rho_{\text{eff}} C_{p,\text{eff}} T\right] = &- \rho_w \left\{\lambda_1 w_b \left[p_v - p_v^*(T, \phi S)\right] \mathcal{R}_1(T) + \lambda_2(\phi S - w_b - w_n)\mathcal{R}_2(T)\right\} \\ &- \lambda_3 \rho_1 \phi_1 (\phi S - w_b - w_n)\mathcal{R}_3(T) - \rho_2\phi_2[\lambda_4\mathcal{R}_4(T) - \lambda_5\mathcal{R}_5(T)] \\ &+ \nabla \cdot \left[K_{\text{eff}} \nabla T\right],\end{aligned} \tag{5.22}$$

where $\rho_{\text{eff}}, C_{p,\text{eff}}$, and K_{eff} are the effective thermal properties of the multiphase material.

Because the gas phase stores very little heat, we will neglect the change in enthalpy provided by the gas phase, and define the effective thermal heat capacity by

$$\rho_{\text{eff}} C_{p,\text{eff}} = \rho_w C_{p,w} \phi S + \sum_{i=1}^{3} \phi_i \rho_i C_{p,i}. \tag{5.23}$$

For the effective thermal conductivity in the multiphase bean, we use the simple form suggested in the literature for a randomly structured material (see, e.g., [59]) and determined by the harmonic average of the volume averaged thermal conductivities of the individual phases:

$$K_{\text{eff}} = \left(\frac{\phi S}{K_w} + \frac{\phi(1 - S)}{K_g} + \sum_{i=1}^{3} \frac{\phi_i}{K_i}\right)^{-1}, \tag{5.24}$$

where K_g is the thermal conductivity of the gas phase. This harmonic average was not used in previous models, such as in Chapter 2, as the effects of a randomly structured material had not been considered. To determine K_g, one must consider the sum of the thermal conductivities of each gas, multiplied by their respective molar fraction. Noting that, because all the gases are locally at the same temperature, the molar fraction of each gas is identical to the fraction of each partial pressure, which yields

$$K_g = \frac{K_a p_a + K_c p_c + K_v p_v}{p_a + p_c + p_v}. \tag{5.25}$$

This modelling is different from the approach taken in Chapter 2, where K_{eff} was taken to be the arithmetic sum of the volume averaged thermal conductivities in each phase.

5.4.5 The Effective Length Scale of a Whole Coffee Bean

To better understand the length scale issues discussed in Section 5.2, we will consider a different geometry than that used by [13] and Chapters 2 and 3 to represent a whole bean. This different geometry is motivated from the SEM image of the cross-section of a coffee bean shown in Figure 5.3. We conclude that a whole coffee bean can be quite well represented as a spherical "shell" of inner radius aL, where $0 < a < 1$, and outer radius L as shown in Figure 5.3. We note that a half-spherical shell may be a more realistic representation of a coffee bean, but such details would break the spherical symmetry of the problem and hence preclude a simple one-dimensional analysis. For the bean chunks, we can take a simple sphere of radius r_{chunk} as the geometry.

We need to choose two constitutive equations in order to relate a and L to the effective radius of the bean r_e. Firstly, we assume that this spherical shell mapping should volume-preserving. Secondly, we impose that the average square-distance from any point in the bean to the boundary of the bean is preserved under the mapping. These two constitutive equations provide the framework for determining a and L; in the context of a hemispherical coffee bean with effective radius r_e, this yields the equations

$$\frac{2\pi}{3} r_e^3 = \frac{4\pi}{3} L^3(1 - a^3), \quad L(1 - a) = \gamma r_e, \tag{5.26}$$

implying that

$$a = \frac{1 + \gamma^3 - \sqrt{3\gamma^3(2 - \gamma^3)}}{1 - 2\gamma^3}, \quad L = \frac{\gamma r_e}{(1 - a)}. \tag{5.27}$$

The constant γ can be then determined directly from these or inferred from simple physical considerations: for example, using the fact that the drying time of coffee chunks in the experiment discussed in Section 5.2 takes roughly 65% of the original whole bean drying time. Using this fact, and that the timescale of diffusive mechanisms scales with the square ratio of length scales, this gives us that

$$\left(\frac{2r_{chunk}}{L(1 - a)}\right)^2 = \left(\frac{2r_{chunk}}{\gamma r_e}\right)^2 = 0.65. \tag{5.28}$$

By using the effective radii listed in Section 5.2, i.e. $r_e = 4$mm and $r_{chunk} = 0.7$mm,

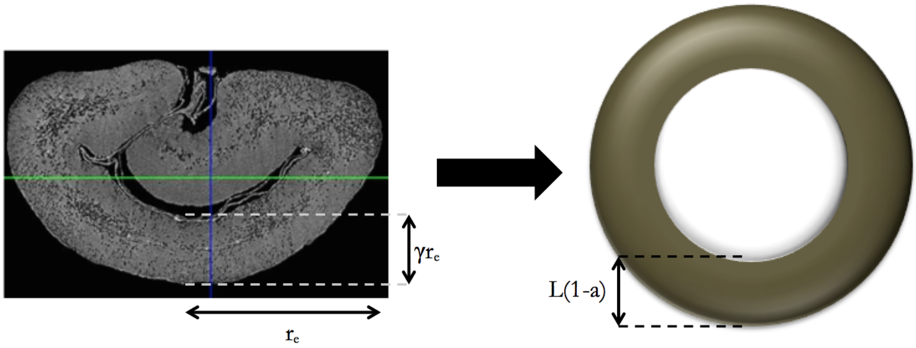

Figure 5.3: SEM coffee bean, with measured radius r_e and thickness γr_e, and the idealised geometry of a spherical shell of outer radius L and inner radius aL. The SEM image (left) is adapted from Chapter 2.

this implies that

$$\gamma = \frac{2r_{chunk}}{r_e\sqrt{0.65}} \approx 0.43. \tag{5.29}$$

Indeed, with reference to Figure 5.3, it seems reasonable that the slab of bean material is approximately 43% of the effective radius of the whole bean, implying that $a \approx 0.47$, $L \approx 0.82r_e$.

5.4.6 Initial and Boundary Conditions

Finally, we consider the initial and boundary conditions for the model. We assume, because the beans have been sitting in storage elsewhere for a long time, that they are filled with air with water vapour in equilibrium and no CO_2 with a total pressure imposed by the surrounding atmosphere. For all geometries, we therefore impose uniform initial conditions on all variables with

$$\begin{gathered}\phi_1(r,0) = \phi_{10}, \quad \phi_2(r,0) = 0, \quad \phi(r,0) = \phi_0, \quad w_b(r,0) = w_{b0},\\ S(r,0) = \sigma, \quad T(r,0) = T_0, \quad p_a(r,0) = p_{a0} := 1\text{atm} - p_v(r,0),\\ p_c(r,0) = 0, \quad p_v(r,0) = p_v^*(T_0, \phi_0, \sigma).\end{gathered} \tag{5.30}$$

For the boundary conditions, we will need to consider what to do for the spherical shell (entire bean) and the sphere (chunks). We shall first make the assumption that any point on the surface of either of these geometries is easily accessible to the surrounding atmosphere. Therefore, after our spherical shell mapping, we will use the same boundary conditions on both the interior and exterior surface of the spherical shell. The surrounding atmosphere is controlled externally; here, we assume it has a total gas pressure of 1 atmosphere, has zero CO_2 gas present, and a fixed vapour gas pressure. Hence, at any point on the boundary, we have that

$$p_a + p_c + p_v = 1\text{atm}, \qquad p_c = 0, \qquad p_v = p_{v0}. \tag{5.31}$$

In addition, motion of the surrounding atmosphere causes convection-dominated heat transfer at the surface of the bean (as discussed in Chapter 2), and hence requires that

$$K_{\text{eff}} \nabla T \cdot \mathbf{n} = \left(\sum_i V_{f,i} h_i \right) (T_\infty - T), \tag{5.32}$$

where T_∞ is the controlled temperature of the roasting environment and h_i are the convective coefficients of each phase. However, by making the assumption that $(\sum_i V_{f,i} h_i)$ can be represented by a bulk heat convective coefficient h_b, this heat transfer boundary condition can be simplified to

$$K_{\text{eff}} \nabla T \cdot \mathbf{n} = h_b (T_\infty - T). \tag{5.33}$$

This gives us the boundary conditions we require for the system of equations at any surface.

Finally, if we are using the sphere geometry (chunks), we shall have to imposed regularity (i.e. symmetry) of the solution at the origin ($r = 0$).

5.5 Non-dimensionlisation of the Sugar Pathway Model

We nondimensionalise the model using the vapour diffusive timescale by letting

$$t = \theta \hat{t}, \qquad \text{where} \qquad \theta = \frac{\phi_0 \mu L^2}{k_{g0} P_0}, \quad r = L\hat{r}, \qquad P_0 = 1\text{atm}, \tag{5.34}$$

and L is the effective radius of the outer surface. We then set

$$\begin{gathered} \phi_1 = \phi_{10} U_1, \ \phi_2 = \phi_{10} U_2, \ \phi = \phi_0 Q, \ w_b = w_{b0} W, \ S = \sigma \hat{S}, \ T = T_0(1 + \mathscr{T}\hat{T}), \\ p_a = P_0 P_a, \ p_c = P_0 P_c, \ p_v = P_0 P_v, \ \text{ and } \ \mathcal{R}_i(T) = \alpha_i \hat{\mathcal{R}}_i(\hat{T}), \end{gathered} \tag{5.35}$$

so that (after dropping the hat notation) our non-dimensional equations become

$$\begin{aligned}\frac{\partial W}{\partial t} =& \kappa_1(\nu QS - W - \nu_2)\mathcal{R}_1(T) - \kappa_2 W\left[P_v - P_v^*(T,Q,S)\right]\mathcal{R}_2(T), && (5.36)\\ \frac{\partial}{\partial t}\left[QS\right] =& -\frac{\kappa_2}{\nu}W\left[P_v - P_v^*(T,Q,S)\right]\mathcal{R}_2(T), && (5.37)\\ \frac{\partial U_1}{\partial t} =& -\kappa_3 U_1(\nu QS - W - \nu_2)\mathcal{R}_3(T), && (5.38)\\ \frac{\partial U_2}{\partial t} =& \zeta_1\kappa_3 U_1(\nu QS - W - \nu_2)\mathcal{R}_3(T) - U_2[\kappa_4\mathcal{R}_4(T) + \kappa_5\mathcal{R}_5(T)], && (5.39)\\ \frac{\partial Q}{\partial t} =& \zeta_2\kappa_3 U_1(\nu QS - W - \nu_2)\mathcal{R}_3(T) + U_2[\zeta_3\kappa_4\mathcal{R}_4(T) + \zeta_4\kappa_5\mathcal{R}_5(T)], && (5.40)\end{aligned}$$

$$\begin{aligned}\frac{\partial}{\partial t}\left[\frac{P_a Q(1-\sigma S)}{1+\mathscr{T}T}\right] =& \nabla\cdot\left[\frac{P_a k_g}{1+\mathscr{T}T}\nabla(P_v + P_c + P_a)\right], && (5.41)\\ \frac{\partial}{\partial t}\left[\frac{P_c Q(1-\sigma S)}{1+\mathscr{T}T}\right] =& \nabla\cdot\left[\frac{P_c k_g}{1+\mathscr{T}T}\nabla(P_v + P_c + P_a)\right] && (5.42)\\ & + U_2\left[\zeta_5\kappa_4\mathcal{R}_4(T) + \zeta_6\kappa_5\mathcal{R}_5(T)\right], && (5.43)\\ \frac{\partial}{\partial t}\left[\frac{P_v Q(1-\sigma S)}{1+\mathscr{T}T}\right] =& \nabla\cdot\left[\frac{P_v k_g}{1+\mathscr{T}T}\nabla(P_v + P_c + P_a)\right] - \zeta_7\frac{\partial}{\partial t}\left[QS\right], && (5.44)\end{aligned}$$

$$\begin{aligned}\frac{\partial}{\partial t}\left[(1+\mathscr{T}T)H\right] =& -\frac{\kappa_1\eta_1}{\nu}(\nu QS - W - \nu_2)\mathcal{R}_1(T)\\ & -\frac{\kappa_2\eta_2}{\nu}W\left[P_v - P_v^*(T,Q,S)\right]\mathcal{R}_2(T)\\ & -\frac{\kappa_3\eta_3}{\nu}U_1(\nu QS - W - \nu_2)\mathcal{R}_3(T) - \kappa_4\eta_4 U_2\mathcal{R}_4(T)\\ & + \kappa_5\eta_5 U_2\mathcal{R}_5(T) + \kappa_6\nabla\cdot\left[K_{\text{eff}}\nabla T\right].\end{aligned} \tag{5.45}$$

The boundary conditions at the external surface of the bean ($r = 1$) are then

$$\frac{\partial T}{\partial r} = \frac{\text{Nu}(1-T)}{K_{\text{eff}}}, \qquad P_a = \mathcal{P}_1, \qquad P_c = 0, \qquad P_v = \mathcal{P}_2. \tag{5.46}$$

For the spherical shell geometry, there are boundary conditions needed on the inner surface ($r = a$) so that

$$\frac{\partial T}{\partial r} = -\frac{\text{Nu}(1-T)}{K_{\text{eff}}}, \qquad P_a = \mathcal{P}_1, \qquad P_c = 0, \qquad P_v = \mathcal{P}_2, \tag{5.47}$$

while for the spherical geometry, regularity requires Neumann boundary conditions at the centre of the bean ($r = 0$):

$$\frac{\partial T}{\partial r} = \frac{\partial P_a}{\partial r} = \frac{\partial P_c}{\partial r} = \frac{\partial P_v}{\partial r} = 0. \tag{5.48}$$

The initial conditions become

$$U_1(r,0) = 1, \quad U_2(r,0) = 0, \quad Q(r,0) = 1, \quad W(r,0) = 1, \quad S(r,0) = 1, \tag{5.49}$$

$$T(r,0) = 0, \quad P_a(r,0) = \mathcal{P}_1, \quad P_c(r,0) = 0, \quad P_v(r,0) = \frac{D_1 \exp(-D_2)}{1 + C_2\left(\frac{1}{\phi_0} - 1\right)^{C_1}}. \tag{5.50}$$

In this problem, the nondimensional functions are defined as

$$\mathcal{R}_i(T) = \exp\left(\beta_i(T-1)\right), \tag{5.51}$$

$$P_v^*(T,Q,S) = \frac{D_1 (QS)^{C_1} \exp\left(\frac{D_2(T-1)}{1+\mathscr{T}T}\right)}{(QS)^{C_1} + C_2\left(\frac{1}{\phi_0} - Q\right)^{C_1}}, \tag{5.52}$$

$$k_g = \max\left\{1 - \tilde{\nu}QS,\ 0\right\}, \tag{5.53}$$

$$H = QS + \omega_1(1 - \phi_0 Q) + (\omega_2 - \phi_{10}\omega_1)U_1 + (\omega_3 - \phi_{10}\omega_1)U_2, \tag{5.54}$$

$$K_g = \frac{P_v + \omega_8 P_c + \omega_9 P_a}{P_v + P_c + P_a}, \tag{5.55}$$

$$K_{\text{eff}} = \left[QS + \omega_4(1 - \phi_0 Q) + (\omega_5 - \phi_{10}\omega_4)U_1 + (\omega_6 - \phi_{10}\omega_4)U_2 + \frac{\omega_7 Q(1-\sigma S)}{K_g}\right]^{-1}, \tag{5.56}$$

while the nondimensional parameters are defined in Table 5.3, with typical values shown where known.

5.6 Numerical Simulations and Comparison with Experiments

We solve the Sugar Pathway Model using the method of lines exploiting a second-order accurate finite difference scheme in r. Using the stiff ODE solver `ode15s` in MATLAB, we can obtain the solution to the Sugar Pathway Model described in Section 5.5. In order to compare these predictions to experimental data, we can use the solutions to compute the average moisture content in a bean. For the spherical

Dimensionless Grouping	Relationship to Dimensional Parameters	Typical value of Parameter	Reference
C_1	–	0.41	[9]
C_2	–	6.1×10^{-3}	[9]
D_1	–	35.0	[10]
D_2	–	7.31	[10]
ν	$\frac{\phi_0 \sigma}{w_{b0}}$	100	Experimentally determined
ν_2	$\frac{w_n}{w_{b0}}$	10	Chosen to fit data
$\tilde{\nu}$	$\frac{\phi_0 \sigma}{\eta}$	0.1	Chosen to fit data
κ_1	$\alpha_1 \theta$	$2.3 \times 10^{-4} - 5.1 \times 10^{-3}$	Chosen to fit data
κ_2	$P_0 \alpha_2 \theta$	$120 - 2600$	Chosen to fit data
κ_3	$w_{b0} \alpha_3 \theta$	$4.7 \times 10^{-6} - 1.0 \times 10^{-5}$	Chosen to fit data
κ_4	$\alpha_4 \theta$	$1.2 \times 10^{-5} - 2.6 \times 10^{-4}$	Chosen to fit data
κ_5	$\alpha_5 \theta$	$1.2 \times 10^{-6} - 2.6 \times 10^{-5}$	Chosen to fit data
κ_6	$\frac{K_w}{\rho_w C_{pw}} \cdot \frac{\mu}{k_{g0} P_0} \cdot \frac{\mathscr{T}}{\phi_0 \sigma^2}$	0.14	[29]
ζ_1	$\frac{\rho_1}{\rho_2}$	0.97	[20]
ζ_2	$\left(1 - \frac{\rho_1}{\rho_2}\right) \frac{\phi_{10}}{\phi_0}$	3.0×10^{-3}	[20]
ζ_3	$\left(1 - \frac{\rho_2 \chi_2}{\rho_3}\right) \frac{\phi_{10}}{\phi_0}$	0.067	[20]
ζ_4	$\left(1 - \frac{\rho_2}{\rho_3}(1 - \chi_1 - \chi_2 - \chi_3)\right) \frac{\phi_{10}}{\phi_0}$	0.067	[20]
ζ_5	$\frac{R T_0 \rho_2 \phi_{10} \chi_1}{P_0 m_c \phi_0}$	27	[20]
ζ_6	$\frac{R T_0 \rho_2 \phi_{10} \chi_3}{P_0 m_c \phi_0}$	9.0	[20]
ζ_7	$\frac{R T_0 \rho_w \sigma}{P_0 m_v}$	110	[20]
ω_1	$\frac{\rho_3 C_{p3}}{\rho_w C_{pw} \phi_0 \sigma}$	0.062	Chosen to fit data
ω_2	$\frac{\rho_1 C_{p1} \phi_{10}}{\rho_w C_{pw} \phi_0 \sigma}$	1.8	[20]
ω_3	$\frac{\rho_2 C_{p2} \phi_{10}}{\rho_w C_{pw} \phi_0 \sigma}$	0.58	Chosen to fit data
ω_4	$\frac{K_w}{K_3 \phi_0 \sigma}$	240	[20]
ω_5	$\frac{K_w \phi_{10}}{K_1 \phi_0 \sigma}$	1.4	[20]
ω_6	$\frac{K_w \phi_{10}}{K_2 \phi_0 \sigma}$	2.4	[20]
ω_7	$\frac{K_w}{K_v \sigma}$	450	Experimentally determined
ω_8	$\frac{K_a}{K_v}$	1.5	Chapter 2
ω_9	$\frac{K_c}{K_v}$	0.94	Chapter 2
η_1	$\frac{\lambda_1}{T_0 C_{pw}}$	2.4	Chosen to fit data
η_2	$\frac{\lambda_2}{T_0 C_{pw}}$	1.9	Chosen to fit data
η_3	$\frac{\rho_1 \lambda_3 \phi_{10}}{\rho_w T_0 C_{pw} \phi_0 \sigma}$	2.8×10^{-3}	Chosen to fit data
η_4	$\frac{\rho_2 \phi_{10} \lambda_4}{\rho_w \phi_0 \sigma T_0 C_{pw}}$	0.41	Chosen to fit data
η_5	$\frac{\rho_2 \phi_{10} \lambda_5}{\rho_w \phi_0 \sigma T_0 C_{pw}}$	6.7×10^{-3}	Chosen to fit data
$\mathcal{P}_1$	$\frac{p_{a0}}{P_0}$	0.98	Experimentally determined
$\mathcal{P}_2$	$\frac{p_{v0}}{P_0}$	0.024	Experimentally determined
Nu	$\frac{h_b L \phi_0 \sigma}{K_w}$	$1.5 - 6.9 \times 10^{-4}$	Chosen to fit data
$\mathscr{T}$	$\frac{T_\infty}{T_0} - 1$	0.72	Experimentally determined

Table 5.3: Description and typical values of dimensionless groupings used in the Sugar Pathway Model. The range of values for κ_i and Nu are based on using lengths from the chopped bean radius ($L = 0.7$mm) to the whole bean spherical shell ($L = 3.3$mm).

shell, this average moisture content is given by

$$M_{avg}(t) = \frac{3\rho_w \phi_0 \sigma}{\rho_b(1-a^3)} \int_a^1 Q(r,t)S(r,t)r^2 \, \mathrm{d}r, \tag{5.57}$$

where ρ_b denotes the bulk density of the coffee bean, and the same formula is valid for the solid sphere geometry by setting $a = 0$. For the calculations presented here, the chopped bean used a value of $L = 0.7\text{mm}$ while the whole bean used $a = 0.47$, $L = 3.3\text{mm}$.

To fit the data, we have chosen many parameter values to get a good fit to the experimental data for moisture content. However, we appear to be able to choose values for the permeability over a vast range but we can still get a good fit by appropriately choosing $h_b = 3.0 - 3.5$ $\text{Wm}^{-2}\text{K}^{-1}$. As we will see in Section 5.7, the qualitative features of the Sugar Pathway Model are robust to small changes in parameter values. To illustrate this, we have chosen to fit the data with two different values of permeability. The first is that appropriate to Darcy flow in timber of 2.5×10^{-14} m^2, which is similar to values of wood permeabilities seen in [29]. The second comes from estimates made on a different experiment using coffee beans [1]. After coffee beans have been roasted, it is very common to quickly quench them to room temperature and then allow them to temper. This tempering is done by placing the beans in a bag and leaving them for several hours. During this rest period, significant quantities of gas come out of the bean and can be seen to inflate the bag. In [1], the authors assume that the gas is transported via linear diffusion and an estimate is made of the diffusion coefficient necessary to see the length decay rate. There has been no other substantive modelling or experimental data collected on this behaviour, so this value is speculative but given as 2.5×10^{-16} m^2. We will use this value as our second value for fitting the Sugar Pathway Model.

The predictions of the model using these two values of permeability, with h_b chosen to make the fit, are shown in Figure 5.4, and show the Sugar Pathway Model has good agreement with the two experimental data sets of the chopped bean experiment. It is important to note that the last two data points of the roasted whole bean experiment are after an event known as First Crack [51], where macroscopic deformation of the coffee bean has occurred. In consequence, these two data points may be affected by mechanisms not included in the Sugar Pathway Model. This demonstrates that the issues concerning length scale have now been resolved and that there is a range of possible permeabilities that might be reasonable.

In both parameter cases, as was seen in Chapter 3, the timescale for thermal diffusion across the bean is much smaller than the timescale for gas flow (i.e. $\kappa_6 \ll 1$). This implies that the temperature in the bean is nearly spatially uniform throughout the entire roasting process (see Figure 5.5(a)). This in turn implies that the global chemical reaction rates $\mathcal{R}_i(T)$ will also be nearly spatially uniform and cause Q, U_1, U_2 and S to display similar features. One notable exception to this, however, is in the early roasting time for W. With reference to Figure 5.5(b), we see that the bound water content is driven to very small levels early in the roasting and displays similar features to the *drying front* discussed in Chapter 3. However, we note that in these regions of small bound water (when $W \ll 1$), the cell water that is released at a rate determined by $\mathcal{R}_1(T)$ immediately evaporates. Thus, the mechanism that slows the overall evaporation rate is linked to the degradation rate $\mathcal{R}_1(T)$ rather than the gas permeability k_g.

As previously discussed in Chapter 4, we note that the vapour pressure P_v is aligned with the sorption isotherm for the entirety of the roast. However, due to the interplay between increasing temperature and decreasing water saturation, the sorption isotherm is non-monotone. Furthermore, due to the gas permeability being smaller in areas of higher saturation, the vapour pressure can also increase at the beginning of the roast when the water content is highest. Due to these combined effects, we observe significant fluctuations in vapour pressure at the beginning of the roast (Figure 5.6).

For the large permeability case, we note that the gas species are nearly spatially uniform, as seen in Figure 5.7(a). This is due to the fact that the removal of water vapour from the bean is controlled by the degradation reaction, described by $\mathcal{R}_1(T)$, and the uniform temperature is being restricted by the low heat transfer coefficient. Once the cell degrades, the water vapour is easily transported to the surface by Darcy flow. For the very small permeability case, as seen in Figure 5.7(b), the gas pressures vary significantly and there is a drying front that travels through the bean. In this case, the cell degradation rate is relatively rapid, so that the water can evaporate quickly but is then severely restricted in diffusing out of the bean, creating large gas pressures. Note that in this case, the chemical reactions are not as spatially uniform, as the hydrolysis reaction $\mathcal{R}_3(T)$ depends on water and the presence of the drying front makes this occur at different rates in different parts of the bean.

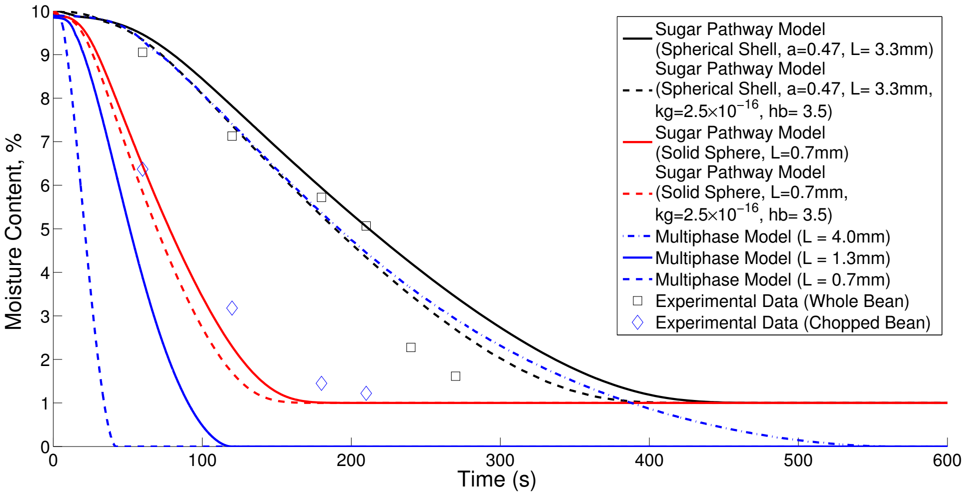

Figure 5.4: Comparison of the average moisture content in a bean chunk versus a whole bean during a 230°C roast. The solid and dot-dashed lines correspond to the average moisture loss determined by the Sugar Pathway Model (5.36)-(5.56), described in Section 5.5, with parameters (unless otherwise listed in the legend) obtained from Table 5.3. The dashed lines correspond to the average moisture loss determined by the Multiphase Model (3.1)-(3.8) presented in Chapter 3, and the markers correspond to experimental data seen in Table 5.1.

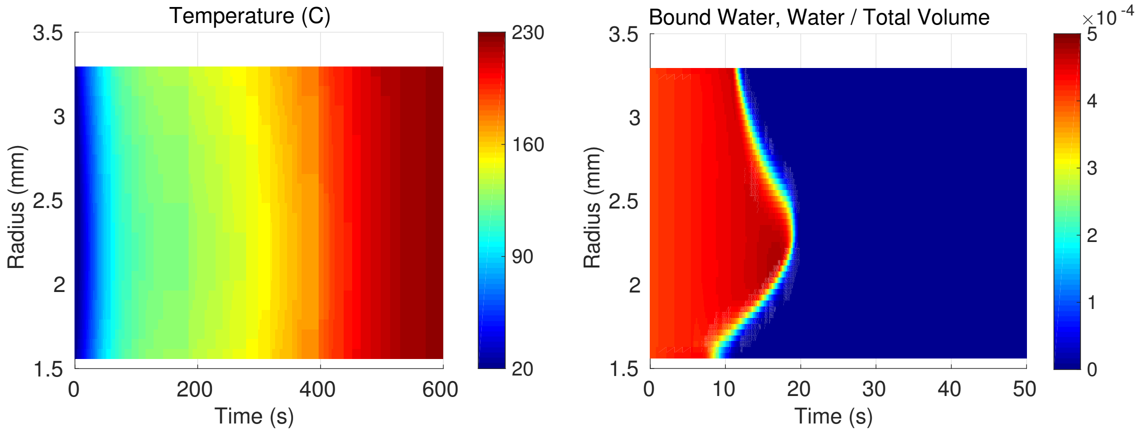

(a)

(b)

Figure 5.5: (a) Temperature $T(r, t)$ over a 600-second roast at 230°C in the spherical shell geometry. (b) The short-time behaviour for $W(r, t)$ in the spherical shell geometry. All parameters for both figures are the upper bound of values listed in Table 5.3.

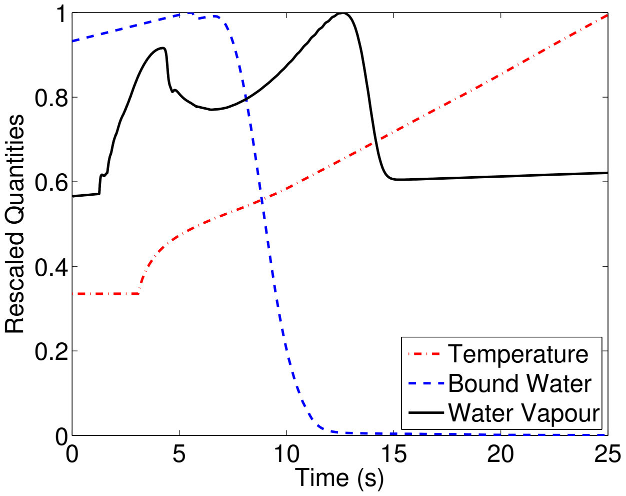

Figure 5.6: The short-time behaviour for temperature $T(t)$, bound water $W(t)$, and vapour pressure $P_v(t)$ near the inner surface of the spherical shell geometry. The three variables have been rescaled by their maximal values to highlight their qualititative changes. All parameters for both figures are the upper bound of values listed in Table 5.3.

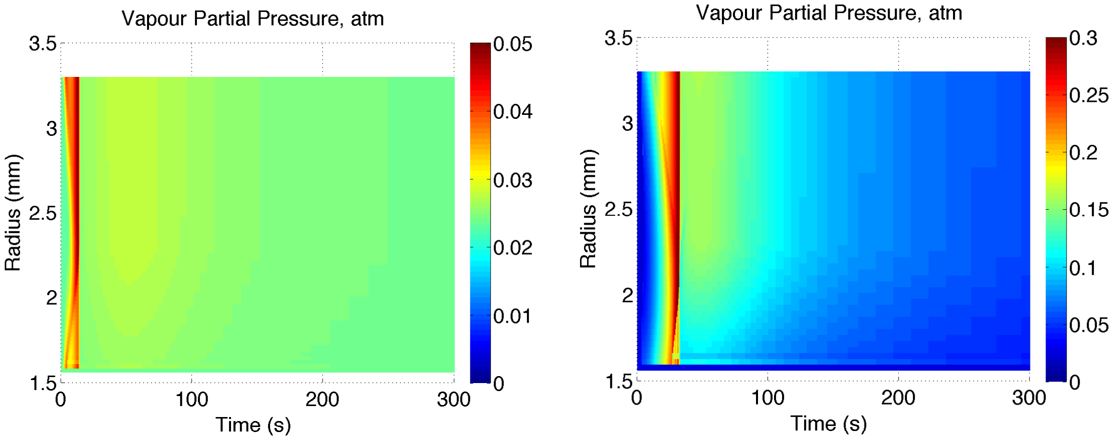

(a)

(b)

Figure 5.7: The partial vapour pressure $p_v(r,t)$ for the first 300 seconds of a 230°C roast in the spherical shell geometry, with (a) $k_g = 2.5 \times 10^{-14}$ and $h_b = 3$; (b) $k_g = 2.5 \times 10^{-16}$ and $h_b = 3.5$. All other parameters for both figures are the upper bound of values listed in Table 5.3.

5.7 Parameter Sensitivity

The Sugar Pathway Model has 19 dimensionless groups that have unknown values. Hence, it is appropriate to consider how sensitive the Sugar Pathway Model is to changing values of dimensionless parameter values. With reference to Figure 5.8, we see four general qualitative features that occur when altering values of these dimensionless groups. We focus on the sensitivity of the temperature and moisture content of the bean due to the lack of experimental data for the other variables.

The first qualitative feature seen is a "faster reaction" effect, where an increase (or decrease) in a parameter's value causes the bean to heat up on a shorter timescale. This can also be seen in the bean's average moisture content, where a different parameter value causes the moisture to be lost at a faster rate. We observe this phenomenon when $\omega_1, \omega_3, \kappa_2, \eta_1$, and η_4 are decreased, or h_b is increased, from the parameter values stated in Table 5.3. As previously mentioned in this section, we can allow for a smaller gas permeability value k_g if we increase h_b. Since these other dimensionless groupings exhibit similar qualitative changes when their parameter values are decreased, we infer that one could use each parameter value to compensate for a smaller value of k_g and still match the experimental data.

Another feature seen in certain parameter regimes is a stronger effect of the exothermic caramelisation reaction group. Naturally, this is observed when η_5 is increased, as this corresponds to more energy being produced from the caramelisation reaction group and therefore causes the bean to heat up faster, even surpassing the roasting temperature in some cases. Curiously, however, we also see similar a phenomenon when ω_3 or κ_3 increases, as well as when β_3 decreases. We infer that when the reducing sugars are easier to react via the caramelisation reaction group (such as in the case of larger κ_3 and smaller β_3) and more energy is released into the system.

We find that the bean's temperature changes for intermediate time when κ_1 and β_1 are changed. This is to be expected, as the cell degradation reaction group determines the free water content in the bean, which is then used to hydrolyse sucrose in the bean. If this reaction is slower than later reactions (e.g. larger β_1 or smaller κ_1), then hydrolysed sucrose will immediately be consumed by the Maillard and caramelisation reaction groups. Therefore, an understanding of the parameters used in the cell degradation reaction group is critical in determining the various products in the Sugar Pathway Model: in particular, the Maillard and caramelisation products.

We see changes in the final moisture content when ν_2 is varied. This is to be ex-

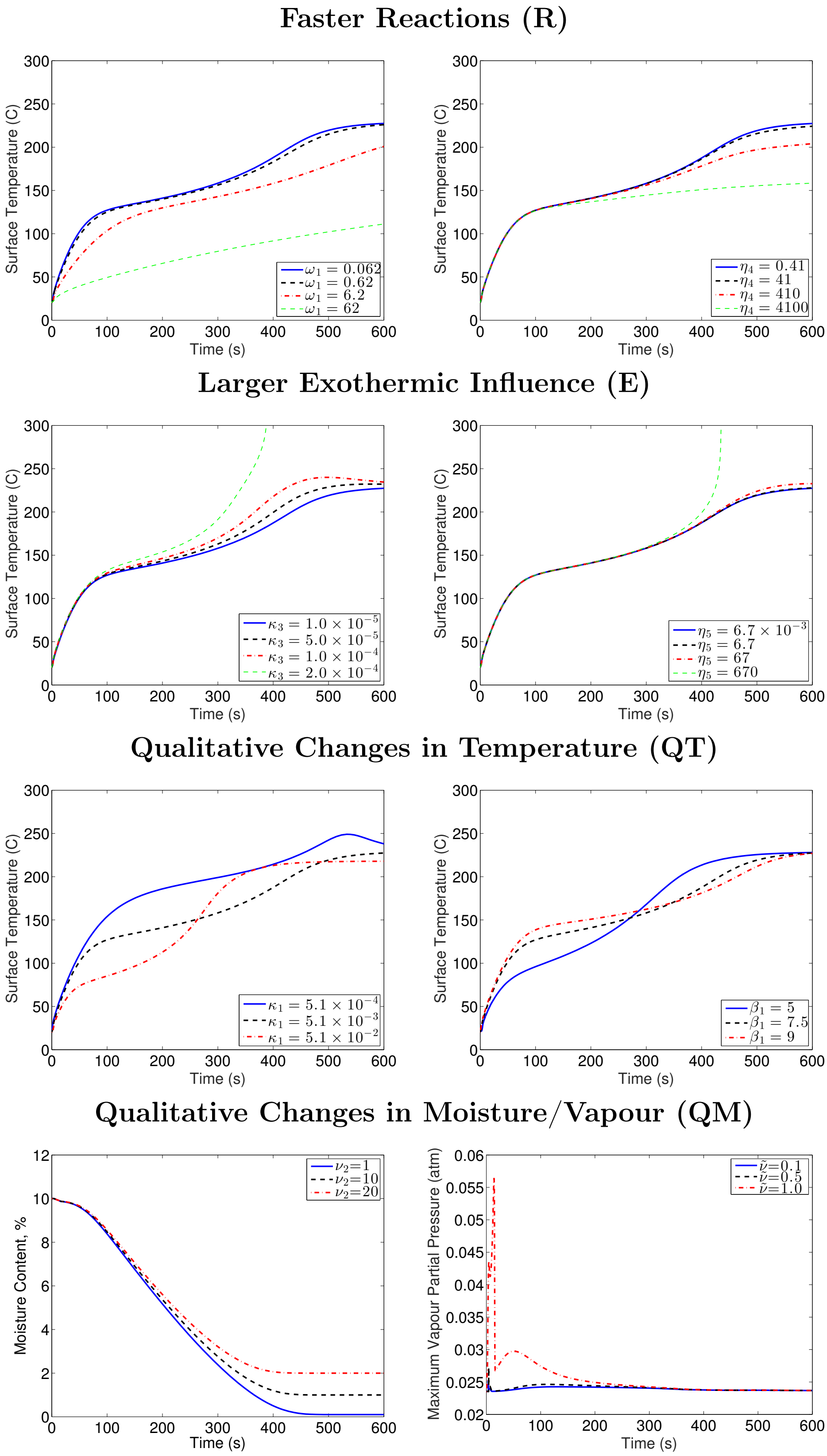

Figure 5.8: Qualitative changes observed for various values of dimensionless groupings. All parameters for both figures are the upper bound of values listed in Table 5.3 unless specified in the figure.

Qualitative Feature	Dimensionless Grouping
R	inc h_b; dec $\omega_1, \omega_3, \kappa_2, \eta_1, \eta_4$
E	inc $\omega_3, \kappa_3, \eta_5$; dec β_3
QT	κ_1, β_1
QM	$\nu_2, \tilde{\nu}$ (provided $\tilde{\nu} \leq 1$)
(No significant change observed)	$\kappa_4, \kappa_5, \beta_2, \beta_4, \beta_5, \eta_3$

Table 5.4: A summary of the sensitivity of dimensionless groupings used in the Sugar Pathway Model by qualitative features. Faster reactions (R) and a larger exothermic influence (E) are observed when certain parameters are increased (inc) or decreased (dec), while qualitative changes in temperature (QT) and moisture/vapour content (QM) are observed in others. See Figure 5.8 for the behaviour of each feature.

pected, since a larger value of ν_2 implies having a larger quantity of inaccessible water that will remain for the duration of the roast. Indeed, the value of ν_2 corresponds to the percentage of initial water remaining as $t \to \infty$ (so, $\nu_2 = 10$ implies that 10% of the initial water content in the bean will remain after roasting). This parameter can therefore be determined via further "chopped green coffee bean experiments" to determine how much inaccessible water is present in a coffee bean. Additionally, we see a larger vapour pressure only for larger values of $\tilde{\nu}$. When $\tilde{\nu} > 1$, however, the vapour transport mechanism described in Section 5.4.3 is invalid and a different model for variable gas permeability should be used. However, typical values of $\tilde{\nu}$ indicate that $\tilde{\nu} \approx 0.1$ [61], so we anticipate that our variable permeability model is reasonably valid.

Finally, there are a large number of dimensionless groupings that yield no significant changes to the predictions of the Sugar Pathway Model. Specifically, no changes in the qualitative features of temperature and moisture content were observed for various values of $\kappa_4, \kappa_5, \beta_2, \beta_4, \beta_5$, and η_3. A summary of all the different qualitative features is shown in Table 5.4.

5.8 Discussion

In this chapter, we have incorporated modified evaporation rates and chemical reaction groups to improve existing mathematical models of roasting coffee beans. These additions were motivated both by the inability of previous mathematical models to reproduce experimental data at different length scales as well as some physically unrealistic parameter values. These limitations were discussed and we provided a brief overview of the existing models presented in [13] and Chapters 2 and 3. In particular, the chopped green coffee bean thought experiment discussed in Chapter 2 was undertaken and data compared with predictions. The experiments suggested that the evaporation mechanism presented in Chapter 2 did not reflect moisture transport in a roasting bean with sufficient accuracy, and hence a different approach was required to model the evaporation rate inside a roasting bean.

We presented a model of evaporation of the water in a roasting coffee bean in two stages: the first being release of cell water into bound water by degradation of the cell, and the second by bound water evaporating. We considered evaporation of bound water using the ideas of chemical reaction groups. By assuming that this chemical reaction group has a distribution of activation energies, the evaporation rate had a *global* reaction rate. We also incorporated how evaporation is affected by deviation of vapour pressure from an equilibrium vapour pressure of the bound water.

Motivated by the global reaction rate, we then used these ideas to account for additional chemical reactions relevant to flavour development. As these reactions are complicated, we examined a simplified sugar pathway network, which turns sucrose into CO_2 gas and other solids via reducing sugars. Modelling this pathway also required us to model the transport of gases other than water vapour (in this case, CO_2 and air) within the bean, as well as the energy produced or consumed during these additional chemical reactions.

We revisited the idealised geometry to use for a coffee bean, finding a spherically symmetric shell to be a more appropriate representation of a whole coffee bean than a solid sphere. We also considered that chunks of bean, as used in the chopped bean experiment, are adequately represented by solid spheres.

We solved the Sugar Pathway Model numerically, and were able to compare our simulations to data obtained from roasting experiments we performed on both solid coffee beans and chopped green coffee beans. Indeed, we found that with a more suitable choice of geometries, the Sugar Pathway Model agrees well with the moisture data obtained from experiments. However, we also found that we needed to choose combinations of the heat transfer coefficient and the permeability in order to make a good fit, but that we could not identify what combination was appropriate just by fitting the moisture content data. This lack of parameter identifiability is due to the fact that the rate at which moisture is lost can be controlled in the model either by altering the temperature, so that the cell degradation controls evaporation, or altering the permeability, to restrict the rate at which the water vapour is transported to the surface. Any combination of these two effects that give the same overall restriction to water vapour transport will fit the moisture data.

We undertook a sensitivity analysis to examine how model solutions depend on parameters whose values were not known from independent sources. We found four main types of qualitative behaviours, namely: faster reactions, stronger dependence on exothermic reaction groups, different thermal behaviours for intermediate time, and different final moisture contents. We also determined the relevant non-dimensional parameters controlling each of these behaviours. While one could improve the fit of the model with additional experimental data, the physically relevant behaviour has been identified via a few notable dimensionless groups. Hence, we believe that the general qualitative behaviour we have identified is robust to the parameters in the Sugar Pathway Model. However, one main aspect of the mathematical modelling that has been omitted thus far is how the structural components of the coffee bean change as it is roasted. We will consider these structural deformations in the context of our multiphase models in Chapter 6.

Chapter 6

Modelling Structural Deformations in a Roasting Coffee Bean

6.1 Introduction

While we have addressed the incorporation of multiphase heat and mass transfer and chemical reaction groups into our model, we now turn our attention to the concepts of solid mechanics and structural degradation of the cell walls within a coffee bean during roasting. Incorporating these elements into our model should provide additional insight into large-scale phenomena that are observed as a coffee bean is being roasted. For instance, one main justification for the incorporation of structural deformation is the need to explain First Crack. As previously discussed in Chapter 1, a distinct popping sound can be heard during First Crack. By including solid mechanics effects into our roasting model, it is possible that large-scale deformations of the cellulose structure of the coffee bean can be properly accounted for. Here, we will investigate the structural properties of a coffee bean as it is roasted. In particular, we shall investigate the stresses and strains produced in a coffee bean due to high gas pressures and increasing temperature.

6.2 Modelling the Cellulose Structure

In this section, we model the cellulose structure as a poroviscoelastic material. However, experimental data suggests that certain parameters that appear in the underlying poroviscoelastic equations are temperature-dependent. In particular, these parameters change significantly at a *glass transition temperature* that is a function of local moisture content. Certain simplifications are made to reduce the parameter regime of the poroviscoelastic equations while still being physically reasonable; additionally, we propose models to describe these temperature-dependent parameters while employing typical values where known. These equations are then further examined in a spherically symmetric domain, where they are in turn coupled to the Modified Multiphase Model discussed in Section 4.3.

6.2.1 Governing Poroviscoelastic Equations

In order to model deformations within a coffee bean, we must first understand how the solid phase, specifically the cellulose structure, behaves. We begin by assuming that the cellulose material in the solid phase can be represented as an isotropic poroviscoelastic material with a gas pressure, denoted as P, inside the porous structure. Additionally, we assume that only small displacements occur, implying that linear elasticity and viscoelasticity constitutive equations are valid. As large deformations are not observed until the bean fractures, rendering our models invalid, these assumptions are plausible. Since we anticipate permanent deformations to occur in the bean, we will assume that the elastic and viscous strains of the cellulose are in series (i.e. a Maxwell viscoelastic model [24]). With these assumptions, our constitutive equations for the elastic strain $\boldsymbol{\epsilon}^e$ and viscous strain $\boldsymbol{\epsilon}^v$ are related to the effective material stress $\boldsymbol{\tau}^E$, given in [24], by

$$\begin{aligned} \boldsymbol{\epsilon} &= \boldsymbol{\epsilon}^e + \boldsymbol{\epsilon}^v, && (6.1)\\ \boldsymbol{\tau}^E &= \Lambda(\mathrm{tr}\ \boldsymbol{\epsilon}^e)\boldsymbol{I} + 2\mathcal{M}\boldsymbol{\epsilon}^e, && (6.2)\\ \boldsymbol{\tau}^E &= \xi\frac{\partial}{\partial t}(\mathrm{tr}\ \boldsymbol{\epsilon}^v)\boldsymbol{I} + 2\eta\frac{\partial \boldsymbol{\epsilon}^v}{\partial t}. && (6.3) \end{aligned}$$

Here, Λ and $\mathcal{M}$ are the Lamé coefficients of the cellulose material, while ξ and η are the bulk and shear viscosities of the cellulose, respectively [24]. We then combine the constitutive equations (6.1)-(6.3) to obtain

$$\frac{\partial}{\partial t}\left[\frac{\boldsymbol{\tau}^E}{\Lambda}\right] + \frac{\boldsymbol{\tau}^E}{\xi} = \frac{\partial}{\partial t}\left[(\mathrm{tr}\ \boldsymbol{\epsilon})\boldsymbol{I} + 2\frac{\eta}{\xi}\boldsymbol{\epsilon}\right] - 2\boldsymbol{\epsilon}\frac{\partial}{\partial t}\left[\frac{\eta}{\xi}\right] + \frac{\partial}{\partial t}\left[2\left(\frac{\mathcal{M}}{\Lambda} - \frac{\eta}{\xi}\right)\boldsymbol{\epsilon}^e\right]. \quad (6.4)$$

Finally, we can decompose the the total stress $\boldsymbol{\tau}$ using Terzaghi's stress principle (see e.g. [57]) as the difference of the effective stress of the cellulose and the total gas pressure in the material P:

$$\boldsymbol{\tau} = \boldsymbol{\tau}^E - P\boldsymbol{I}. \quad (6.5)$$

This is coupled with the steady-state conservation of linear momentum equation, as we assume that the acceleration of the displacement of cellulose is negligible:

$$\boldsymbol{\nabla} \cdot \boldsymbol{\tau} = \mathbf{0}. \tag{6.6}$$

6.2.2 Reducing the Parameter Regime

In order for the poroelastic and poroviscoelastic regimes to agree at the glass transition temperature, we must ensure that the ratio of viscosities is equal to the ratio of Lamé parameters, i.e.

$$\frac{\mathcal{M}}{\Lambda} = \frac{\eta}{\xi} := \frac{2-\varsigma}{2\varsigma}. \tag{6.7}$$

This simplification is often taken with viscoelastic materials (c.f. [24]) and is equivalent to stating that the elastic and viscous components have the same Poisson's ratio. Additionally, we will assume that this ratio is constant (i.e. that ς is constant). In consequence, (6.4) becomes

$$\frac{\partial}{\partial t}\left[\frac{\boldsymbol{\tau}^E}{\Lambda}\right] + \frac{\boldsymbol{\tau}^E}{\xi} = \frac{\partial}{\partial t}\left[(\text{tr}\,\boldsymbol{\epsilon})\boldsymbol{I} + \left(\frac{2-\varsigma}{\varsigma}\right)\boldsymbol{\epsilon}\right]. \tag{6.8}$$

6.2.3 The Glass Transition Temperature

We anticipate that the cellulose structure in a coffee bean will behave differently at different temperatures, with very large changes occuring at the transition. This phenomenon is common amongst organic materials and such a transition of material properties can often be reflected via a *glass transition temperature* [50]. Specifically, the glass transition temperature represents the transition in amorphous materials from behaving like a brittle (or, elastic) material to a rubbery (or, viscous) material. Crucially, this glass transition temperature, denoted here as T_G, also depends on the material's moisture content [50]. A simple empirical relationship for T_G, which agrees with qualitative features seen in experimental data, is given by

$$T_G(Y) = \frac{T_{\text{dry}}}{1 + \frac{Y}{Y^*}\left(\frac{T_{\text{dry}}}{T_0} - 1\right)}, \tag{6.9}$$

where Y is the mass fraction of water, T_{dry} is the glass transition temperature at zero moisture, and Y^* is the mass fraction at which the glass transition occurs at room temperature (T_0). In terms of variables described in previous chapters, we relate Y

to the volume fraction of water by use of

$$Y = \frac{1}{1 + \frac{\rho_s(1-\phi)}{\rho_w \phi S}}, \tag{6.10}$$

which puts (6.9) into the form

$$T_G(\phi, S) = \frac{T_{\text{dry}}\left(1 + \frac{\rho_s(1-\phi)}{\rho_w \phi S}\right)}{1 + \frac{\rho_s(1-\phi)}{\rho_w \phi S} + \frac{1}{Y^*}\left(\frac{T_{\text{dry}}}{T_0} - 1\right)}. \tag{6.11}$$

When the temperature locally is below the glass transition temperature, we expect that the coffee bean behaves elastically; that is to say, the viscosity of the cellulose is very large in comparison to the elasticity parameters. Above the glass transition temperature, however, the cellulose will permanently deform due to viscous effects. This implies that, unlike previously described poroviscoelastic models (c.f. [24]), the viscosities and/or the Lamé coefficients of the cellulose will vary with temperature. The authors of [45] observed that these parameters in coffee beans decrease in a sigmoidal manner near the glass transition temperature. While various constitutive equations can be employed, we propose a simple model to reflect this sigmoidal behaviour in Λ and ξ:

$$\Lambda = \frac{\lambda_1 + \lambda_2}{2} + \left(\frac{\lambda_2 - \lambda_1}{2}\right)\tanh\left(\frac{T - T_G(\phi, S)}{T_{\text{crit}}}\right), \tag{6.12}$$

$$\xi = \frac{\xi_1 + \xi_2}{2} - \left(\frac{\xi_1 - \xi_2}{2}\right)\tanh\left(\frac{T - T_G(\phi, S)}{T_{\text{crit}}}\right). \tag{6.13}$$

Here, λ_1 and λ_2 are the Lamé coeffecients of the cellulose at low and high temperatures, ξ_1 and ξ_2 are the viscosities of the cellulose at low and high temperatures, and we define T_{crit} as a physical parameter representing the sharpness of the sigmoidal transition. A small value of T_{crit} represents a sharp and rapid transition between parameter regimes, whereas a larger value of T_{crit} represents a more gradual change in the cellulose's elastic and viscous properties. As we anticipate a larger viscosity and/or Lamé coefficient when $T < T_G$, we will assume that $\lambda_1 > \lambda_2$ and $\xi_1 > \xi_2$.

6.2.4 Determining Typical Parameter Values Associated with the Glass Transition Temperature

It is expected that, in an isothermal setting, the Lamé coefficient λ_1 will be a function of porosity and water saturation to reflect the porous cellulose structure. Using the isothermal closed cell model proposed in [19], which is a suitable model to describe the porous structure of a coffee bean, we infer the empirical relationship

$$\frac{\lambda_1}{\Lambda^*} \sim \phi^2 \left(1 - \phi + \phi S \frac{\rho_w}{\rho_s}\right)^2 + (1 - \phi)\left(1 - \phi + \phi S \frac{\rho_w}{\rho_s}\right). \tag{6.14}$$

Here, Λ^* represents the Lamé coefficient of solid cellulose (≈ 59600 atm, [62]) and $\frac{\rho_w}{\rho_s}$ is the density ratio of water to solid cellulose (≈ 1.18, [5]). As seen in Chapters 2 and 5, we anticipate that $\phi \approx 0.5$ and $S \in [0, 0.1]$, which suggests that $\frac{\lambda_1}{\Lambda^*} \in [0.31, 0.36]$. Therefore, we assume that at low temperatures,

$$\lambda_1 \approx 0.335\Lambda^* \approx 2 \times 10^4 \text{ atm}. \tag{6.15}$$

Typical values of the Lamé coefficients of cellulose have been examined extensively in [62]; from these values, we assume that $\varsigma \approx 0.72$. It is unclear how large λ_2 should be, as viscous deformations now dominate the deformations in the cellulose. However, we shall see later that the choice of λ_2 does not affect the dominant effects of the cellulose deformations.

For typical values of ξ, it is unclear how large ξ_1 should be to reflect that the deformations below the glass transition temperature are purely elastic. However, the apparent viscosity has been measured for various wood/plastic composite materials (c.f. [27]); typical values indicate that

$$\xi_2 \approx 10^5 \text{ Pa}\cdot\text{s} \tag{6.16}$$

is a reasonable assumption to make.

Finally, is it important to determine typical parameter values used in the glass transition temperature (6.11), in order to understand how sharp of a transition is to be expected between the two Lamé coefficients and viscosities. Many of these glass transition parameter values have been recorded for coffee beans (see e.g. [45]); using these values, we assume that

$$T_{\text{crit}} \in [10^\circ\text{C}, 30^\circ\text{C}], \quad T_{\text{dry}} \approx 190^\circ\text{C}, \quad \text{and} \quad Y^* \approx 0.995. \tag{6.17}$$

6.2.5 Governing Equations in Spherical Symmetry

Having discussed how the Lamé coefficients and viscosities are temperature-dependent, along with their typical parameter values, we now return to the poroviscoelastic equations described in Section 6.2.1 to model deformations in the cellulose structure and examine the special, but physically relevant case, of spherical symmetry. In a spherically symmetric domain with symmetric boundary conditions, the displacement $\mathbf{u}$ is purely radial (i.e. $\mathbf{u} = [u(r), 0, 0]^\top$) and (6.6) reduces to

$$\tau_{\theta\theta} = \frac{1}{2r}\frac{\partial}{\partial r}\left[r^2 \tau_{rr}\right], \tag{6.18}$$

where τ_{rr} and $\tau_{\theta\theta}$ denote the radial and hoop (angular) stresses, respectively. Additionally, the radial and angular strains, e_{rr} and $e_{\theta\theta}$, can be written as

$$e_{rr} = \frac{\partial u}{\partial r}, \qquad e_{\theta\theta} = \frac{u}{r}, \tag{6.19}$$

respectively. Therefore, we can determine the radial and angular components of (6.8) and obtain

$$\frac{\partial}{\partial t}\left[\frac{\tau_{rr} + P}{\Lambda}\right] + \frac{\tau_{rr} + P}{\xi} = \frac{\partial}{\partial t}\left[\frac{1}{r^2}\frac{\partial}{\partial r}(r^2 u) + 2\frac{\eta}{\xi}\frac{\partial u}{\partial r}\right], \tag{6.20}$$

$$\frac{\partial}{\partial t}\left[\frac{1}{\Lambda}\frac{\partial \tau_{rr}}{\partial r} + \frac{\partial}{\partial r}\left(\frac{4\eta u}{\xi r}\right)\right] + \frac{1}{\xi}\frac{\partial \tau_{rr}}{\partial r} = 0. \tag{6.21}$$

As we will have more information at the boundaries of the coffee bean for u than for τ_{rr}, we will now manipulate (6.20), (6.21) to eliminate explicit spatial derivatives in τ_{rr}. Firstly, (6.20), (6.21) can be expressed as

$$\frac{\partial \tau_{rr}}{\partial t} = -\frac{\partial P}{\partial t} + \Lambda\left[\frac{2}{\varsigma}\frac{\partial^2 u}{\partial t \partial r} + \frac{2}{r}\frac{\partial u}{\partial t} - (\tau_{rr} + P)\Omega\right], \tag{6.22}$$

$$\frac{\partial \tau_{rr}}{\partial r}\Omega = -\frac{1}{\Lambda}\frac{\partial^2 \tau_{rr}}{\partial t \partial r} - \left(\frac{4 - 2\varsigma}{\varsigma}\right)\frac{\partial}{\partial r}\left(\frac{1}{r}\frac{\partial u}{\partial t}\right), \tag{6.23}$$

where

$$\Omega = \frac{1}{\xi} - \frac{1}{\Lambda^2}\frac{\partial \Lambda}{\partial t}. \tag{6.24}$$

Substituting (6.22) into (6.23) yields, after some rearranging of terms,

$$\frac{\partial}{\partial r}\left[\Lambda\left(\frac{2}{\varsigma}\frac{\partial^2 u}{\partial t \partial r} + \frac{2}{r}\frac{\partial u}{\partial t}\right)\right] + \left(\frac{4 - 2\varsigma}{\varsigma}\right)\frac{\partial}{\partial r}\left(\frac{1}{r}\frac{\partial u}{\partial t}\right) = \frac{\partial^2 P}{\partial t \partial r} + (\tau_{rr} + P)\frac{\partial}{\partial r}(\Lambda\Omega) + \Lambda\Omega\frac{\partial P}{\partial r}. \tag{6.25}$$

This then allows us to couple (6.22) to the following second-order differential equation for the material's velocity $\frac{\partial u}{\partial t}$

$$\frac{\partial^3 u}{\partial t \partial r^2} + \frac{\partial u}{\partial t \partial r}\left(\frac{1}{\Lambda}\frac{\partial \Lambda}{\partial r} + \frac{2}{r}\right) + \frac{1}{r}\frac{\partial u}{\partial t}\left(\frac{\varsigma}{\Lambda}\frac{\partial \Lambda}{\partial r} - \frac{2}{r}\right)$$
$$= \frac{\varsigma}{2\Lambda}\left[\frac{\partial^2 P}{\partial t \partial r} + (\tau_{rr} + P)\frac{\partial}{\partial r}(\Lambda\Omega) + \Lambda\Omega\frac{\partial P}{\partial r}\right]. \qquad (6.26)$$

We will refer to the poroviscoelastic equations as the equations (6.22) and (6.26).

6.2.6 Boundary and Initial Conditions

For the initial data relating to the poroviscoelastic equations, we assume that the bean starts from a reference state of zero displacement, i.e. a strain-free initial state, giving

$$u|_{t=0} = 0 \quad \text{and} \quad \tau_{rr}|_{t=0} = -P|_{t=0}. \qquad (6.27)$$

For the boundary data, we have that there is zero displacement at the centre of the bean, along with zero radial strain at the surface of the bean, which is equivalent to

$$u|_{r=0} = 0 \quad \text{and} \quad \left.\frac{\partial u}{\partial r}\right|_{r=L} = 0. \qquad (6.28)$$

6.2.7 Determining the Gas Pressure

In order to determine what deformations occur from the increasing gas pressure inside the bean, we must also determine the pressure P from other conservation equations. While we can use more complicated models that account for chemical reactions and additional gas species, such as the Sugar Pathway Model in Chapter 5, we will focus on a simpler (and better understood) model to highlight the effects of solid mechanics. In particular, we use the Modified Multiphase Model discussed in Section 4.3 to determine P and couple this to the poroviscoelastic equations. As we do not expect large deformations to occur in the bean before First Crack, we can neglect any advection caused by the moving cellulose. Finally, to observe a significant build-up of vapour pressure, we assign the gas permeability to $k_g = 10^{-16}$ m^2, which agrees with typical parameter values discussed in Chapters 4 and 5. We will now proceed to list the equations of the Modified Multiphase Model, along with their boundary conditions, together with the non-dimensional version of the poroviscoelastic equations in Section 6.3.

6.3 The Non-dimensionalised Poroviscoelastic Equations and Modified Multiphase Model

In order to better understand the governing conservation equations (6.22) and (6.26), we non-dimensionalise the variables such that

$$\begin{aligned} &P = \mathcal{P}\hat{P},\ \tau_{rr} = \mathcal{P}\hat{\tau},\ \Lambda = \frac{\lambda_1}{2}\hat{\Lambda},\ \xi = \frac{\xi_2}{2}\hat{\xi}, \\ &\Omega = \frac{2}{\xi_2}\hat{\Omega},\ r = L\hat{r},\ t = \vartheta\hat{t},\ \text{ and }\ u = \frac{L\mathcal{P}\vartheta}{\xi_2}\hat{u}. \end{aligned} \tag{6.29}$$

Here, the typical pressure $\mathcal{P}$ and timescale ϑ are identical to the values used in the non-dimensionalisation of the Modified Multiphase Model, i.e.

$$\mathcal{P} = D_1 P_0 \quad \text{and} \quad \vartheta = \frac{\phi\mu L^2}{k_{g0}\mathcal{P}}. \tag{6.30}$$

Combined with the additional poroviscoelastic equations (6.22) and (6.26), this gives the nondimensional equations (after dropping hats)

$$\frac{\partial \tau_{rr}}{\partial t} = -\frac{\partial P}{\partial t} + \mathrm{Wi}\,\Lambda\left[\frac{1}{\varsigma}\frac{\partial^2 u}{\partial t\partial r} + \frac{1}{r}\frac{\partial u}{\partial t} - (\tau_{rr}+P)\Omega\right], \tag{6.31}$$

$$\begin{aligned} &\frac{\partial^3 u}{\partial t\partial r^2} + \frac{\partial u}{\partial t\partial r}\left(\frac{1}{\Lambda}\frac{\partial \Lambda}{\partial r} + \frac{2}{r}\right) + \frac{1}{r}\frac{\partial u}{\partial t}\left(\frac{\varsigma}{\Lambda}\frac{\partial \Lambda}{\partial r} - \frac{2}{r}\right) \\ &\qquad = \frac{\varsigma}{\Lambda}\left[\frac{1}{\mathrm{Wi}}\frac{\partial^2 P}{\partial t\partial r} + (\tau_{rr}+P)\frac{\partial}{\partial r}(\Lambda\Omega) + \Lambda\Omega\frac{\partial P}{\partial r}\right], \end{aligned} \tag{6.32}$$

where the dimensionless functions are defined as

$$T_G(S) = \frac{\frac{T_{\text{dry}}}{T_0}\left(S + \frac{\rho_s(1-\phi)}{\rho_w\phi\sigma}\right)}{\frac{\rho_s(1-\phi)}{\rho_w\phi\sigma} + \frac{S}{Y^*}\left(\frac{T_{\text{dry}}}{T_0} - 1 + Y^*\right)}, \tag{6.33}$$

$$\Lambda = 2 - \varphi_1\left[1 + \tanh\left(\frac{1 + \mathscr{T}T - T_G}{\varphi_3}\right)\right], \tag{6.34}$$

$$\xi = 2 + \varphi_2\left[1 - \tanh\left(\frac{1 + \mathscr{T}T - T_G}{\varphi_3}\right)\right], \tag{6.35}$$

$$\Omega = \xi^{-1} - \frac{1}{\mathrm{Wi}\,\Lambda^2}\frac{\partial \Lambda}{\partial t}, \tag{6.36}$$

with

$$\mathrm{Wi} = \frac{\lambda_1\vartheta}{\xi_2}, \quad \varphi_1 = 1 - \frac{\lambda_2}{\lambda_1}, \quad \varphi_2 = \frac{\xi_1}{\xi_2} - 1, \quad \text{and} \quad \varphi_3 = \frac{T_{\text{crit}}}{T_0}. \tag{6.37}$$

The dimensionless parameter Wi is often referred to as the *Weissenberg number* [47], which relates the elastic forces in the cellulose to its viscous forces. Additionally, the dimensionless parameters φ_1 and φ_2 determine the relative changes in the Lamé coefficients and viscosities at the glass transition temperature, whereas φ_3 indicates how sharp the transition is. These non-dimensional poroviscoelastic equations (6.31)-(6.32) are coupled to the Modified Multiphase Model:

$$\frac{\partial S}{\partial t} = -\frac{1}{\epsilon^2} I_v, \tag{6.38}$$

$$\frac{\partial}{\partial t}\left[\frac{(1+\mathscr{T})P(1-\sigma S)}{1+\mathscr{T}T}\right] = -\frac{1}{\delta}\frac{\partial S}{\partial t} + \nabla \cdot \left[\frac{(1+\mathscr{T})P\nabla P}{1+\mathscr{T}T}\right], \tag{6.39}$$

$$\frac{\partial T}{\partial t} + \mathcal{A}_1 \frac{\partial}{\partial t}\left[S(1+\mathscr{T}T)\right] = \mathcal{A}_2 \frac{\partial S}{\partial t} + \mathcal{A}_3 \nabla \cdot \left[(1+\mathcal{A}_4 S)\nabla T\right], \tag{6.40}$$

where

$$I_v = S(1-\sigma S)(P_v^*(T,S) - P)\sqrt{\frac{1+\mathscr{T}}{1+\mathscr{T}T}} \tag{6.41}$$

and

$$P_v^*(T,S) = \frac{S^{C_1} \exp\left(\frac{D_2(T-1)}{1+\mathscr{T}T}\right)}{S^{C_1} + C_3}. \tag{6.42}$$

Additionally, our boundary conditions become

$$\frac{\partial T}{\partial r} = 0, \quad \frac{\partial P}{\partial r} = 0 \quad \text{at} \quad r = 0, \tag{6.43}$$

$$\frac{\partial T}{\partial r} = \nu \left(\frac{1-\sigma S}{1-\sigma}\right)\left(\frac{1+\mathcal{A}_4}{1+\mathcal{A}_4 S}\right)(1-T) \quad \text{at} \quad r = 1, \tag{6.44}$$

$$P\big|_{r=1} = \begin{cases} P_v^*(T,S), & T < T_a, \\ P_a, & T \geq T_a, \end{cases} \tag{6.45}$$

$$u|_{r=0} = 0 \quad \text{and} \quad \left.\frac{\partial u}{\partial r}\right|_{r=1} = 0. \tag{6.46}$$

Finally, our initial conditions are

$$S(r,0) = 1, \quad T(r,0) = 0, \quad P(r,0) = P_v^*(0,1), \quad u(r,0) = 0, \quad \text{and} \quad \tau_{rr}(r,0) = -P(r,0). \tag{6.47}$$

As we have assumed that advection due to the expanding coffee bean is negligible, the Modified Multiphase Model decouples from the poroviscoelastic equations. Therefore, for the remainder of this chapter, we will assume that T, S, and P have been determined independently of the poroviscoelastic equations and are then used as known functions when solving for τ_{rr} and u.

6.4 The Large Weissenberg Number Limit

Typical parameter values (as derived in Section 6.2.4) indicate that the Weissenberg number $\mathrm{Wi} \approx 5.5 \times 10^3$, so it is natural to perform an asymptotic analysis in the large Weissenberg number limit (LWNL). While there are several other nondimensional groupings that can play a role in determining leading-order dynamics (namely, φ_1, φ_2, and φ_3), we examine the LWNL in two specific cases: when φ_1, φ_2, and φ_3 are all $O(1)$, and when φ_2 is large.

6.4.1 The General LWNL

Firstly, we will consider the regime where all other dimensionless groupings in the poroviscoelastic equations (i.e. φ_1, φ_2, and φ_3) are $O(1)$. Physically speaking, this corresponds to when there is no dramatic change in Lamé coefficients and viscosities at the glass transition temperature, nor does this transition occur too rapidly. By taking the asymptotic expansions in the limit $\mathrm{Wi}^{-1} \to 0$

$$u(r,t) = u_0(r,t) + O(\mathrm{Wi}^{-1}), \qquad \tau_{rr}(r,t) = \mathcal{T}_0(r,t) + O(\mathrm{Wi}^{-1}), \tag{6.48}$$

our leading order equations for (6.31) and (6.32) become

$$\frac{1}{\varsigma}\frac{\partial^2 u_0}{\partial t \partial r} + \frac{1}{r}\frac{\partial u_0}{\partial t} = \frac{\mathcal{T}_0 + P}{\xi}, \tag{6.49}$$

$$\frac{\partial^3 u_0}{\partial t \partial r^2} + \frac{\partial u_0}{\partial t \partial r}\left(\frac{1}{\Lambda}\frac{\partial \Lambda}{\partial r} + \frac{2}{r}\right) + \frac{1}{r}\frac{\partial u_0}{\partial t}\left(\frac{\varsigma}{\Lambda}\frac{\partial \Lambda}{\partial r} - \frac{2}{r}\right) = \varsigma\left[\left(\frac{\mathcal{T}_0 + P}{\Lambda}\right)\frac{\partial}{\partial r}\left(\frac{\Lambda}{\xi}\right) + \frac{1}{\xi}\frac{\partial P}{\partial r}\right]. \tag{6.50}$$

By substituting (6.49) into (6.50), we obtain a single PDE determining u_0 based on predetermined functions ξ and P:

$$\frac{\partial^3 u_0}{\partial t \partial r^2} + \frac{\partial u_0}{\partial t \partial r}\left(\frac{1}{\xi}\frac{\partial \xi}{\partial r} + \frac{2}{r}\right) + \frac{1}{r}\frac{\partial u_0}{\partial t}\left(\frac{\varsigma}{\xi}\frac{\partial \xi}{\partial r} - \frac{2}{r}\right) = \frac{\varsigma}{\xi}\frac{\partial P}{\partial r}. \tag{6.51}$$

In particular, if we assume that ξ does not change at the glass transition temperature (which, in our non-dimensional equations, corresponds to assuming that $\varphi_2 = 0$ and $\xi \equiv 2$) with no other restriction on parameter space, our leading order equations become

$$\frac{\partial}{\partial r}\left[\frac{1}{r^2}\frac{\partial}{\partial r}\left(r^2\frac{\partial u_0}{\partial t}\right)\right] = \frac{\varsigma}{2}\frac{\partial P}{\partial r}, \tag{6.52}$$

which corresponds to the poroviscoelastic equations with constant Lamé coefficients as seen in [24]. By imposing the boundary conditions (6.46), we can solve (6.49) and (6.52), which yields

$$\begin{aligned} u_0(r,t) &= \frac{\varsigma}{2r^2}\int_0^t\int_0^r \left[P(\chi,s) - A(s)\right]\chi^2\,\mathrm{d}\chi\,\mathrm{d}s, \\ \mathcal{T}_0(r,t) &= \frac{\varsigma - 1}{r^3}\int_0^r \left[P(\chi,t) - A(t)\right]\chi^2\,\mathrm{d}\chi - A(t), \end{aligned} \tag{6.53}$$

where

$$A(t) = 3\left.P\right|_{r=1} - 6\int_0^1 P(\chi,t)\chi^2\,\mathrm{d}\chi. \tag{6.54}$$

Therefore, this indicates that having Λ non-constant does not affect the leading-order poroviscoelastic equations in the general LWNL. However, different leading-order behaviour is observed if φ_2 is large.

6.4.2 The Large φ_2 LWNL

If we have a large difference between ξ_1 and ξ_2 viscosities, this will be represented by a large value of φ_2. The leading-order behaviour of the LWNL poroviscoelastic equations can be expected to change for sufficiently large values of φ_2, e.g. $\varphi_2 = \mathrm{Wi}^{\alpha}$. There is a distinguished limit when $\alpha = 1$ (which we will discuss later in this section), which naturally divides the parameter regime into two main regions: $0 < \alpha < 1$ and $\alpha > 1$. We will now discuss these three regions in greater detail.

Firstly, $0 < \alpha < 1$ corresponds to the viscous stresses being small below the glass transition temperature, which in turn implies that $u \ll 1$ when $1 + \mathscr{T}T < T_G$. In this regime, we take the asymptotic expansions in the limit $\mathrm{Wi}^{-\alpha} \to 0$ to be

$$u(r,t) = \mathrm{Wi}^{-\alpha}U_0(r,t) + O(\mathrm{Wi}^{-2\alpha}), \qquad \tau_{rr}(r,t) = \mathcal{T}_0(r,t) + O(\mathrm{Wi}^{-\alpha}). \tag{6.55}$$

The leading order terms of (6.31) and (6.32) then reduce to nearly the same PDE framework as in the non-degenerate LWNL: namely,

$$\frac{\partial^3 U_0}{\partial t\partial r^2} + \frac{\partial U_0}{\partial t\partial r}\left(\frac{1}{\Xi}\frac{\partial \Xi}{\partial r} + \frac{2}{r}\right) + \frac{1}{r}\frac{\partial U_0}{\partial t}\left(\frac{\varsigma}{\Xi}\frac{\partial \Xi}{\partial r} - \frac{2}{r}\right) = \frac{\varsigma}{\Xi}\frac{\partial P}{\partial r}, \tag{6.56}$$

where the rescaled viscosity Ξ is defined as

$$\Xi = 1 - \tanh\left(\frac{1+\mathscr{T}T - T_G}{\varphi_3}\right). \tag{6.57}$$

The distinguished limit $\alpha = 1$ corresponds to the inclusion of temporal stress terms in (6.31) and (6.32) in the leading-order equations. Therefore, for $\varphi_2 = C\mathrm{Wi}$ and $C = O(1)$ (i.e. $\alpha = 1$), our leading order equations for (6.31) and (6.32), for $1 + \mathscr{T}T < T_G$, become

$$\frac{\partial \mathcal{T}_0}{\partial t} = -\frac{\partial P}{\partial t} + \Lambda\left[\frac{1}{\varsigma}\frac{\partial^2 U_0}{\partial t \partial r} + \frac{1}{r}\frac{\partial U_0}{\partial t} - (\mathcal{T}_0 + P)\left(\Xi^{-1} - \frac{1}{\Lambda^2}\frac{\partial \Lambda}{\partial t}\right)\right], \tag{6.58}$$

$$\begin{aligned}\frac{\partial^3 U_0}{\partial t \partial r^2} &+ \frac{\partial U_0}{\partial t \partial r}\left(\frac{1}{\Lambda}\frac{\partial \Lambda}{\partial r} + \frac{2}{r}\right) + \frac{1}{r}\frac{\partial U_0}{\partial t}\left(\frac{\varsigma}{\Lambda}\frac{\partial \Lambda}{\partial r} - \frac{2}{r}\right)\\ &= \varsigma\left[\frac{1}{\Lambda}\frac{\partial^2 P}{\partial t \partial r} + \left(\frac{\mathcal{T}_0 + P}{\Lambda}\right)\frac{\partial}{\partial r}\left(\frac{\Lambda}{\Xi} - \frac{1}{\Lambda}\frac{\partial \Lambda}{\partial t}\right) + \left(\Xi^{-1} - \frac{1}{\Lambda^2}\frac{\partial \Lambda}{\partial t}\right)\frac{\partial P}{\partial r}\right],\end{aligned} \tag{6.59}$$

where

$$\Xi = C\left[1 - \tanh\left(\frac{1+\mathscr{T}T - T_G}{\varphi_3}\right)\right]. \tag{6.60}$$

As these leading-order equations are not great simplifications of (6.31) and (6.32), the main conclusion from this distinguished limit regime is that deformations for $1 + \mathscr{T}T < T_G$ are negligible in comparison to the $O(1)$ deformations that occur when $1 + \mathscr{T}T > T_G$ (i.e. $\xi \sim 2$), which reduces to equation (6.53) from the non-degenerate LWNL.

Finally, in the parameter regime when $\alpha > 1$, we have that

$$\Omega \sim -\frac{1}{\mathrm{Wi}\,\Lambda^2}\frac{\partial \Lambda}{\partial t}, \tag{6.61}$$

implying that ξ no longer plays a leading-order role in Ω, which continues to be $O(\mathrm{Wi}^{-1})$. Therefore, we use the same rescalings of u and τ_{rr} as in other ranges of α, implying that the leading-order equations for (6.31) and (6.32), for $1 + \mathscr{T}T < T_G$, become

$$\frac{\partial \mathcal{T}_0}{\partial t} = -\frac{\partial P}{\partial t} + \Lambda\left[\frac{1}{\varsigma}\frac{\partial^2 U_0}{\partial t \partial r} + \frac{1}{r}\frac{\partial U_0}{\partial t} - (\mathcal{T}_0 + P)\hat{\Omega}\right], \tag{6.62}$$

$$\begin{aligned}\frac{\partial^3 U_0}{\partial t \partial r^2} &+ \frac{\partial U_0}{\partial t \partial r}\left(\frac{1}{\Lambda}\frac{\partial \Lambda}{\partial r} + \frac{2}{r}\right) + \frac{1}{r}\frac{\partial U_0}{\partial t}\left(\frac{\varsigma}{\Lambda}\frac{\partial \Lambda}{\partial r} - \frac{2}{r}\right)\\ &= \varsigma\left[\frac{1}{\Lambda}\frac{\partial^2 P}{\partial t \partial r} + \left(\frac{\mathcal{T}_0 + P}{\Lambda}\right)\frac{\partial}{\partial r}\left(\Lambda\hat{\Omega}\right) + \hat{\Omega}\frac{\partial P}{\partial r}\right],\end{aligned} \tag{6.63}$$

where

$$\hat{\Omega} = -\frac{1}{\Lambda^2}\frac{\partial \Lambda}{\partial t}. \tag{6.64}$$

Again, these leading-order equations are not great simplifications of (6.31) and (6.32). The main conclusions from the regime, when $\alpha > 1$, are that the dimensionless function Ω continues to be $O(\mathrm{Wi}^{-1})$, but no longer depends on the viscosity ξ at leading order, and that deformations for $1+\mathscr{T}T < T_G$ are still negligible in comparison to the $O(1)$ deformations that occur when $1 + \mathscr{T}T > T_G$.

6.5 Numerical Results

We solve the poroviscoelastic equations, equations (6.31) and (6.32), coupled with the Modified Multiphase Model, equations (6.38)-(6.47), in MATLAB using a second-order finite difference scheme in the spatial component and a stiff ODE solver for the time component (namely, the MATLAB function `ode23s`). We used 101 spatial meshpoints to achieve good numerical resolution.

Firstly, we examine the parameter regime when $\varphi_1 = 0.25$ and $\varphi_2 = 0$, in order to explore the effects of a temperature-dependent Lamé coefficient with constant viscosity. As we see in Figure 6.1, we observe that the radial component of the effective material stress, τ_{rr}^E, is qualitatively similar to the vapour pressure, P. Indeed, the difference between these two quantities is identically τ_{rr}, which we observe to have values about a quarter the size of the vapour pressure. Additionally, we note that the glass transition temperature, $T_G(S)$, first occurs in the interior of the bean before propagating towards the surface and centre. This results from the fact that the glass transition temperature is easier to achieve in areas of higher moisture content; therefore, this specific configuration of the glass transition curve in time and space is the result of a balance between moisture loss and temperature increase within the bean.

We also observe that the displacement, u, attains a maximal value of about 250mm in a 500 s roast (Figure 6.2(a)). These large displacements are due to a combination of small gas permeability and viscosity values. In reality, the total gas pressure would include CO_2 and non-reacting gases, which would allow for a build-up of total gas pressure at larger gas permeabilities and viscosities. These larger parameter values would, in turn, decrease the typical displacement lengthscale. $\frac{L\mathcal{P}\vartheta}{\xi_2}$, while keeping the pressure gradient, $\frac{\partial P}{\partial r}$, the same.

Nevertheless, we can use the displacement u to compare the temperature-dependent

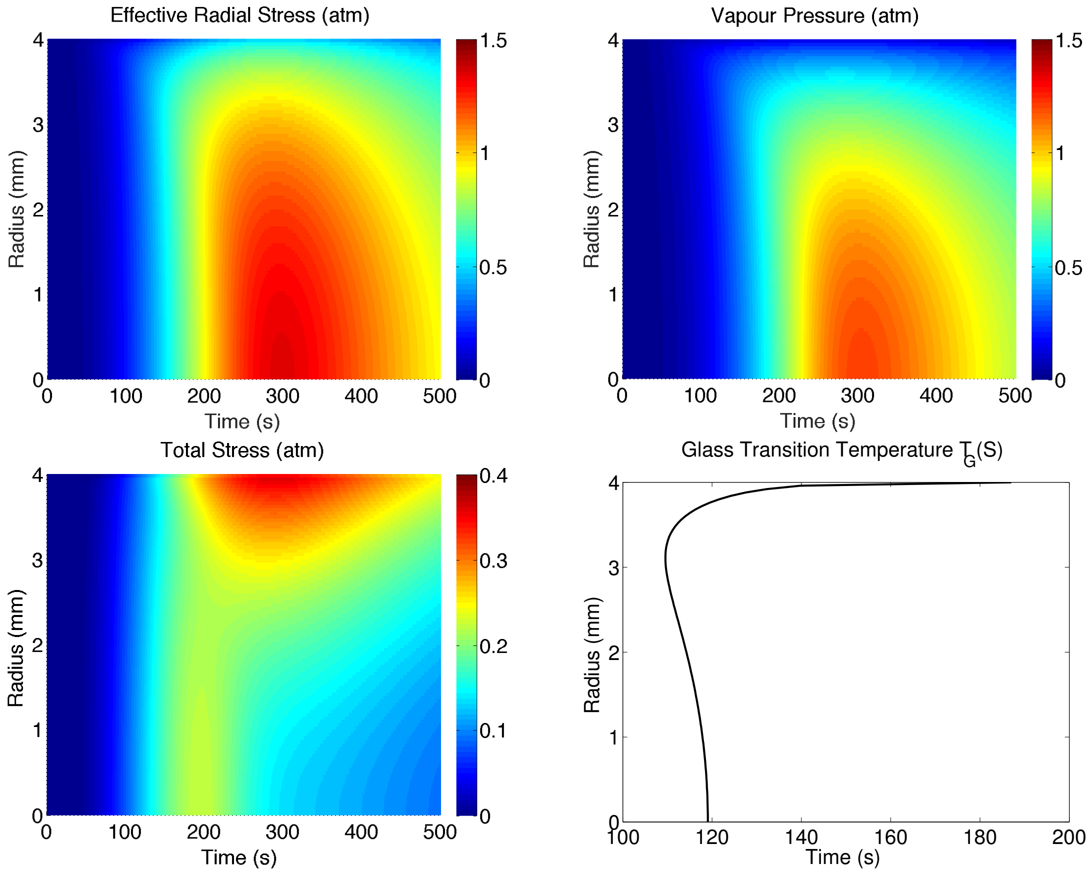

Figure 6.1: The solutions of the poroviscoelastic equations, coupled with the Modified Multiphase Model (4.39)-(4.48), for the first 500 seconds of a 230°C roast, with $\varphi_1 = 0.25$ and $\varphi_2 = 0$. The glass transition temperature $T_G(S)$ first occurs in the interior of the bean before propagating towards the surface and centre.

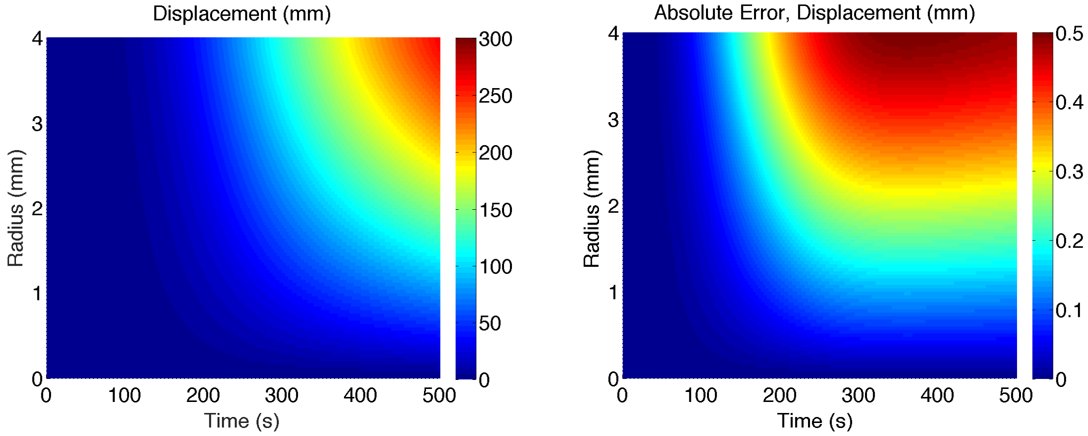

(a) (b)

Figure 6.2: The radial displacement $u(r,t)$ of the poroviscoelastic equations, with (a) the temperature-dependent Lamé coefficient ($\varphi_1 = 0.25, \varphi_2 = 0$) and (b) the absolute error $|u(r,t) - u_0(r,t)|$, where $u_0(r,t)$ is the leading-order approximation in the large Weissenberg number limit determined via equation (6.53).

Lamé coefficient with the large Weissenberg number limit (LWNL) asymptotic approximation (6.53). With a maximum absolute error of 0.5mm (Figure 6.2(b)), we conclude that the LWNL asymptotic expansion (i.e. the constant Λ approximation) is a good approximation for the leading-order behaviour of the solutions to the poroviscoelastic equations.

Knowing now that a temperature-dependent Lamé coefficient displays the same leading-order behaviour as its constant coefficient approximation, we now examine the parameter regime when $\varphi_1 = 0$ and φ_2 is non-zero to explore the effects of a temperature-dependent viscosity. Numerical difficulties are observed for sharp sigmoidal behaviour in viscosities, e.g. smaller values of φ_3 smaller than 0.04, corresponding to $T_{\text{crit}} < 10°\text{C}$. In order to avoid these numerical difficulties, we relax this sharp transition and take $\varphi_3 \approx 0.09$, corresponding to $T_{\text{crit}} = 25°\text{C}$. With reference to Figure 6.3, we find that the displacement is smaller below the glass transition temperature than the constant viscosity parameter regime, which is to be expected. However, as seen in Figure 6.4, a large spike in radial stress occurs as the glass transition temperature reaches the surface of the bean, which is a phenomenon not seen in previous parameter regimes. This surge of stress (which begins after the glass transition first occurs in the interior of the bean) is caused by a thin region near the coffee bean's surface being far more rigid that its viscous interior. Once the glass transition has occurred at the surface of the bean, the viscosity of the cellulose is approximately uniform throughout the bean and dissipates the build-up of stress via

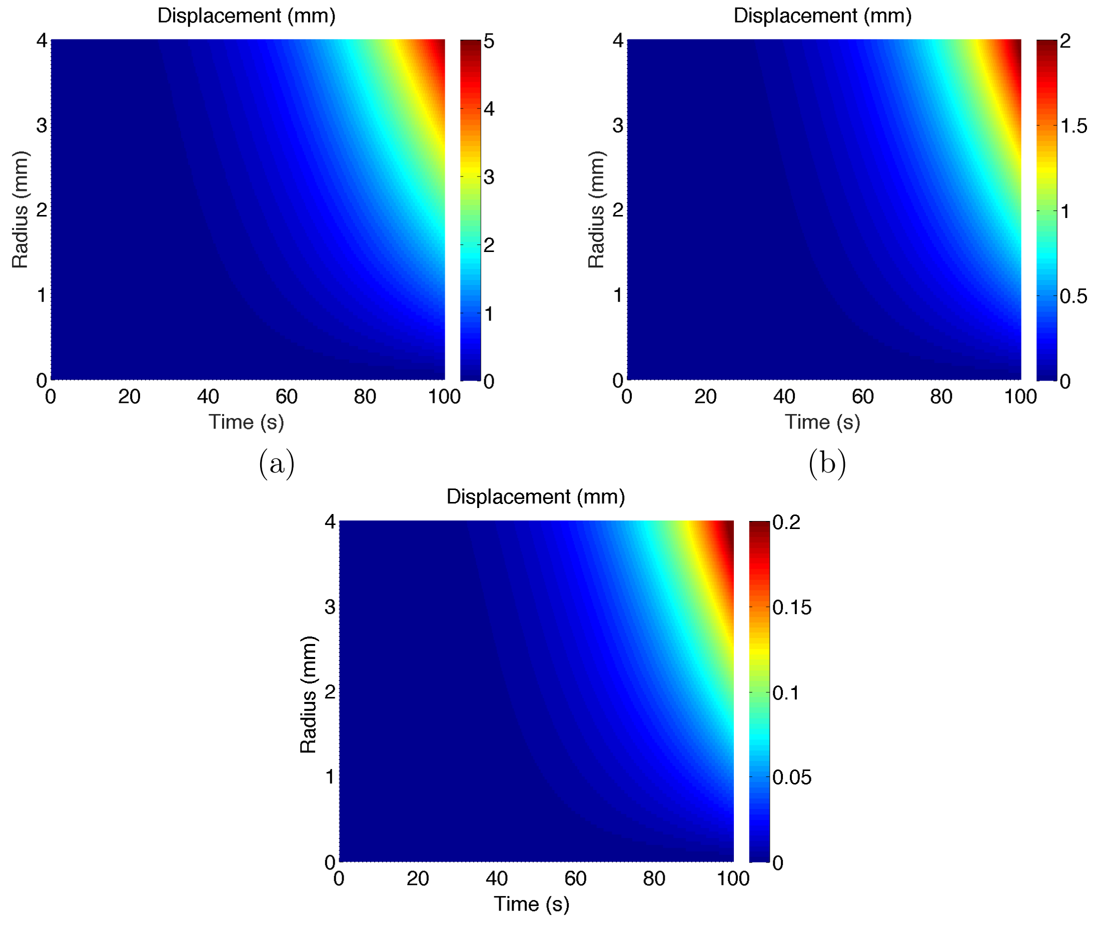

(a) (b)

(c)

Figure 6.3: The radial displacement $u(r,t)$ of the poroviscoelastic equations, with $\varphi_1 = 0$ and temperature-dependent viscosity ξ, with (a) $\varphi_2 = 0$, (b) $\varphi_2 = 9$, and (c) $\varphi_2 = 99$.

the deformation of the cellulose. This indicates that mechanical failure in the solid structure, yielding phenomena such as First Crack, could be strongly linked to this surge of stress just as the glass transition approaches the surface of the bean.

The temperature-dependent viscosity regime therefore indicates that macro-scale fracturing in a roasting coffee bean can be controlled by determining when the glass transition temperature occurs at the surface of the bean. This is equivalent to changing where the temperature-moisture pair $(S^*, T_G(S^*))$ occurs, which can be done in several ways; we give two simple suggested modifications. The first possible modification is to change the convective heat coefficient at the surface of the bean (contained in the non-dimensional grouping ν) so that the effective thermal timescale of the problem is changed. Similarly, one could change the roasting temperature (reflected in the non-dimensional grouping $\mathscr{T}$) so that the glass transition temperature occurs

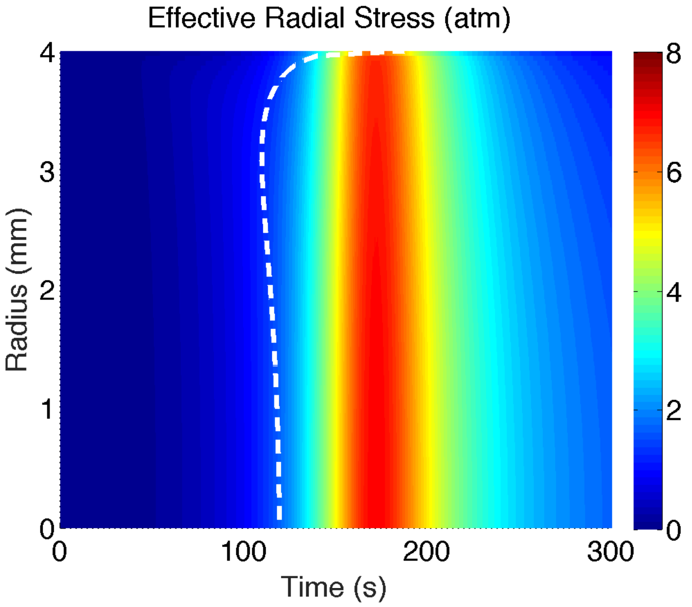

Figure 6.4: The effective radial material stress $\tau^E_{rr}(r,t)$ of the poroviscoelastic equations, with $\varphi_1 = 0$ and $\varphi_2 = 9$. A large build-up of stress is observed when the glass transition temperature (white dashed curve) approaches the surface of the bean.

for a different moisture value. In either case, modifying the roasting environment of the bean allows for the glass transition temperature to occur at different times and positions in the bean, changing when First Crack occurs.

The temperature-dependent viscosity regime also gives insight into how large the dimensionless grouping φ_2 might be. As previously discussed, macro-scale fracturing occurs at the onset of the glass transition temperature. Additionally, we know that the displacement in the large φ_2 LWNL has a similar displacement value to the constant poroviscoelastic equations (6.53), divided by a factor of φ_2. Therefore, knowing how far the surface of the bean has been displaced just before First Crack, as well as what displacements are expected from (6.53), yields a ratio linked to φ_2. For example, if (6.53) yields a displacement of 5mm at the onset of First Crack, while experimentally determined to be 0.5mm, this would tell us that $\varphi_2 \approx \frac{5}{0.5} = 10$.

6.6 Discussion

In this chapter, we have explored the role of deformations in the solid cellulose structure of a roasting coffee bean. Specifically, we modelled the cellulose structure in the bean as a poroviscoelastic Maxwell material with temperature-dependent Lamé coefficients and viscosities. These parameters crucially depend on a moisture-dependent glass transition temperature, which signals the transition between a predominantly poroelastic material at low temperatures to a poroviscoelastic material at high temperatures. The governing poroviscoelastic equations are then coupled to the Modified Multiphase Model to determine the temperature, water saturation, and vapour pressure within the bean, and are then used as input variables to determine the radial stress and displacement of the bean. With a suitable non-dimensionalisation, we find that the poroviscoelastic equations crucially depend on the Weissenberg number, which relates the ratio of elastic forces to viscous forces. Typical parameter values indicate that the Weissenberg number is very large, which allowed us to determine the leading-order equations for radial stress and displacement via asymptotic analysis. In particular, the leading-order poroviscoelastic equations do not depend on the variability of Lamé coefficients, which is confirmed by numerical solutions of the equations. Additionally, we find that if the viscosity of the material changes significantly at the glass transition temperature, a large build-up of stress occurs, which can signal the onset of macro-scale deformations such as First Crack. Therefore, by controlling where the glass transition temperature occurs in time and space (say, by modifying the roasting temperature or convective heat transfer coefficient at the bean's surface), we can control when First Crack occurs in a particular roast.

Chapter 7

Conclusions and Future Work

7.1 General Discussion

In this thesis, we studied, from a mathematical perspective, the physical and chemical processes that arise as a coffee bean is roasted. By examining the changing structure of coffee beans during a roast, we concluded that a mathematical model incorporating multiphase heat and mass transfer processes is an appropriate way to describe the phenomena that are observed. Our modelling approach is motivated by models that arise in other food engineering applications (cf. [13, 61]), and is an extension of existing literature which consists of regression analyses and simple empirical models used to interpret experimental data (see e.g. [2, 51, 60]).

Once heat and mass transfer models were derived and suitably non-dimensionalised, numerical results of one particular model indicated that a "drying front", propagating from the surface of the bean to the centre of the bean, divides the coffee bean into a moist and a dry region. We were then motivated to use asymptotic analysis to determine the leading-order behaviour of the temperature, vapour pressure, water saturation, and motion of the drying front. As the asymptotic structure crucially relies on the form of the evaporation rate used in the multiphase model, various other evaporation rates, including ones employing a sorption isotherm, were considered and compared.

Extensions to these heat and mass transfer models were considered in order to gain insight into the qualitative behaviour of various chemical and physical processes during roasting. In particular, we derived a model that incorporates a simplified sugar chemical pathway for specific chemical components in the bean and introduced global reaction rates that account for the distribution of activation energies of the chemical reactions. Other spherically symmetry geometries beyond a solid sphere were also considered, motivated by experiments which suggested that one should model a coffee bean chunk differently to a whole coffee bean. Lastly, the mechanical properties of the solid phase were examined to model the deformations and stresses that occur during roasting.

7.2 Findings and Conclusions

7.2.1 Chapter 2

By deriving a model from first principles that incorporates multiphase flow (the Local Moisture Model), as well as heat and mass transfer, we were able to extend ideas presented in [13]. More specifically, by solving a simplified version of the Local Moisture Model (the Multiphase Model), we determined that this model can indeed be fit to existing experimental data. Additionally, numerical issues that can be seen in the model motivated from [13] (the Bulk Moisture Model) were not observed in the Multiphase Model. Moreover, we concluded that while both models can fit experimental data concerning the average moisture content within a coffee bean as it is roasted, the predicted local moisture content within a bean is significantly different between these two models. This is mainly driven by the fact that the authors in [13] rely on bulk moisture content, rather than on local moisture content, to determine the dynamics of evaporation within the coffee bean. Therefore, the multiphase models presented in Chapter 2 provide greater insight into the local phenomena that occur as a coffee bean is roasted.

7.2.2 Chapter 3

In Chapter 3, we studied solutions of the Multiphase Model via asymptotic methods, in order to better understand important qualitative features of the coffee bean roasting process. Motivated by previous numerical results, we considered the limit where the rate of vapour transport by Darcy flow is much smaller than the evaporation rate. The asymptotic analysis showed that the solution could be divided into two main regions and a transition layer. The entire bean was in the first region until a critical time, t^*, when a thin transition layer appeared at the surface of the bean. This transition layer then propagated into the bean creating a second main region between it and the surface of the bean. In the first region, the vapour pressure is in equilibrium with the steam table pressure and the moisture content of the bean remains at its initial value, with heat flow governed by the heat equation. In the thin transition region, the moisture content changes rapidly from its initial value to a small value. Here, evaporation dominates and the temperature and vapour pressure remain spatially uniform. Finally, in the second main region, there is almost no water and therefore no evaporation. The problem in this second region consists of diffusion equations for the heat and vapour flow with coupling through the matching conditions, similar to a Stefan problem, at the transition layer.

Numerical simulations suggested that the externally applied roasting temperature is attained fairly quickly; hence, the case where temperature is fixed at the roasting temperature was considered. This also allowed the coupled Stefan-like problem to be reduced to a single Stefan-like problem, which could then be solved via similarity solutions or large Stefan number asymptotics. The leading order expressions were shown to agree well with the dynamics of the drying front found from numerical simulations, under both spherical and planar geometries.

7.2.3 Chapter 4

In Chapter 4, we examined how various models for evaporation rates affect the predicted moisture loss inside a roasting bean. Specifically, by utilising the asymptotic framework discussed in Chapter 3, we determined that evaporation rates which can be written as a product of two functions (one depending only on saturation and one depending only on vapour pressure) share the same asymptotic features in the two main regions of the bean as previously shown. In the thin transition layer, these separable evaporation rates yield the same Stefan-like condition that determines the drying front, but display slightly different dynamics in the water content. However, since the transition layer is very thin, these separable evaporation rates do not drastically change the overall qualitative behaviour of the Multiphase Model.

We also further examined how evaporation is affected by deviation of vapour pressure from an equilibrium vapour pressure of the bound water: namely, by considering the sorption isotherm of the material. This sorption isotherm modifies the steam table pressure used in the Multiphase Model, with the result that the equilibrium vapour pressure becomes a function of temperature and water saturation. Using similar asymptotic analysis techniques as those presented in Chapter 3, we determined that, at leading order, the vapour pressure never deviates from its sorption isotherm, as the external vapour pressure boundary condition is now satisfied by the sorption isotherm. In consequence, there is no “drying front” or secondary dry region observed when the sorption isotherm is incorporated into the Multiphase Model.

Additionally, the incorporation of the sorption isotherm significantly increases the time for a coffee bean to dry out, while decreasing the maximal vapour pressure experienced in the bean. When compared to numerical results, we determined that the bean's maximal vapour pressure is approximately proportional to the reciprocal square-root of the gas permeabilities in the range relevant to similar organic materials, such as wood. While this approximate relationship is simplistic, it allows us to infer what magnitudes of vapour pressures can be expected for a range of gas permeabilities, which is crucial when incorporating additional features into these multiphase models. While the multiphase framework in earlier models (such as those discussed in Chapters 2 and 3) allows for the modelling of the bean's local moisture content, the incorporation of the sorption isotherm in said multiphase models allows for a much better representation of the moisture loss of a roasting coffee bean.

7.2.4 Chapter 5

In Chapter 5, we incorporated modified evaporation rates (discussed in Chapter 4) and chemical reaction groups to allow predictions of flavour development in a roasting coffee bean. These additions were motivated both by the inability of previous mathematical models (such as those presented in Chapters 2 and 3) to reproduce experimental data at different length scales, as well as to remedy some physically unrealistic parameter values. In particular, the "chopped green coffee bean" thought experiment discussed in Chapter 2 was carried out and the resulting experimental data compared with predictions.

By assuming that a chemical reaction group has a distribution of activation energies, the new evaporation rate had a *global* reaction rate. These ideas were then used to model a simplified sugar pathway network relevant to flavour development. Modelling this pathway also required us to model the transport of gases other than water vapour (in this case, CO_2 and air) within the bean, as well as the energy produced or consumed during these additional chemical reactions.

Finally, a spherically symmetric shell geometry was proposed to be a more appropriate representation of a whole coffee bean than a solid sphere. We also considered that chunks of bean, as used in the chopped bean experiment, are adequately represented by solid spheres. With the incorporation of this new geometry for a whole coffee bean, we were able to accurately capture the differences in moisture loss seen in the "chopped green coffee bean" experiment. A sensitivity analysis shows how various non-dimensional groupings, whose values are not known in the literature, affect the temperature and moisture profiles of a roasting coffee bean.

7.2.5 Chapter 6

In Chapter 6, we examined how the build-up of gas pressure affects the mechanical properties of the cellulose structure within a coffee bean. We modelled the cellulose structure as a poroviscoelastic material with temperature-dependent parameters: namely, the Lamé coefficients and viscosities, which are assumed to change significantly at a saturation-dependent glass transition temperature. These poroviscoelastic equations are then coupled with the Modified Multiphase Model discussed in Chapter 4, in order to determine the pressure gradient in the cellulose material.

The poroviscoelastic equations are then non-dimensionalised, where typical parameter values indicate that the elastic forces in the cellulose are significantly smaller than its viscous forces (i.e. the large Weissenberg number limit). Asymptotic analysis in this limit indicated that, at leading order, the temperature-dependency of the Lamé coefficients do not affect the poroelastic equations, which is confirmed by numerical simulations of the poroviscoelastic equations. However, we also showed that having a temperature-dependent viscosity significantly changes the stresses within the bean. Specifically, if the transition in viscosity values at the glass transition temperature is too large or too steep, a surge of stress occurs when the glass transition temperature reaches the surface of the bean. This surge of stress results from a thin region near the bean's surface being far more rigid that its viscous interior, which may be linked to macro-scale deformations in the bean (such as First Crack). Therefore, controlling when the glass transition temperature reaches the surface of the bean could, in turn, allow one to control these macro-scale deformations in order to prevent or slow fracturing within the bean.

7.3 Future Work

It is no surprise that there are many aspects of coffee bean roasting that have not been considered in our work. Many parameter values in our models were unknown in the literature and therefore were used to fit results to experimental data. Further experimental work, especially concerning values used in the Sugar Pathway Model of Chapter 5, would allow a considerable reduction of uncertainty in the parameter regime. Additionally, further experimental data to determine the gas permeability of a roasting coffee bean could prove useful in providing accurate and quantitative results for moisture and gas transport with the bean. The sorption isotherm, which is also responsible for moisture and vapour transport, crucially depends on the choice of model used to relate water activity to moisture content. Examining various other forms of water activity functions, along with how they affect the sorption isotherm and moisture transport, could also aid in fine-tuning our multiphase models.

Along with the lack of certain experimentally-determined parameters used in these multiphase models, additional modelling could be carried out for the coffee bean roasting process. One large assumption we have used throughout was that the bean can be modelled via a spherically symmetric geometry. In the future, more complicated geometries that accurately reflect the true shape of a coffee bean might be used when employing these multiphase models. Through the use of a commercial FEM package, various other simplifications used in these models might also be relaxed, including (but not limited to): modelling the anisotropic nature of the solid cellulose structure, advection due to gas transport and deformations, more complex distributions used in chemical reaction groups, failure criteria and fracturing mechanics during First Crack, and the incorporation of other diffusive processes not considered in these models. Finally, it is important to note that all of these multiphase models are to describe the roasting of a single bean. One may need to employ homogenisation or other multi-particle modelling techniques in order to study an array of roasting beans.

Bibliography

[1] B. A. Anderson, E. Shimoni, R. Liardon, and T. P. Labuza. The diffusion kinetics of carbon dioxide in fresh roasted and ground coffee. *Journal of Food Engineering*, 59(1):71–78, 2003.

[2] J. Baggenstoss. *Coffee roasting and quenching technology - Formation and stability of aroma compounds.* PhD thesis, Swiss Federal Institute of Technology, 2008.

[3] R. B. Bird, W. E. Stewart, and E. N. Lightfoot. *Transport Phenomena.* John Wiley & Sons, New York, 1960.

[4] A. G. W. Bradbury and D. J. Halliday. Chemical structures of green coffee bean polysaccharides. *Journal of Agricultural and Food Chemistry*, 38(2):389–392, 1990.

[5] V. Chandrasekar and R. Viswanathan. Physical and thermal properties of coffee. *Journal of Agricultural Engineering Research*, 73(3):227–234, 1999.

[6] J. Chen, K. Pitchai, S. Birla, M. Negahban, D. Jones, and J. Subbiah. Heat and mass transport during microwave heating of mashed potato in domestic oven–model development, validation, and sensitivity analysis. *Journal of Food Science*, 79(10), 2014.

[7] A. B. Comsol. Comsol multiphysics users guide, Version: September 2005.

[8] G. L. Comstock. Directional permeability of softwoods. *Wood and Fiber Science*, 1(4):283–289, 2007.

[9] P. C. Corrêa, A. L. D. Goneli, P. C. A. Junior, G. H. H. De Oliveira, and D. S. M. Valente. Moisture sorption isotherms and isosteric heat of sorption of coffee in different processing levels. *International Journal of Food Science & Technology*, 45(10):2016–2022, 2010.

[10] J. A. Dean. *Lange's Handbook of Chemistry, 15th Ed.* McGraw-Hill, New York, 1999.

[11] A. Dhall, A. Halder, and A. K. Datta. Multiphase and multicomponent transport with phase change during meat cooking. *Journal of Food Engineering*, 113(2):299–309, 2012.

[12] G. Eggleston, B. J. Trask-Morrell, and J. R. Vercellotti. Use of differential scanning calorimetry and thermogravimetric analysis to characterize the thermal degradation of crystalline sucrose and dried sucrose- salt residues. *Journal of Agricultural and Food Chemistry*, 44(10):3319–3325, 1996.

[13] A. Fabbri, C. Cevoli, L. Alessandrini, and S. Romani. Numerical modeling of heat and mass transfer during coffee roasting process. *Journal of Food Engineering*, 105(2):264–269, 2011.

[14] N. T. Fadai, Z. Akram, F. Guilmineau, J. Melrose, C. P. Please, and R. A. Van Gorder. The influence of distributed chemical reaction groups in a multiphase coffee bean roasting model. *IMA Journal of Applied Mathematics*, 2018.

[15] N. T. Fadai, J. Melrose, C. P. Please, A. Schulman, and R. A. Van Gorder. A heat and mass transfer study of coffee bean roasting. *International Journal of Heat and Mass Transfer*, 104:787–799, 2017.

[16] N. T. Fadai, C. P. Please, and R. A. Van Gorder. Asymptotic analysis of a multiphase drying model motivated by coffee bean roasting. *SIAM Journal on Applied Mathematics*, 78(1):418–436, 2018.

[17] S. E. Fayle and J. A. Gerrard. *The Maillard Reaction*, volume 5. Royal Society of Chemistry, 2002.

[18] A. Fick. On liquid diffusion. *Philosophical Magazine Series 4*, 10(63):30–39, 1855.

[19] L. J. Gibson and M. F. Ashby. *Cellular solids: structure and properties.* Cambridge University Press, 1999.

[20] M. Ginz, H. H. Balzer, A. G. W. Bradbury, and H. G. Maier. Formation of aliphatic acids by carbohydrate degradation during roasting of coffee. *European Food Research and Technology*, 211(6):404–410, 2000.

[21] A. N. Gloess, A. Vietri, F. Wieland, S. Smrke, B. Schönbächler, J. A. Sánchez López, S. Petrozzi, S. Bongers, T. Koziorowski, and C. Yeretzian. Evidence of different flavour formation dynamics by roasting coffee from different origins: On-line analysis with ptr-tof-ms. *International Journal of Mass Spectrometry*, 365:324–337, 2014.

[22] A. Halder, A. Dhall, and A. K. Datta. Modeling transport in porous media with phase change: applications to food processing. *Journal of Heat Transfer*, 133(3):031010, 2011.

[23] W. N. Hernández-Díaz, I. I. Ruiz-López, M. A. Salgado-Cervantes, G. del C. Rodríguez-Jimenes, and M. A. García-Alvarado. Modeling heat and mass transfer during drying of green coffee beans using prolate spheroidal geometry. *Journal of Food Engineering*, 86(1):1–9, 2008.

[24] P. Howell, G. Kozyreff, and J. Ockendon. *Applied Solid Mechanics*, volume 43. Cambridge University Press, 2009.

[25] C. T. Hsu and P. Cheng. Thermal dispersion in a porous medium. *International Journal of Heat and Mass Transfer*, 33(8):1587–1597, 1990.

[26] H. Huang, P. Lin, and W. Zhou. Moisture transport and diffusive instability during bread baking. *SIAM Journal on Applied Mathematics*, 68(1):222–238, 2007.

[27] M. Kaseem, K. Hamad, J. H. Park, and Y. G. Ko. Rheological properties of abs/wood composites. *European Journal of Wood and Wood Products*, 73(5):701–703, 2015.

[28] E. K. Kemsley, S. Ruault, and R. H. Wilson. Discrimination between coffea arabica and coffea canephora variant robusta beans using infrared spectroscopy. *Food Chemistry*, 54(3):321–326, 1995.

[29] B. Krupińska, I. Strømmen, Z. Pakowski, and T. M. Eikevik. Modeling of sorption isotherms of various kinds of wood at different temperature conditions. *Drying Technology*, 25(9):1463–1470, 2007.

[30] K. J. Laidler. The development of the arrhenius equation. *Journal of Chemical Education*, 61(6):494, 1984.

[31] I. Langmuir. The vapor pressure of metallic tungsten. *Physical Review*, 2(5):329, 1913.

[32] M. Larini, F. Giroud, B. Porterie, and J.-C. Loraud. A multiphase formulation for fire propagation in heterogeneous combustible media. *International Journal of Heat and Mass Transfer*, 41(6-7):881–897, 1998.

[33] Y. Llave, K. Takemori, M. Fukuoka, T. Takemori, H. Tomita, and N. Sakai. Mathematical modeling of shrinkage deformation in eggplant undergoing simultaneous heat and mass transfer during convection-oven roasting. *Journal of Food Engineering*, 178:124–136, 2016.

[34] S. I. F. S. Martins, W. M. F. Jongen, and M. A. J. S. Van Boekel. A review of maillard reaction in food and implications to kinetic modelling. *Trends in Food Science & Technology*, 11(9-10):364–373, 2000.

[35] MATLAB. Users' guide and statistics toolbox release, 1990.

[36] S. W. McCue, B. Wu, and J. M. Hill. Classical two-phase stefan problem for spheres. *Proceedings of the Royal Society of London A*, 464(2096):2055–2076, 2008.

[37] A. M. Meirmanov. *The Stefan Problem*, volume 3. Walter de Gruyter, 1992.

[38] H. Ni and A. K. Datta. Heat and moisture transfer in baking of potato slabs. *Drying Technology*, 17(10):2069–2092, 1999.

[39] H. Ni, A. K. Datta, and K. E. Torrance. Moisture transport in intensive microwave heating of biomaterials: a multiphase porous media model. *International Journal of Heat and Mass Transfer*, 42(8):1501–1512, 1999.

[40] C. R. Oswin. The kinetics of package life. iii. the isotherm. *Journal of Chemical Technology and Biotechnology*, 65(12):419–421, 1946.

[41] S. Paik and H. D. Nguyen. Numerical modeling of multiphase plasma/soil flow and heat transfer in an electric arc furnace. *International Journal of Heat and Mass Transfer*, 38(7):1161–1171, 1995.

[42] R. Pečenko, S. Svensson, and T. Hozjan. Modelling heat and moisture transfer in timber exposed to fire. *International Journal of Heat and Mass Transfer*, 87:598–605, 2015.

[43] C. Peishi and D. C. T. Pei. A mathematical model of drying processes. *International Journal of Heat and Mass Transfer*, 32(2):297–310, 1989.

[44] P. Perré and I. W. Turner. A 3-d version of transpore: a comprehensive heat and mass transfer computational model for simulating the drying of porous media. *International Journal of Heat and Mass Transfer*, 42(24):4501–4521, 1999.

[45] R. Perren, R. Geiger, S. Schenker, and F. Scher. Recent developments in coffee roasting technology. In *20th International Conference on Coffee Science*, pages 451–459. Association for science and information on coffee, 2004.

[46] C. P. Please, M. J. McGuinness, and D. L. S. McElwain. Approximations to the distributed activation energy model for the pyrolysis of coal. *Combustion and Flame*, 133(1):107–117, 2003.

[47] R. J. Poole. The deborah and weissenberg numbers. *British Society of Rheology, Rheology Bulletin*, 53:32–39, 2012.

[48] L. Roberts, E. Nordgård-Hansen, Ø. Mikkelsen, S. A. Halvorsen, and R. A. Van Gorder. A heat and mass transfer study of carbon paste baking. *International Communications in Heat and Mass Transfer*, 88:9–19, 2017.

[49] I. I. Ruiz-López, A. V. Córdova, G. C. Rodrıguez-Jimenes, and M. A. Garcıa-Alvarado. Moisture and temperature evolution during food drying: effect of variable properties. *Journal of Food Engineering*, 63(1):117–124, 2004.

[50] N. L. Salmen and G. L. Back. The influence of water on the glass transition temperature of cellulose. *Tappi*, 60(12):137–140, 1977.

[51] S. Schenker. *Investigations on the hot air roasting of coffee.* PhD thesis, Swiss Federal Institute of Technology, 2000.

[52] O. Séro-Guillaume and J. Margerit. Modelling forest fires. part i: a complete set of equations derived by extended irreversible thermodynamics. *International Journal of Heat and Mass Transfer*, 45(8):1705–1722, 2002.

[53] M. A. Stanish, G. S. Schajer, and F. Kayihan. A mathematical model of drying for hygroscopic porous media. *AIChE Journal*, 32(8):1301–1311, 1986.

[54] J. M. Talbot. *Grounds for agreement: The political economy of the coffee commodity chain.* Rowman & Littlefield Publishers, 2004.

[55] E. Tombari, G. Salvetti, C. Ferrari, and G. P. Johari. Kinetics and thermodynamics of sucrose hydrolysis from real-time enthalpy and heat capacity measurements. *The Journal of Physical Chemistry B*, 111(3):496–501, 2007.

[56] S. L. Truscott and I. W. Turner. A heterogeneous three-dimensional computational model for wood drying. *Applied Mathematical Modelling*, 29(4):381–410, 2005.

[57] R. Uzuoka and R. I. Borja. Dynamics of unsaturated poroelastic solids at finite strain. *International Journal for Numerical and Analytical Methods in Geomechanics*, 36(13):1535–1573, 2012.

[58] M. A. J. S. Van Boekel. Formation of flavour compounds in the maillard reaction. *Biotechnology Advances*, 24(2):230–233, 2006.

[59] C. Y. Wang and P. Cheng. A multiphase mixture model for multiphase, multicomponent transport in capillary porous media - i. model development. *International Journal of Heat and Mass Transfer*, 39(17):3607–3618, 1996.

[60] X. Wang and L. Lim. A kinetics and modeling study of coffee roasting under isothermal conditions. *Food and Bioprocess Technology*, 7(3):621–632, 2014.

[61] J. Zhang and A. K. Datta. Mathematical modeling of bread baking process. *Journal of Food Engineering*, 75(1):78–89, 2006.

[62] M. Z. Zhu, Y. F. Chen, W. B. Zhu, X. M. Du, J. B. Zhou, C. Gu, and R. J. Liao. Mechanical property of hydrous amorphous cellulose studied by molecular dynamics. *Russian Journal of Physical Chemistry B*, 10(3):524–530, 2016.